UNDERSTANDING FORMATION OF METALS AND ALLOYS IN SOLUTION WITH *IN SITU* CHARACTERIZATIONS

A Dissertation
Presented to
The Academic Faculty

by

Xuetian Ma

In Partial Fulfillment
of the Requirements for the Degree
Doctor of Philosophy in the
George W. Woodruff School of Mechanical Engineering

Georgia Institute of Technology
May 2019

UNDERSTANDING FORMATION OF METALS AND ALLOYS IN SOLUTION WITH *IN SITU* CHARACTERIZATIONS

Approved by:

Dr. Hailong Chen, Advisor
School of Mechanical Engineering
Georgia Institute of Technology

Dr. Peter Hesketh
School of Mechanical Engineering
Georgia Institute of Technology

Dr. Paul Kohl
School of Chemical & Biomolecular
Engineering
Georgia Institute of Technology

Dr. Shuman Xia
School of Mechanical Engineering
Georgia Institute of Technology

Dr. Ting Zhu
School of Mechanical Engineering
Georgia Institute of Technology

Date Approved: December 11, 2018

Dedicated to my parents.

ACKNOWLEDGEMENTS

There are so many great people who are essential to the completion of my five-year journey in graduate school. My sincere gratitude goes to them: my advisor, my committee members, my lab members, my collaborators, my funding agencies, administrative staffs in my department, and my family.

Firstly, I would like to thank my advisor, Dr. Hailong Chen. I came to Georgia Tech as the first student in Dr. Chen's group, when there was nothing but an empty space in Chen's group. We overcame many obstacles to build the laboratory from scratch together, which was one of my most unique experiences as a graduate student in Georgia Tech. It was Dr. Chen who not only led me into the research area of electrochemistry, but also taught me about responsibility, persistence, and motivation as an individual researcher. In addition, he was very supportive to my professional plan and is always willing to offer his insights to help me choose the right path for myself. I sincerely appreciate Dr. Chen for choosing me to be his first student and now, his first graduate in the group.

Next, I would like to thank my committee members, Dr. Peter Hesketh, Dr. Paul Kohl, Dr. Shuman Xia, and Dr. Ting Zhu for taking the time to serve on the committee and provide me very insightful suggestions, which are critical to the completion of this thesis.

I have a group of driven, and family-like lab members who make my graduate school life more enjoyable. I would like to thank Dr. Lufeng Yang, Shan Xiong, Zhantao Liu, Yifan Ma, Jacqueline Baidoo, Aijie Han, Yangyang Li, Jon Payne, Zoe Holderness, Jake Thiemann, Joy Zhang, Nabeel Chhatriwala, and Shikai Jin for their support and

iv

TABLE OF CONTENTS

LIST OF TABLES

LIST OF FIGURES

condition (d). The color bar indicates the calculated surface energy of each facet.

LIST OF SYMBOLS AND ABBREVIATIONS

hcp   hexagonal close-packed

fcc   face-centered cubic

DFT   Density Functional Theory

XRD   X-ray Diffraction

NSLS   National Synchrotron Light Source

APS   Advanced Photon Source

SEI   solid-electrolyte interphase

EG   ethylene glycol

AOT   dioctyl sulfosuccinate sodium salt

SUMMARY

Conventionally, phase diagrams serve as the road maps for the synthesis and processing of metals and alloys. However, the bulk phase diagrams oftentimes become not predictive in the synthesis of nanostructures of metals and alloys owing to the significant contribution of surface energy in the total energy. How the surface energy varies the total energy, and therefore alters the relative stability at nanometer scale, yet remain to be explored. Theoretical and systematic understanding on the formation of metal/alloy nanostructures and establishment of experiment-based nanometric phase diagrams are much desired.

To systematically understand and predict the stable polymorphic phases of metals and alloys, a combined computational and experimental approach was employed. Metallic Cobalt (Co) was chosen as a model system, where the two polymorphs, *fcc* and *hcp* phases, can be selectively formed in a solvothermal reaction with 100% selectivity, controlled by the addition of different capping agents that significantly vary and tune the surface energy of the two phases. It was found that despite the hexagonal close-packed (*hcp*) phase is the thermodynamically stable phase in bulk phase diagram, at nanometer scale, face-centered cubic (*fcc*) Co is a more favorable phase under neutral or acidic conditions (pH<8), while *hcp* Co is only more stable under basic condition (pH >8), due to the change of surface energy with the capping of OH^- with different concentrations. First-principles Density Functional Theory (DFT) computations were used to theoretically explain and understand this observation. The computational results not only agreed with the experiments extremely well, but also indicated this surface-dependent polymorphism can be generally applicable

in more material systems. A state-of-the-art *in situ* synchrotron X-ray Diffraction (XRD) platform was built at the synchrotron sources (Advanced Photon Source and National Synchrotron Light Source) to track the solvothermal reaction in real-time, which was rarely reported previously. The results confirmed that the phase selectivity is truly due to the surface induced relative thermodynamic stability change, instead of reaction kinetics.

Based on the above results, we further explored the polymorphs formation of Co through electrodeposition, for that electrodeposition offers more precisely tunable thermodynamic driving force than that in the solvothermal reactions. A novel synchrotron -based *in situ* electrodeposition platform was built to track the reaction process, where both pH of the electrolyte and over-potential can be easily tuned to control the nanoscale phase selection of Co upon nucleation. Aside from the pH effect, it was found that high over-potential expedites the kinetics of the reaction and yields both the metastable phase and stable phase concurrently in certain pH ranges.

Based on the aforementioned work on simple substance metal, we further explored the polymorphism and formation of binary alloys with using Cobalt (Co) -Nickel (Ni) as the model system, for that Co and Ni have similar reduction potential, atomic radius, and a binary phase diagram composing of *hcp* and/or *fcc* solid solution for entire composition. A series of electrodeposition experiments and ex situ and *in situ* characterizations were carried out to investigate the polymorph formation. It was found that the polymorphs formation of Co-Ni is determined by a number of key factors, including the composition (elementary ratio), the pH of electrolyte and the over-potential. These factors together impact the surface energy and the thermodynamics of the nanometric alloy particles, as well as the kinetics of reaction, and thus alternate phase boundaries in the phase diagram.

The formation and polymorph selection of alloys are far more complicated than simple metals in both solvothermal and electrodeposition conditions. This work revealed some fundamental insights of the binary alloys and opens the door towards a better understanding on the formation of more complicated alloys system through advanced *in situ* technique.

Inspired by the new findings in above fundamental research, we also conducted research closely related to applications. We explored the potential application of using electrodeposited metals for electrochemical energy storage. Recent progresses of using copper (Cu) or carbon as current collectors of lithium metal batteries inspired us to investigate using electrodeposited 3-D nano-structured Cu layer as the current collector with controlled morphology that can effectively suppress the formation Li dendrites. Herein, we developed a facile one-step electrodeposition process for low-cost, scalable fabrication of copper current collectors with 3-D architected nano-porous structures composed of interconnected nanoparticles of Cu. Li anode deposited onto this porous current collector exhibits good cycling stability of >340 hours in symmetric cells without short-circuit. When tested in full cells with either liquid or solid-state electrolyte, the Li anode hosted in the 3-D Cu current collector demonstrated excellent cycling performance with no dendrites formation. This electrodeposition processing is extremely simple and scalable and can be easily incorporated into current roll-to-roll manufacturing of Li-ion batteries, which may have immediate and significant impact on the battery industry.

The results presented in this dissertation revealed unprecedented fundamental insights on the surface-controlled formation and polymorph selectivity of metals and binary alloys in both chemical and electrochemical potential driven solution reactions and opens the door towards the establishment of predictive nanometric phase diagrams for other metal

and complex alloys. The development of the state-of-the-art *in situ* XRD systems for solvothermal and electrodeposition reactions enabled real-time observation of nucleation, crystal growth and ripening of metal/alloy nanoclusters in solution, which not only provided solid experimental evidence of this research, but also offered a powerful characterization method to research on other materials and could impact multiple fields in solid-state chemistry, electrochemistry, and materials engineering.

CHAPTER 1.   INTRODUCTION

1.1   Formation of materials in nanometer scale

Nanometric materials are generally defined as the materials that have at least one dimension of size within 1 and 100 nanometers (nm)[1] and usually contain several hundreds to 10^5 atoms.[2] Many important applications require that the materials must be synthesized in nanostructures instead of bulk to have desired properties. For example, $LiFePO_4$ as a popular cathode material for lithium ion batteries can only demonstrate ultrahigh ionic conductivity in nanoparticles form.[3] As shown in Figure 1, the ratio of unblocked conducting channel rapidly declines with increasing size of particles, resulting in deteriorating ionic conductivity when used as an electrode material. In addition, various applications of nanoparticles, including optical, magnetic devices, and catalysts, show size dependence,[4,5] as the relaxation of the crystal lattice with limited number of unit cells in the fine nanoparticles induces different bond length, bond angle, and periodicity of the crystal field than those in bulk crystals, therefore changes the electronic structures.
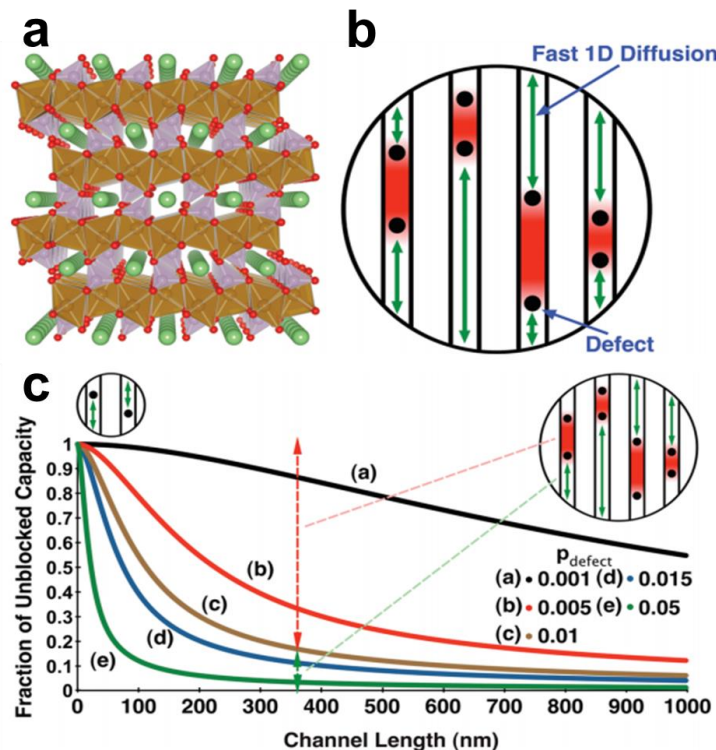
Figure 1 (a) Crystal structure of LiFePO₄ along [010] direction; (b) Schematic illustration of Li⁺ diffusion impeded by immobile point defects in 1D channel; (c) Expected unblocked capacity vs channel length in LiFePO₄. Adapted from [3].

At nanometric scale, many meta-stable phases and polymorphs may be favored over the thermodynamically stable phase in the phase diagram. Thus, the phase diagrams built upon bulk phase thermodynamics provide limited guidance for synthesizing materials at nanometer scale. This deviation from conventional phase diagrams is mainly due to the significant contribution of surface energy into the total energy of the nanometric crystal.[6–8] How the surface exactly varies the total energy and thus alters the phase diagram at nanometric scale is the fundamental question necessary for understanding and guiding the synthesis of nanomaterials.

Methods have been demonstrated in a wide range of nanomaterials to tune the physical features, such as the particle size,[9,10] morphology,[11–14] and exposing facets,[15,16] to obtain enhanced properties that are useful for certain applications. The final structure of the nanoparticles is determined by a combination of factors during both nucleation and growth stages,[17] including kinetic factors[18,19] and thermodynamic factors,[20,21] which are affected by the surface energy and the thermodynamic formation energy of the bulk materials. According to Gibbs-Curie-Wulff theorem,[22] the shape of a single crystal is a result of minimizing the surface energies of all facets.[23] The prevailing methods to tune the size and morphology of certain functional materials is to use capping agents to control the growth kinetics for the different exposing surfaces. For example, Xia et al.[24] reported that the surfactant, polyvinylpyrrolidone (PVP) has selective interaction with different facets of silver nanoparticles, resulting in a change of the growth rate ratio along <100> and <111> directions of the *fcc* silver nanoparticles. Alivisatos et al.[12] reported the formation of twinned CdSe tetrahedron as quantum dots with using hexyl-phosphonic acid (HPA, $C_6H_{15}PO_3$) added to pure trioctylphosphine oxide (TOPO) as surfactant to tune the growth kinetics. However, most of such pervious works focused on tuning and controlling the geometric features of a given material with the same phase/crystal structure.[25–27] It is rare to see the crystal structure or the space group of the material can be completely changed depending on the capping status or particle size.

Some previous investigations did demonstrate that possibility of such dependence.[6-8,28–30] Navrotsky et al.[31] (Figure 2a) demonstrated experimentally of the polymorphs of TiO_2, with using both adsorbed water molecule and particle size as tuning factors to control the formation of the nanoscale polymorphs (e.g., rutile and anatase). According to the

3

result, with increasing portion of surface area per mole (indicating reducing size of primary particle), the more stable phase changes from rutile, to brookite, and eventually, anatase, demonstrating apparent deviation from stable bulk phase diagram. Ceder et al.[7] (Figure 2b) reported a computational study on calcite mineral with using solution capping ion (Mg^{2+}) as the tuning factor to obtain metastable aragonite nanophase. The absorbed Mg^{2+} alters the stable Wulff shape and thereafter changes the surface energy of particles. As a result, the bulk metastable aragonite phase can be synthesized. And in recent research, K^+ [8] and Mg^{2+} [30] was used to tune the formation of different polymorphs of MnO_2 in solution, respectively. However, in the three later cases, the composition of the polymorphs was not exactly the same, due to incorporation of the doping cations. In a parallel effort, we aim to explore the interplay of bulk lattice energy and surface energy in a system with constant composition to reveal and quantitatively evaluate the polymorphism induced solely by surface energy contributions. It would be worthy trying to establish a thorough approach using a model system that can be generalized to other similar or more complicated systems. To address this question, a proper nanoparticle compound with relatively small ground-state-energy difference of various polymorphs is preferred.
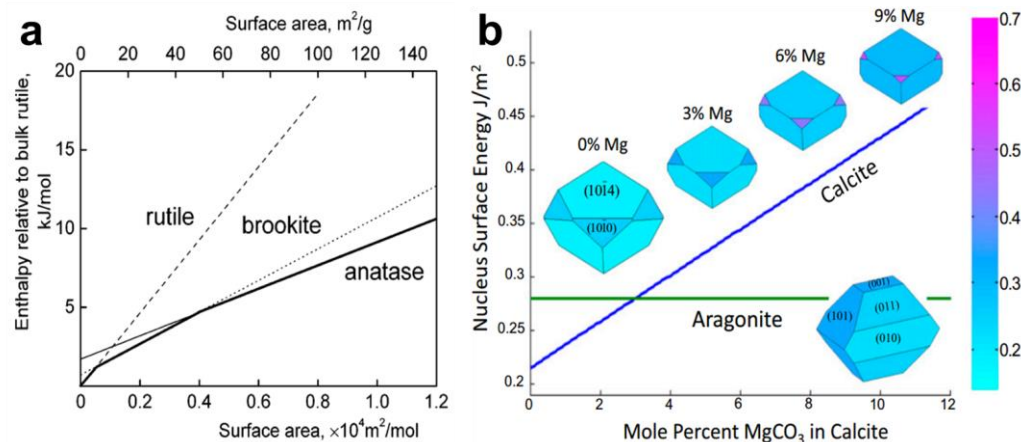
Figure 2 (a) Energetics of nano-titania. Solid line shows energetic stability regions of different phases, adapted from [31]; (b) Morphology-averaged surface energies for hydrated Mg-calcite and aragonite as a function of Mg^{2+} uptake in calcite, adapted from [7]. Colors correspond to facet-specific surface energies. Aragonite does not incorporate Mg^{2+}.

1.2 Selection of model material systems

For this reason, metallic cobalt was chosen as the model system to begin with. Cobalt is known to have two common polymorphs, the hexagonal close-packed (*hcp*) phase and the face-centered cubic (*fcc*) phase. In the bulk material, the *hcp* phase is thermodynamically more stable at lower temperatures while the *fcc* phase is more stable above 450 °C. [32] Nanometric Co is widely used as magnetic, electrical, and catalytic materials, warranting the importance of understanding it polymorphism in nanometer scales.[33] In previous efforts to synthesize Co nanoparticles, the results varied depending on different synthesis conditions. Some syntheses yield *fcc*,[34,35] some yield *hcp*,[36,37] and some yield the mixture of the two.[38] There is a lack of systematic and fundamental understanding why these phases selectively form and how to control the selectivity. Based on these considerations, we for the first time identified a method that could tune the formation of *fcc* and *hcp* Co with 100% selectivity and conducted DFT computations to identify the

5

energy contribution from the surfaces and its critical role in determining the formation of different polymorphs.

Furthermore, based on the results obtained from Co, we extend the investigation to Co-based bimetallic nanoparticles with interesting magnetic, mechanical, or electrochemical properties. The principals of selecting an appropriate system is that the two elements should have similar 1) electrode potential, 2) atomic radius, and have less complicated phase complexity. Nickel (Ni) is one of the elements that meet with the aforementioned criteria, for that: 1) its standard electrode potential[39] is -0.25 V (Co: -0.28V); 2) its empirically measured covalent radius[40] is 135 pm (Co: ~135 pm); and 3) it forms *hcp* phase with Co below 25% a.t. Ni, and *fcc* phase with Co above 35% a.t. Ni[41] (as shown in Figure 3). Solid solution Co-Ni is formed over the whole atomic ratio range. Co-Ni alloy nanoparticles are known to be efficient catalysts for hydrazine fuel cells,[42] alkaline water electrolysis,[43] and perpendicular magnetic recording.[44] Therefore, we have selected Co-Ni as the alloy system to start with. With introducing another key factor, composition (elementary ratio), how the nanometric polymorphs would be tuned with contribution from surface energy remains unknown and challenging. We believe that using Co-Ni bimetallic system would be a good example to explore multiple elements and future extend to the better understanding on phase formation of high-entropy-alloy (HEA).
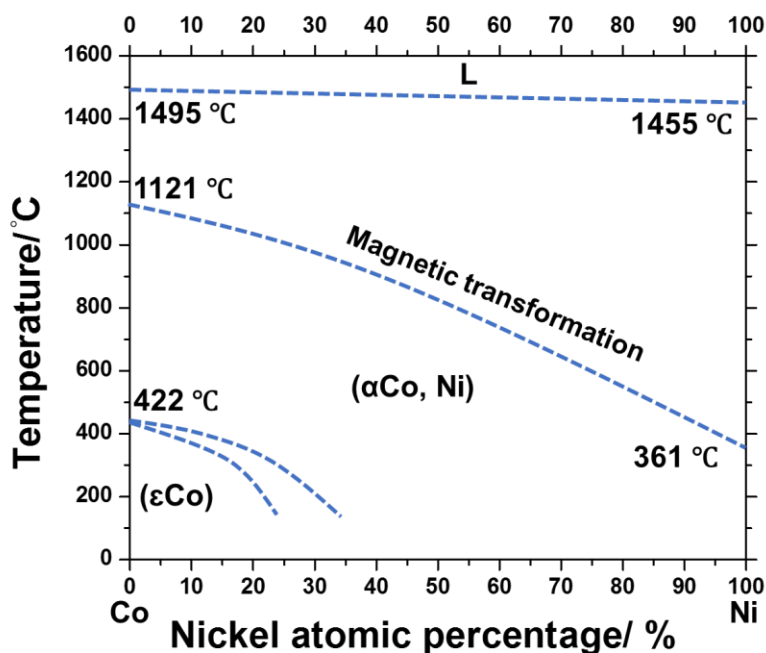
Figure 3 Cobalt – Nickel bulk phase diagram. Reproduced from [41].

1.3   Solvothermal and electrodeposition methods

There are two methods that we applied in this dissertation, a polyol-based solvothermal method and an electrodeposition method.

Solvothermal method is a commonly used approach to produce chemical in laboratory through reaction in a stainless steel autoclave. The schematic set up is shown in Figure 4a.[45] The difference of solvothermal reaction with hydrothermal is that the former one uses organic solvent as reactant while the latter one uses water. Using solvothermal route gains one the benefits of both the sol-gel[46] and hydrothermal routes[47] - allowing for the precise control over the size, shape distribution, and crystallinity of nanoparticles under a milder conditions. The advantages[48] of polyol-based wet-chemistry synthesis are: 1)

7

environmentally benign; 2) it avoids other problems encountered by high-temperature processes such as poor stoichiometric control due to volatilization of components or stress-induced defects; 3) it offers more factors to tune the surface energy by applying different possible capping ions/functional groups, compared to all solid-state reactions or physical metallurgy. Therefore, solvothermal synthesis has been widely used in laboratory to make nanostructured metals[49], titanium dioxide,[50] graphene,[51] carbon,[52] and other functional materials.

Electrodeposition, on the other hand, is a more facile, economic, and easy-to-upscale or downscale room-temperature approach for practical application.[53] The schematic set up is shown in Figure 4b.[54] Typical electrodeposition could be three-electrode based or two electrode-based. In Figure 4b, a 3-electrode system is demonstrated, with working electrode (WE), counter electrode (CE), and reference electrode (RE) immersed in electrolytic solution which contains the deposited metal ions. During the process, an electric current is applied to reduce the dissolved metal ions cations at the interface between the solution and working electrode substrate and forms a layer of metal coating. Meanwhile, the oxidation reaction will take place at CE. The reference electrode, including commonly used saturated calomel electrode (SCE) or Ag/AgCl electrode, is one that has a stable and well-known electrode potential.[55] The high stability of the reference electrode potential is usually reached by employing a redox system with constant (buffered or saturated) concentrations of each participant of the redox reaction. [56] It is used to accurately measure the potential of working electrode during reaction.

Electrodeposition is an approach that the thickness and morphology of the nanostructures can be precisely controlled by adjusting the electrochemical parameters.

Among them, overpotential is an important one that would impact the reaction kinetics. It is defined as the potential difference (voltage) between a half-reaction's thermodynamically determined reduction potential and the potential at which the redox reaction is experimentally observed.[56] The quantity of overpotential is specific to the design of cell and varies across operation condition and cells, even for the same reaction. It is experimentally determined by measuring the potential at which a given current density is achieved. By increasing over-potential, the reaction kinetics would be tuned, which would impact morphology of the as-synthesized materials. The controllable factors of electrodeposition, e.g., over-potential, time, additives, and substrate, could make it possible to realize step synthesis and achieve multi-layer structures. It is also the approach that can accommodate elements with various reducing potential by adjusting the applied potential. Therefore, in the following section, the results on Co model system using both solvothermal method and electrodeposition method will be discussed. Regarding Co-Ni system, due to the fact that polyol-based reaction has a fixed reducing potential, determined by reducing agent, thus limits its capability to tune the polymorphs, thereafter, electrodeposition approach will be used.
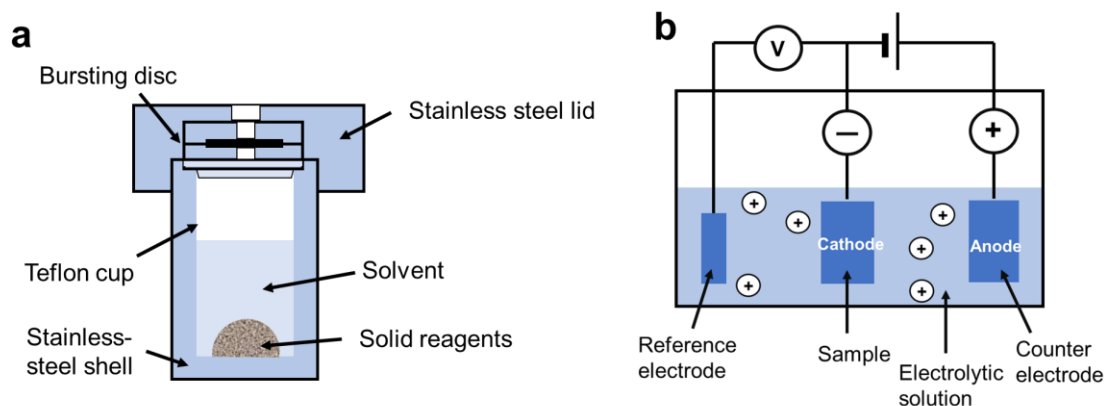
Figure 4 Schematic set up of (a) Teflon-lined, stainless autoclave used for solvothermal reaction (reproduced from [45]); (b) three-electrode electrodeposition bath (reproduced from [54]).

1.4 *In situ* synchrotron X-ray diffraction

A key question remaining unclear is that, by far, most of the works focus on discussing structure upon completion of the reaction. However, it is possible that the polymorphs convert during the reaction leading to different initial and final phases. As some reactions, e.g., solvothermal or molten salt, take a long time to be cooled down, it is impossible to prove or rule out such transformations with postmortem or ex situ investigations, therefore calling for the need for *in situ* observation and characterization. *In situ* synchrotron X-ray Diffraction (XRD) offers such possibility. Synchrotron XRD is an extremely powerful source of X-rays. The X-rays are produced by high energy electrons as they circulate around the synchrotron. It builds on the physical phenomenon that a moving electron emits energy when it changes direction. If the electron is moving fast enough, the emitted energy, called synchrotron radiation, is at X-ray wavelength.[57]

In particular, *in situ* synchrotron X-ray Diffraction (XRD) offers unique advantage because of its high flux (6 x 10^{13} photons/sec at NSLS II 28-ID-2 and 6 x 10^{10} photons/sec

@27 keV at APS 17BM-B) and fast 2D detectors (as low as 1 second per exposure) to observe materials as a function of process parameters such as temperature, pH, pressure, etc. with atomic precision. As shown in Figure 5, the high-energy e-beam is generated from e-gun and enters booster ring to accelerate the energy. Typically, booster rings work a few times per day, when the storage ring is refilled. The storage ring is a tube where the electrons circle for hours close to the speed of light. By passing through different magnets when traveling around the ring, the electrons produce x-rays. Afterwards, they enter the individual beam line hutch for specific applications. A series of auxiliary components including bending magnets, slits, mirrors, and monochromator in the hutch are used to select the beam with specific wavelength and beam shape for end use.[58]
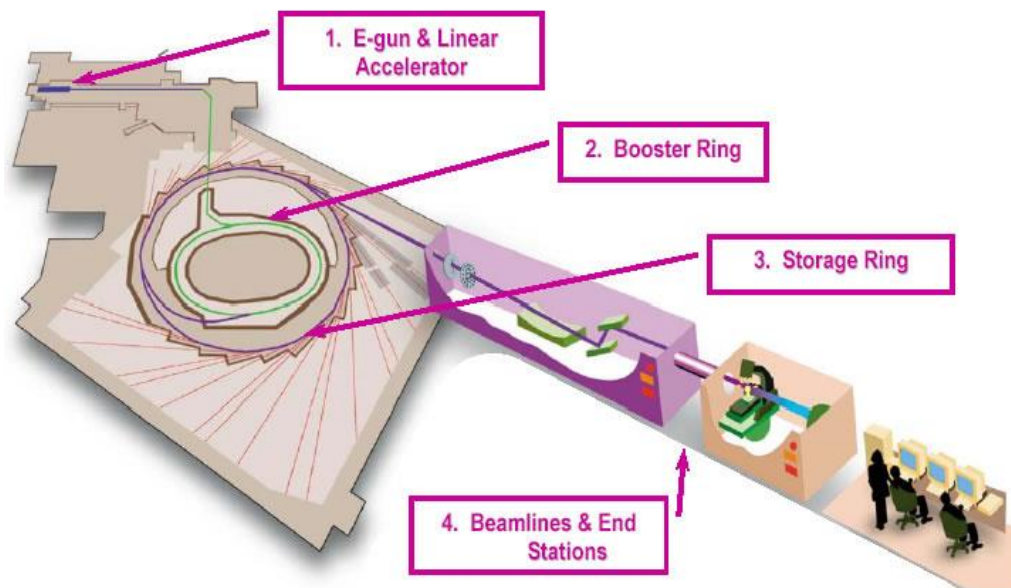
Figure 5 Illustration of how synchrotron works. Adapted from work supported by the National Science Foundation under Grant No. 0237162. Courtesy: Canadian Light Source.

Regarding operation for the aforementioned two synthesis approaches, the main hurdles are :1) For solvothermal reaction, the high pressure generated by the solution at elevated temperatures (r.t. to a few hundreds of Celsius) conventionally requires using thick-walled press vessels made of high strength metals, which makes it impossible to detect the reaction inside in real time with any characterization tools; 2) For electrodeposition, the reaction takes place within seconds upon nucleation yet the weak signal is very hard to be detected by ex situ techniques. To address these issues and take advantage of the capability of *in situ* synchrotron XRD, we have successfully developed two unique platforms on beam lines at NSLS (I and II) and APS, making it possible to track the whole process throughout nucleation to phase growth either in high-pressure solvothermal system or fast-reaction electrodeposition system. The setups will be discussed in the following chapters. The endeavor also paves the way for future study on more complicated systems (alloys, oxides etc.) regarding phase formation in solutions under nanoscale.

CHAPTER 2.   GUIDING SYNTHESIS OF POLYMORPHS OF MATERIALS USING NANOMETRIC PHASE DIAGRAMS

2.1   Introduction

Conventionally, phase diagrams serve as road maps for the design and synthesis of materials. However, bulk phase diagrams are often not as predictive for the synthesis of nanometric materials, mainly due to the increased significance of surface energy. The change of surface energy can drastically alter the total energy of the nanocrystals thus yield a polymorph or meta-stable phase different than the stable phase in bulk, providing a means for controlling the synthesis of metastable phases. To achieve a theoretical and systematical understanding on the polymorphism of nanomaterials, metallic cobalt was chosen as a model system, where the two polymorphs, *fcc* and *hcp* phases, can be tuned with 100% selectivity in a solvothermal reaction. Advanced *in situ* synchrotron X-ray diffraction (XRD) technique and density functionals theory (DFT) were complementary employed to reveal the size and surface dependent polymorphism at nanometer scale. The nanometric phase diagram provides a general predictive approach to guide the synthesis of metastable materials.

2.2   Methods

2.2.1   Solvothermal synthesis.

As a typical protocol for the synthesis of Co nanoparticles, 3mmol cobalt hydroxide ($Co(OH)_2$) (99.9%, Alfa Aesar) and a certain amount of potassium hydroxide (KOH) (85%, Alfa Aesar), varying from 0 g, 1 g, 2 g to 4 g, were dissolved in 12 g ethylene glycol (EG)

(99+%, Alfa Aesar) at room temperature to form solutions with various pH values. Then the slurry was transferred into polytretrafluoroethylene(PTFE) lined 23ml stainless steel hydrothermal autoclaves (Parr Instrument). The autoclaves were put into an oven at the desired temperature and for desired reaction time. After the completion of the reaction, the autoclaves were cooled down to room temperature. The solid products were separated from the solution by centrifugation at 4000 rpm (Centrifuge, Eppendorf 5804R), washed three times with distilled water and one time with acetone, and finally dried in an oven in air at 60 ℃ for 2-3 hours.

2.2.2 Computational methods.

The ground-state bulk and surface energies of *fcc* and *hcp* Co were calculated using DFT with the projector augmented-wave approach (PAW)[59] as implemented in the Vienna *ab initio* simulation package (VASP).[60] The generalized gradient approximation (GGA) of Perdew, Burke, and Ernzerhof (PBE) was used for the exchange-correlation energy.[61] The plane-wave energy cutoff and k-point mesh were consistent with parameters used by the Materials Project (MP).[62] Surface calculations were performed using supercells of Co metal slabs with vacuum regions on both sides of the slab. H^+, OH^-, and H_2O adsorbates were added in several locations and concentrations while maintaining the symmetry of the slab surfaces. Surface energies, as dependent on adsorbates and pH, were calculated using the following expression:

$$\gamma = \frac{1}{2A}(E_{slab} - n_{Co}E_{bulk} - n_{ads}\mu_{ads})$$

14

where A is the area of the surface in the slab supercell model, E_{slab} is the total energy of the slab-vacuum supercell, E_{bulk} is the energy of the bulk phase, and μ_{ads} depends on the adsorbate type. For example, for OH⁻ adsorbates, $\mu_{OH} = \Delta G^f_{H_2O} + \mu^0_H + \mu^0_O + kT ln(10)pH$.[63] Using the lowest energy configurations for each surface index, the Wulff shapes of Co nanoparticles in different pH conditions were constructed. The Wulff shapes were used to determine the bulk and surface energy of a nanoparticle as dependent on particle size. The total energy was found as a sum of the bulk and surface energy terms. The total energy difference between nanoparticles of each polymorph was calculated to generate the *fcc-hcp* phase diagram as a function of particle size and pH. The total energies neglected the contribution of the *PV* term and the entropy term, which are expected to largely cancel out in calculating the energy differences between the two solid phases.[64]

2.2.3   *In situ synchrotron X-ray diffraction for the solvothermal synthesis.*

The *in situ* synchrotron XRD experiments on cobalt nanoparticles were done at beam line X14A (wavelength=0.7793 Å), the National Synchrotron Light Source (NSLS) at Brookhaven National Laboratory and at beam line 17-BM-B (wavelength=0.7277 Å), Advanced Photon Source (APS) at Argonne National Laboratory with slightly different setups. $Co(OH)_2$, KOH, and EG were mixed to form a pinkish slurry with various pH values with a procedure similar as described above. An *in situ* solvothermal cell was used to collect XRD pattern during the solvothermal reaction, as schematically illustrated in Figure 6. The solution/slurry in the quartz tube with 1 mm inner diameter was heated up to desired temperature with an air blower heater at NSLS and with a ceramic heating cell at APS, respectively.
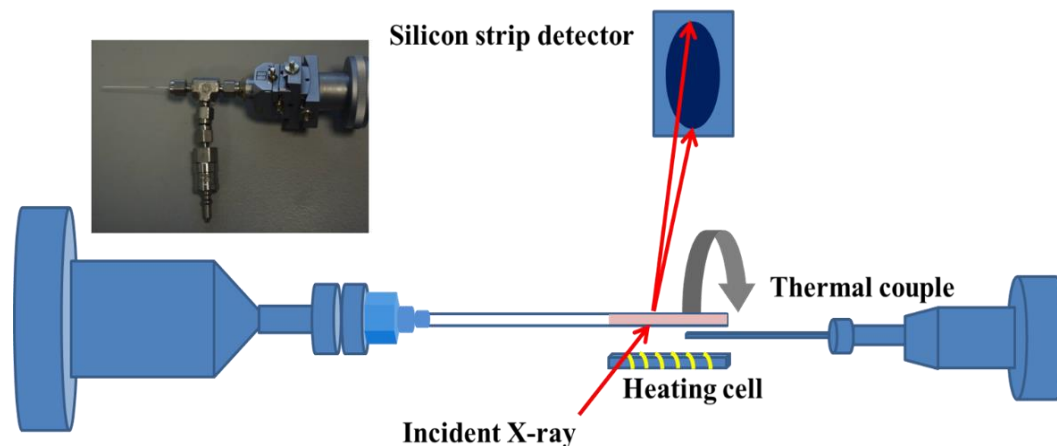
Figure 6 *In situ* **solvothermal cell set-up at X14A at NSLS.**

The temperature of heating cell was calibrated with using a thermal couple placed at the tip of the capillary and with using a thermal couple inserted into an empty quartz tube. The calibrations from the two methods have negligible deviations. The quartz tube was spun during heating for the purposes of stirring the solution and averaging the orientations of the powder. XRD patterns were collected with a step size of 10 or 20 ℃ till the desired temperature was reached. Each XRD scan typically took 5-15 minutes, depending on the concentration of the solution. At each step, two-minute idling time was used to allow the reaction and temperature to stabilize and then the temperature was held during the XRD scan. When the desired reaction temperature was reached, such as 200 or 250 ℃, the temperature was held for a few hours to allow the reaction fully complete. During this period, XRD scans were taken every 5-30 minutes, depending on the kinetics of each batch of reaction. Finally, the tube was cooled down to room temperature after the scans were done.

2.2.4   Other Characterizations.

An X-ray Diffractometer (D8 Advanced, Bruker) with a Molybdenum radiation ($\lambda_{K\alpha1}$=0.709Å) was used to examine the crystalline phase of the synthesized compound from 2θ between 8° to 40°. Rietveld refinement was done to determine the ratio of the polymorphs in the mixture as well as to obtain the lattice parameters with using GSAS software.[65] High resolution transmission electron microscopy (HRTEM) and scanning transmission electron microscopy (STEM) were performed to reveal the morphology and crystal structure of as-synthesized Co nanoparticles under various conditions using the double aberration-corrected JEOL-ARM200CF microscope with a cold-field emission gun and operated at 200 kV.

2.3   Results and Discussion

2.3.1   Selective formation of hcp and fcc Co.

Based on the hypothesis that the surface energy may significantly vary the total energy of nanometric crystals, it would be easiest to observe this effect at the nucleation stage as then the surface atoms take the largest fraction of the total number of atoms. To control the formation of different polymorphs via tuning of surface energy, a natural thought is to use different absorbents/capping agents. Experimentally, we choose to use a polyol-based solvothermal reduction method to synthesize Co nanoparticles as wet-chemistry synthesis allows more possible capping ions/functional groups, compared to synthesis with all solid-state reactions or physical metallurgy.[66] In the solvothermal synthesis of Co, it turns out that even a very simple capping agent, OH⁻, could vary the surface energy enough to change the relative stability of the two polymorphs. In our

solvothermal synthesis, $Co(OH)_2$ was used as the cobalt source, while ethylene glycol (EG) was used as both the solvent and the reducing agent, and 0 to 4 g of KOH was used as the additive. $Co(OH)_2$ is slightly soluble in basic EG solution. The reduction reaction takes place typically at temperature >180 ℃ as follows:

$$Co(OH)_2 \rightarrow Co^{2+} + 2OH^- \tag{1}$$

$$Co^{2+} + CH_2OH\text{-}CH_2OH \rightarrow Co + CH_3COOH + 2H^+ \tag{2}$$

With this solution reaction, the newly formed Co^0 nucleates in very small clusters. Because this reaction requires basic or neutral solution to go forward, as implied in reaction (2), and because metallic Co reacts with acids, therefore, acidic solution was not tested. Table 1 summarizes the synthesis conditions of different samples. Samples obtained from batches with different amount of KOH (4 g, 2 g, 1 g, and 0 g) are denoted as S1, S2, S3 and S4, respectively. Figure 7 shows the XRD patterns of each sample. For S1, with 4 g KOH added to obtain a high concentration of OH⁻, which almost reaches the solubility limit of KOH in EG solvent, the product is pure *hcp* Co (PDF#05-0727). This result is in accordance with the bulk phase diagram in that *hcp* Co is the stable phase below 450 °C. However, for S4, where no KOH is added and the solution is neutral, the reaction yields pure *fcc* Co phase (PDF#15-0806). This result clearly deviates from the bulk phase diagram, as the temperature that converts bulk *hcp* Co to *fcc* Co is 450 ℃ while our reaction temperature is only 200 ℃. With intermediate amount of KOH (1 g) adding in the solution, the product is a mixture of approximately equal amount of *hcp* and *fcc* phases. With increasing amount of KOH to 2 g, sample S2 yields more *hcp* phase than *fcc* phase. The relative ratio of the two phases in S2 and S3 phases are extracted by using two-phase whole-pattern fitting on the XRD patterns of these samples. The refinement results and parameters

18

of all four samples are shown in Table 2 and Figure 8. In S2 and S3, the fraction of *hcp*

Co is determined to be 79% and 64%, respectively. This gradual change in the composition

of product from pure *hcp* to the mixture and then to pure *fcc* shows obvious dependence on

the concentration of OH⁻ in the solvothermal solution.

Table 1 Synthesis conditions of Co(OH)₂ in EG with different KOH amounts.

Sample number	Co(OH)₂/mmol	EG/g	KOH/g	Temperature/℃	Reaction time/h
S1	3	12	4	200	20
S2	3	12	2	200	20
S3	3	12	1	200	20
S4	3	12	0	200	20
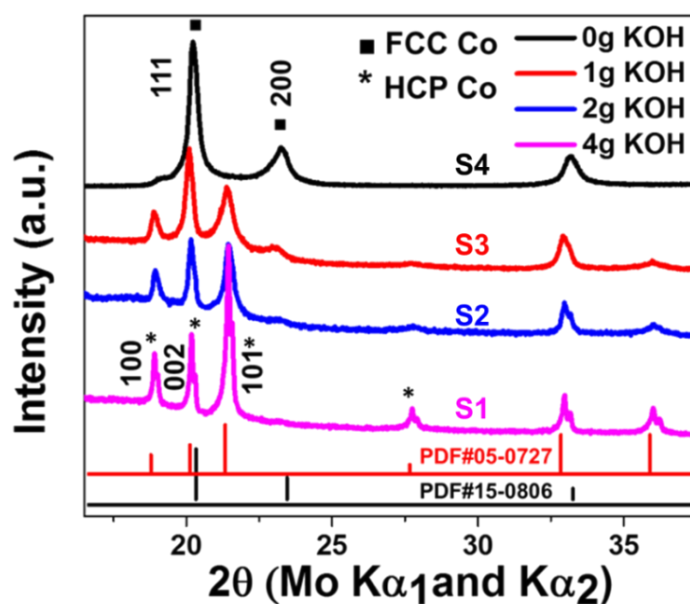
Figure 7 XRD patterns of S1, S2, S3 and S4, synthesized in solvothermal solutions with addition of 4 g, 2 g, 1 g, and 0 g KOH in 12g EG solvent, respectively.

Table 2 Refinements parameters of S1-S4.

Sample number	CHI2	wRp	Rp	hcp %	hcp cell parameters/ Å	fcc cell parameters/ Å
S1	5.049	0.0396	0.0265	100	a=b=2.51(3) c=4.08(5)	N/A
S2	5.170	0.0471	0.0329	78.5	a=b=2.52(5) c=4.10(9)	a=b=c=3.56(0)
S3	5.401	0.0580	0.0418	64.1	a=b=2.53(1) c=4.12(9)	a=b=c=3.57(0)
S4	5.781	0.0944	0.0788	0	N/A	a=b=c=3.56(0)
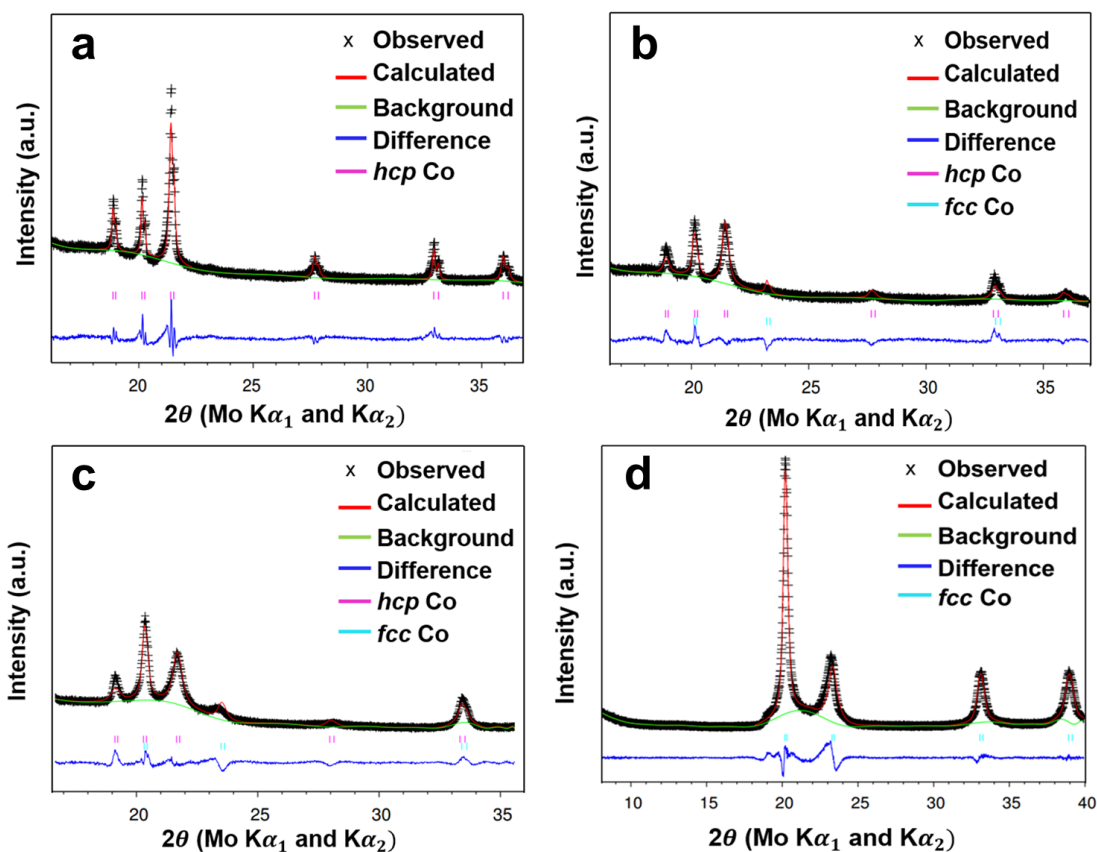
Figure 8 Refinements results of S1 (a), S2 (b), S3 (c), and S4 (d).

As solvothermal reactions using a statics Parr Instrument vessel without stirring take hours to reach the desired temperature and the reaction is slow and inhomogeneous, it is very difficult to collect samples at the nucleation stage. We collected samples with the shortest reaction time that yields a pure phase for microscopic investigations. Figure 9 shows the TEM images of Co nanoparticles that yield pure *fcc* (a,b,c) and pure *hcp* (d,e,f) phases, collected from a 9-hour and a 5-hour reaction, respectively. The particles show severe agglomeration but it could be seen that the primary particles are small single crystals with rather uniform sizes. No fused secondary particles were observed. The average size of *fcc* Co is around 2-4 nm, while for *hcp* Co it is about 3-5 nm. From the high-resolution images in Figure 9c and 9f, it could be seen that the particles are well-crystallized. The *d*-spacing of (111) faces in *fcc* Co is about 0.203 nm, while the *d*-spacing between (002) faces in *hcp* Co is about 0.206 nm, which agree with the values extracted from Rietveld refinement of the XRD patterns. The morphology and the exposing facets of the particles, however, is difficult to clearly identify due to the strong agglomeration of the particles, which is very common for nanoparticles.
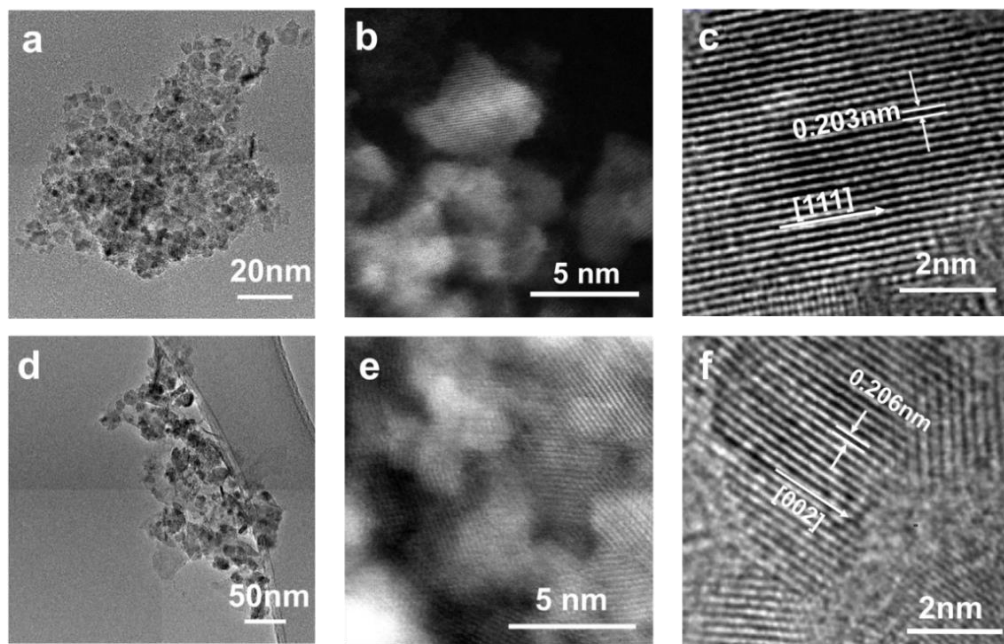
Figure 9 TEM (a,c) and STEM high angle annular dark field (HAADF) (b) images of pure *fcc* Co nanoparticles, with scale bars of 20 nm, 2nm, and 5 nm, respectively; TEM (d,f) and STEM-HAADF (e) images of pure *hcp* Co nanoparticles, with scale bars of 50 nm, 2nm, and 5 nm, respectively.

2.3.2   Surface energy of Co nanoparticles.

To understand how surface energy governs the formation of polymorphs of Co nanoparticles, DFT calculations were performed to evaluate the surface structures and surface energy of several low-index facets of *fcc* and *hcp* Co phases with various surface adsorbents. According to the Gibbs-Curie-Wulff theorem,[67] the shape of a single crystal is a result of minimizing the facets with lowest surface energies.[68] Calculations were performed for the (100), (110), and (111) surfaces of the *fcc* phase, and the ($1\bar{1}00$), (0001), ($2\bar{1}\bar{1}0$) surfaces of the *hcp* phase. The surface energies of surfaces with different adsorbents such as H^+, OH^-, and H_2O, with varying surface coverage were evaluated. The OH^- terminated surfaces were found to have the lowest surface energies for all *fcc* and *hcp* surfaces over a wide range of pH values (see Figure 10). It should be noted that the acidic

22

pH is only used in computation for the sake of covering a wide range of OH- concentration, while in experiments acidic pH cannot be tested because Co reacts with acid to form hydrogen gas.
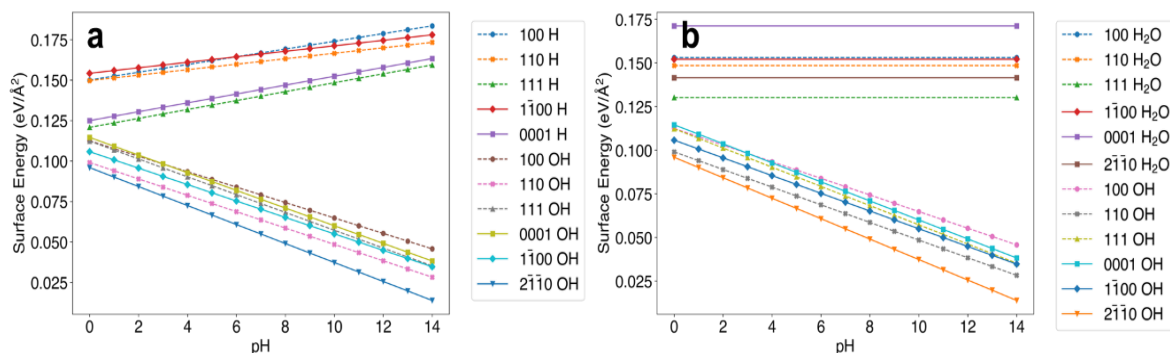
Figure 10 Comparison of surface energy of various facets of *fcc* and *hcp* Co with adsorbents OH⁻ and H⁺ (a); and OH⁻ and H₂O (b) over pH range of 0 to 14.

The calculated surface energies from the lowest-energy surfaces were used to construct Wulff shapes of *fcc* and *hcp* Co phases, which show the equilibrium morphology of a particle. Since the calculated surface energy varies with pH (i.e. the concentration of OH⁻), the Wulff shapes also changed as pH was increased (Figure 11). For all pH levels, the dominant facet in *fcc* Co was (110). The energy of the (110) surfaces decreased more rapidly than the (111) and (100) facets as the solution became more alkaline. As a result, with increasing pH, the fraction of the (110) facets in the Wulff shape increased, as shown in Figure 11a and 11b. The Wulff shape of *hcp* Co is a hexagonal prism, made of the $(2\bar{1}\bar{1}0)$ and (0001) facets in all pH conditions (Figure 11c and 11d). In summary, the surface energies and Wulff shapes of both *fcc* and *hcp* Co vary with pH values. This variation impacts the total energies of the Co nanoparticles and their preferences for *fcc* versus *hcp* phases as a function of pH (the concentration of OH⁻ in solution).

23
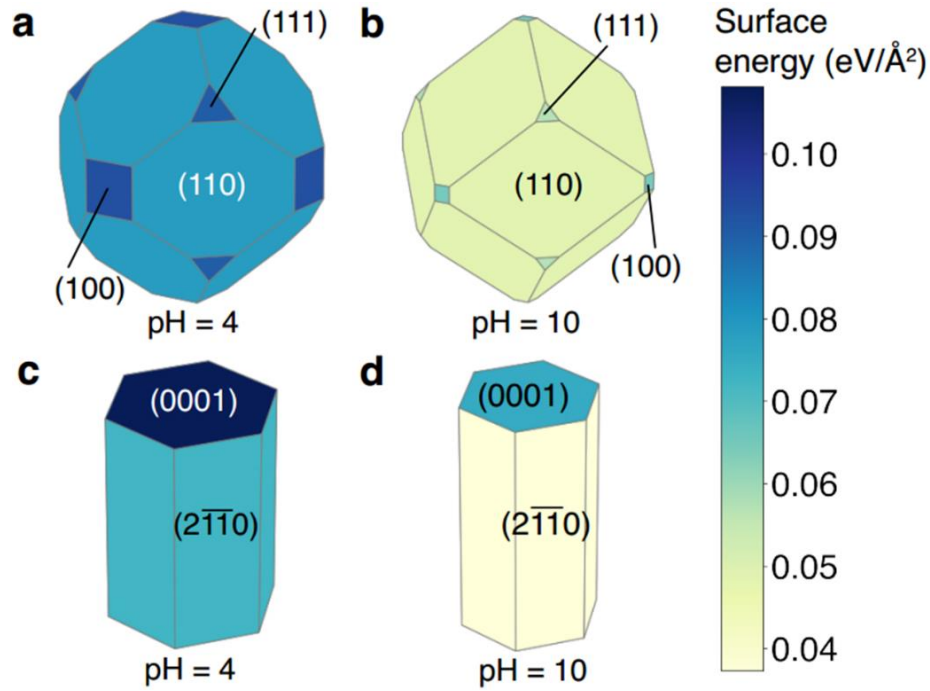
Figure 11 Wulff shapes of *fcc* Co in acidic condition (a) and basic condition (b); Wulff shapes of *hcp* Co in acidic condition (c) and basic condition (d). The color bar indicates the calculated surface energy of each facet.

2.3.3   Phase selectivity of Co nanoparticles.

To understand how the thermodynamically favored phase is influenced by the surface energy, the total energy of *hcp* and *fcc* Co nanoparticles was calculated and compared to construct a phase diagram as a function of particle size and pH values. The total energy of Co nanoparticles (in both *hcp* and *fcc* phases) as a function of particle size was calculated as the sum of the bulk energy and the total surface energy contributed from each facet present (see details in Methods). The phase diagram with respect to particle size and solution pH was constructed by comparing the total energies of Co nanoparticles in *hcp* and *fcc* phases (Figure 12). In short, the pH value determines the morphology of the nuclei and thus also determines the stable polymorph phase in this condition. The total energy difference between the two nanoparticle polymorphs describes the thermodynamic

driving force for the formation of a given phase. The larger the energy difference, the more one phase is favored over the other. As the phase diagram indicates, the *fcc* phase of Co is favored to nucleate in acidic pH conditions and for smaller particle sizes, and the *hcp* phase is favored under more basic conditions and favored as the Co particle becomes larger. These calculations could therefore explain the observed formation of *hcp* Co under high pH and formation of *fcc* Co under neutral pH at nanometer scale as the result of surface energy contribution. The formation of a mixture of *hcp* and *fcc* Co in samples S2 and S3 can be explained because at these intermediate pH values, the total energies of *hcp* and *fcc* nanoparticles are very similar. Therefore, the thermal fluctuations allow for the nucleation of both phases, but with statistical probabilities that are determined by the differences in their total energy (i.e. more *hcp* phase yields in S2 than in S3 due to the higher pH).
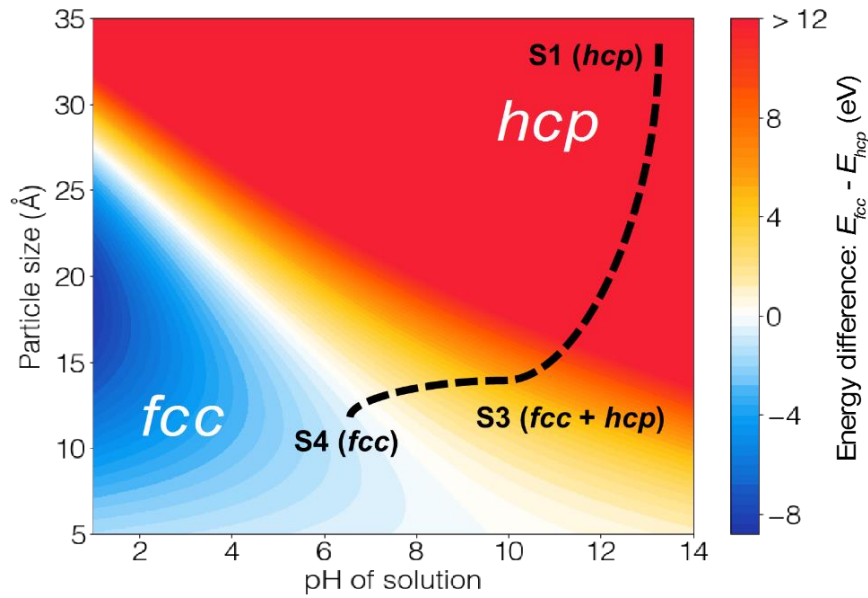
Figure 12 Phase diagram of *fcc* versus *hcp* Co nanoparticles with respect to varying particle size and pH level of the solution. The color bar shows the energy differences between the nanoparticles of the two phases. The black dashed line demonstrates

the trend of nanoscale polymorph formation under increasing pH environment, as observed in this work.

2.3.4   In situ XRD investigation.

By far, we have demonstrated that the *ex situ* experiments and computations agree with each other well on the observations that high concentration of OH⁻ coverage on the surface of the nuclei lowers the energy of the *hcp* phase as the stable polymorph. However, one could argue that what computation captures is the energy of the nuclei or the nanoclusters with size of a few nanometers, while the XRD patterns, as well as the TEM images, were taken from samples with a few tens of nanometers or micrometer sized sample. It is possible that the polymorphs may convert during the reaction therefore the initial and final phases are different. As it is rather slow to heat up and cool down the solvothermal reactor, it is impossible to rule out such transformations with postmortem or *ex situ* observations. Therefore, *in situ* observation and characterization is essentially necessary.   One outstanding challenge is that solvothermal synthesis, and similar hydrothermal synthesis, is previously considered as a black box. Because of the high pressure generated by the solution at elevated temperatures (r.t. to a few hundreds of Celsius), conventionally the solvothermal/hydrothermal reactions have to be carried out in thick-walled press vessels made of high strength metals, which made it impossible to detect the reaction inside in real time with any characterization tools. One can only guess the reactions inside by varying the starting materials and analyzing the products. In this study, we developed a unique platform that allowed us to *in situ* track the solvothermal reaction with high transmitting synchrotron X-ray, as elaborated in Methods. We were able to track

the full path of this solvothermal reaction in real time from starting materials to the nucleation state and the following crystal growth and ripening processes.

Solutions with same starting materials as used in the lab synthesis were used in the *in situ* XRD observations in the sealed quartz tube, namely S4, S3 and S1, as previous denoted. (See Table S3). Figure 13a, 13b, and 13c show the results of *in situ* solvothermal reactions done at beam line X14A at the National Synchrotron Light Source (NSLS) and at 17-BM-B at the Advanced Photon Source (APS). The reaction starts from room temperature, with a heating step of 10 ℃. As denoted in Figure 5, each reaction starts with $Co(OH)_2$, and gradually shows the nucleation and growth of Co phases while consuming the starting materials. As expected, S4 yields pure *fcc* Co phase, S3 yields a mixture of *hcp* and *fcc* phases, and S1 yields pure *hcp* Co phase. No phase cross-over was observed in any of these experiments, which confirms that the formation of the polymorphs starts directly from nucleation stage. Using Scherrer equation:[69]

$$\tau = \frac{b\lambda}{\beta cos\theta}$$

where:

τ is the average size of the crystallites as if they were cubes, monodisperse in size.

b is a shape factor, typically ranging from 0.89 to 0.94 depending on the function used to fit the peak.

β is the line broadening at half the maximum intensity (FWHM), after subtracting the instrumental line broadening, in radians.

θ is the Braggs angle in radians.

The particle size of *fcc* phase in S4 and *hcp phase in* S1 and S3 at the nucleation stage is estimated to be around 2 nm, 4 nm, and 3 nm, respectively. The particle size and phase composition of the samples are schematically labeled with the dashed line in Figure 12. Again, it shows that the computation and experiments well agree each other. It should be noted that in experiments, the *hcp* phase always shows larger particle size in the *in situ* XRD observation, either in the pure *hcp* product or in *hcp-fcc* mixed products. It is mainly because the thermodynamic driving force for the formation of *hcp* phase in high pH environments is greater than that of *fcc* phase in neutron pH, as indicated by the color in Figure 12. With the greater driving force, the particles of *hcp* phase grow faster and result in larger size than the *fcc* phase, under the same heating program in the *in situ* XRD experiments.

Table 3 Synthesis conditions of *in situ* synthesis of Co(OH)₂ in EG with different KOH amounts.

Sample number	*Co(OH)₂/mmol*	*EG/g*	*KOH/g*	*Temperature/℃*	*Temperature Step/℃*
S1	3	12	4	200	10
S3	3	12	1	200	10
S4	3	12	0	200	10
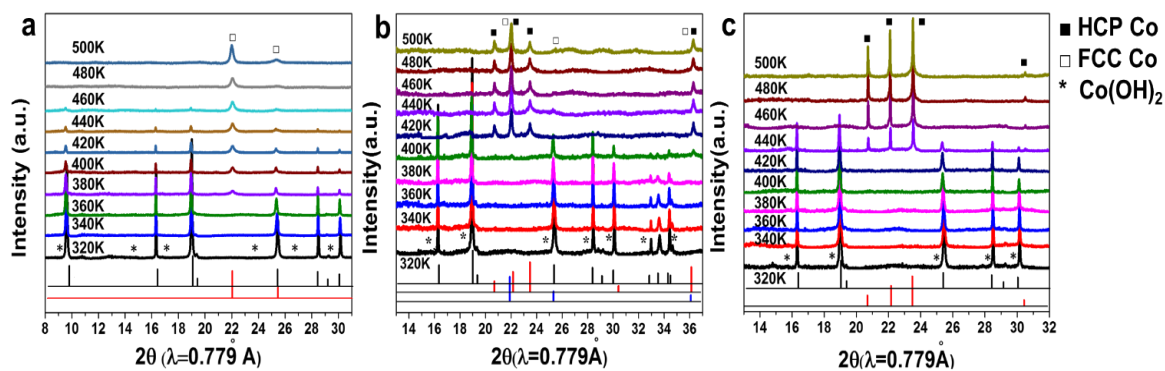
Figure 13 (a) *In situ* **XRD patterns of S4 without KOH addition, (b) S3 with 1g KOH addition, and (c) S1 with 4g KOH addition in 12 g EG solvent.**

By now, it can be concluded based on both experimental and computational results that the concentration of OH⁻ in solution, or say the pH level of the solution, is a critical factor that influence the stable phase obtained for Co nanoparticles via changing the surface energy by the capping effects of OH⁻. *Hcp* Co is more favorable under higher pH conditions, while *fcc* Co is more stable under neutral condition. This interplay between surface energy and total energy is expected to be general. It would be interesting to see such surface-controlled polymorphism can be observed with other capping agents other than OH⁻. Therefore, we designed experiments to use dioctyl sulfosuccinate sodium salt (AOT) (See Figure 14 for chemical structure of AOT) as an alternative capping agent to observe the polymorphism of Co. *In situ* solvothermal synthesis with using same Co source (Co(OH)₂) and solvent (EG) but without adding any KOH was carried out on the beam lines. The results, as shown in Figure 15, clearly show that with adding just 1 mmole AOT, which is a far lower concentration than that of KOH used in previous experiments, the synthesis yields pure *hcp* Co phase from nucleation stage. This clearly indicates that AOT has the same capability of varying the surface energy of Co clusters. Due to the selectively

bonding of AOT ligands with Co facets that lowers the surface energy, it results in an *hcp*

phase formation and growth. This experiment provides another proof of the feasibility and

effectiveness of tuning surface energy to vary the total energy and thus tune the

polymorphs.
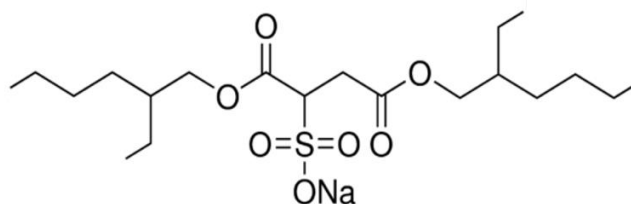
Figure 14 Chemical structure of AOT.
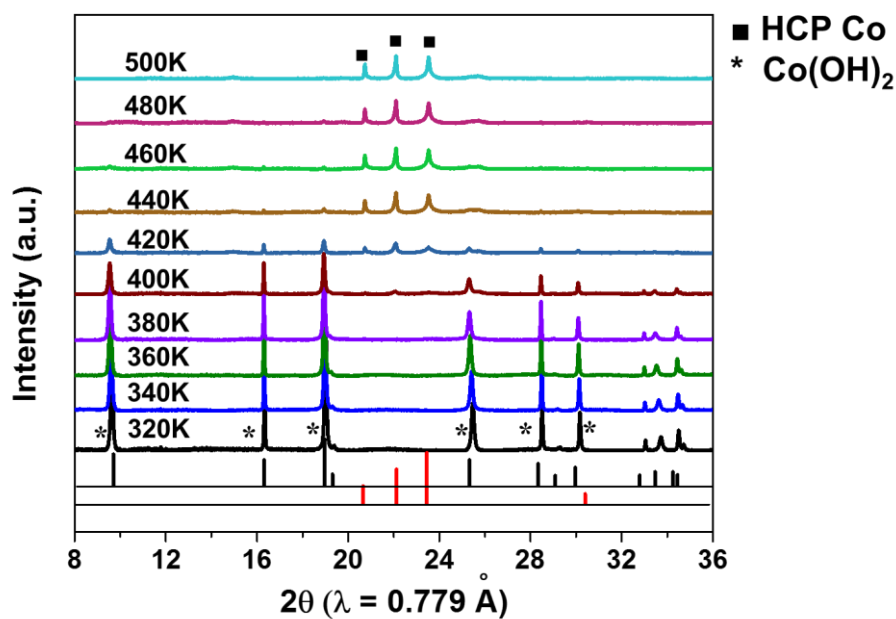
Figure 15 *In situ* XRD pattern of sample with 1 mmol AOT addition in 12 g EG solvent.

In this work we demonstrate that tuning the surface energy via capping ions can completely change the yielding polymorph for Co nucleation in solution. This tuning of polymorph is purely due to the change of surface energy and does not involve any stoichiometry change as Co is simple substance, which is different from previous works where such tuning is realized through changes in stoichiometry and composition. This indicates that surface energy by itself could be significant enough to vary the relative stability of different polymorphs. The tuning ability of the surface capping agents depends on both the energetics of the materials as well as the bonding/adsorption ability of the capping agents. One may expect that, if the difference in bulk energy of the polymorphs is too large, it would be difficult to alter the stable phase by solely changing the surface energy. However, surface energy may become significant as at the nucleation stage the particle size is very small. In this case, the difference between the ground state energy of the two polymorphs of Co capped with OH^- is at the scale of 0.25 kJ/mol[70] (corresponding to the transition temperature of 450 ℃), while the surface energy for a 1 nm nucleus under neutral condition (pH = 7), as computed, is 0.76 kJ/mol, which is more than three times higher. This implies that this surface energy tuning strategy may be effective for many other materials with even more significantly different energy among the polymorphs (i.e. higher polymorph cross-over temperature in simple heat treatment), considering using capping agents such as AOT with stronger surface bonding effect than OH^-. Polymorphism is very common in many important functional materials, such as TiO_2 (anatase, rutile, brookite), $CaCO_3$ (calcite, aragonite), and many electrode materials for alkaline metal ion batteries.[71,72] Synthesis of nanometric materials may benefit systematically considering the contribution of surface energy and controlling it accordingly. In fact, we have attempted to

tune the polymorphs of alloys. Similar tuning effects can be realized and will be published elsewhere. Such tuning method in principle can be applied to many more complicated crystalline materials, although the tuning factors may not necessarily be pH or AOT. Other factors such as the solvent or other ligands may be more sensitive and effective.

Another important factor is the bonding ability of the capping agents. When tuning the polymorph of Co with OH^-, at least 4g (or 70 mmol) of KOH was required to form pure *hcp* phase. However, use of only 0.016g (1 mmol) AOT yielded same pure *hcp* product in a 12 g EG solution. That is because the bonding between the surface Co atom and OH^- is relatively weak and very dynamic. A high concentration of OH^- is necessary to achieve enough coverage that can effectively change the energetics. As a contrast, the SO_3^- functional group in AOT has much stronger bonding with surface Co, due to the induction effect of sulfur.[73] Meanwhile, the much higher mass of AOT makes the adsorption much less dynamic and more stable. As a result, much lower concentration of AOT is needed to yield pure *hcp* Co. It is also worth noting, the use of capping agent in wet-chemistry syntheses is very common for the purpose of tuning the morphology of nanoparticles and nanowires. Yet in those cases, only the growth kinetics was varied due to the selective adsorption of the capping agent on different facets of the material. However, in this case, the formation of different phase-pure polymorphs was governed by thermodynamics, as demonstrated by the computational results and the *in situ* XRD observation.

More importantly, the nanometric phase diagram with particle size parameter has been established from DFT computation to evaluate and predict the stable phase in nucleation, and is demonstrated with accuracy and effectiveness in the case of Co. Although in more complicated solutions, more factors such as the competing effect of

different ligands and possible stoichiometry change and defects in the crystal need to be considered. As a grand vision, a database of nanometric phase diagrams as the function of particle size, chemical environment, and the concentration of the capping agent can be constructed to guide the synthesis of nanometric polymorphic materials.

2.4   Conclusion

In summary, we combined both experimental results and computational work to generalize an approach to understand the phase selection mechanism of Co polymorphs under solvothermal conditions. It was found that the surface energy was largely affected by the adsorbents, namely OH^-, from the solution. In competing with the bulk energy of particles, the surface energy plays an important role in determining the overall energy of the polymorphs for nanometric Co particles, resulting in the formation of various phases under different pH levels. The proposed driving force landscape of *fcc* and *hcp* Co could serve as a reference for selective synthesis of various polymorphs of nanoscale Co for specific applications. This method may be extended to other functional materials besides simple elemental materials, such as alloys, oxides, or carbonates.

CHAPTER 3.   AN *IN SITU* SYNCHROTRON X-RAY DIFFRACTION STUDY ON PHASE FORMATION OF COBALT NANOPARTICLES THROUGH ELECTRODEPOSITION METHOD

3.1   Introduction

Nanostructures have gained significant importance due to their numerous potential applications in various areas such as electronics, magnetism, biomedical engineering, energy storage, electrochemistry and beyond. A widely applied approach to synthesize various type of nanomaterials is electrodeposition, for that it is less expensive,[74] easier to scale up for mass production,[75] capable of producing uniform and dense film on complex shape substrate or templates within short time,[76] and more importantly, it has more parameters[77] (composition, pH, concentration, temperature, current density etc.) that can be controlled to produce different polymorphs or morphologies of nanoclusters. However, due to the fact that electrodeposition process involves multiple tunable parameters, and the fact that nanomaterials often deviates from their stable bulk phases resulting from the significant contribution from surface energy, a systematic understanding of how to synthesize desired polymorph using electrodeposition method is needed.

Another black-box that has been rarely explored is the polymorphism throughout nucleation till phase ripening during electrodeposition. Since the reaction is complicated in nature, which involves local pH change at working electrode with the proceeding of reaction,[78] which phase forms upon nucleation and what changes take place during ripening

34

process is of our great interests. Considering the technical difficulties that: (1) electrodeposition takes place very fast (usually within few seconds); and (2) the newly formed Co film has very weak signal that cannot be detected by in-house XRD; thereafter, we designed an *in situ* electrolytic cell made from acrylic glass, as shown in Figure 16, and use high-energy synchrotron *in situ* X-ray diffraction to enable real-time observation of polymorph formation throughout the reaction.
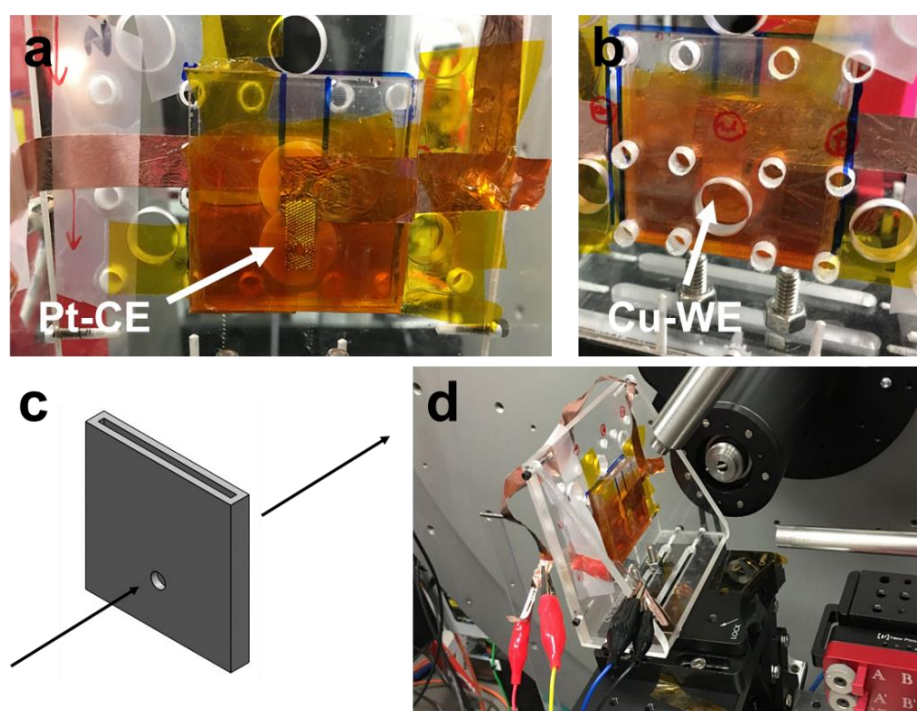
Figure 16 (a) Front view of electrolytic cell. A platinum mesh with a hole to let beam pass through was used as the counter electrode (CE); (b) Back view of electrolytic cell. A piece of copper foil was used as the working electrode (WE); (c) Schematic view of electrolytic cell. The outer dimension of the cell is 50 mm x 50 mm x 6.35 mm, with thickness of 2.175 mm and diameter of the hole is 5 mm; (d) Overview of final setup on beam line.

The advanced *in situ* X-ray diffraction (XRD) technique was employed to study the phase selection of Cobalt (Co) under various conditions including pH of the solution and over-potential. The metastable polymorph obtained in lower pH region and low over-potential was primarily driven by the surface energy contribution, which was theoretically quantified by DFT in our previous work (Chapter 2). On the other hand, due to higher kinetics of the reaction driven by over-potential, the metastable phase in lower pH region (i.e., *hcp* Co) can be obtained concurrently with the stable polymorph (i.e., *fcc* Co) upon nucleation. Therefore, we proposed the theory that the key drivers for phase selection of Co through electrodeposition include both thermodynamic factor - surface energy of the nanoclusters, and kinetic factor - over-potential. By tuning the condition, it is controllable to obtain the desired phase. We furthermore proved the feasibility of the theory by tuning phases selectively and forming layer-by-layer (LBL) Co revealed by *in situ* XRD observation. This work opens up opportunities for the design of functional electrodeposited materials rationally and introduce a new *in situ* technique for electrodeposition to track phase formation upon nucleation till phase ripening for the first time.

3.2   Methods

3.2.1   Electrodeposition synthesis

The base cobalt electrodeposition bath was composed of 0.5M cobalt sulfate pentahydrate (99.9%, GFS Chemicals) in 20 mL deionized water. 0.1M boric acid (99.5%, BDH Chemicals) and 0.1M sulfate acid (95-98%, BDH Chemicals) was added to the bath to examine the effect of pH on phase formation of Co. The chemical compositions are listed in Table 4. Four types of samples are investigated, including Co synthesized under neutral

condition (without adding boric acid and diluted sulfate acid, denoted as "N"); Co synthesized under mild acidic condition (adding boric acid but not diluted acid, denoted as "MA"); Co synthesized under acidic but low over-potential condition (adding boric acid and diluted sulfate acid, operating under low over-potential – with current density ranging below 15 mA/cm^2, denoted as "HA-LV"); and Co synthesized under acidic but high over-potential condition (adding boric acid and diluted sulfate acid but operating under high over-potential – with current density higher than 60 mA/cm^2, denoted as "HA-HV").

Table 4 Chemical composition of cobalt electrodeposition bath.

Bath Name	CoSO$_4$·5H$_2$O/M	H$_3$BO$_3$/M	H$_2$SO$_4$/M	Current density/mA·cm^{-2}	Deposition time/min
N	0.5	-	-	~10	20
MA	0.5	0.1	-	~12	20
HA-LV	0.5	0.1	0.1	~6	20
HA-HV	0.5	0.1	0.1	~65	20

A two-electrode system was used with a constant voltage electrodeposition process using a battery cycler (Arbin, BT2043). Copper foil with thickness of 0.005 inch and area of 2.5 cm^2 was used as the working electrode, while platinum plate with area of 0.25 cm^2 was used as the counter electrode. The current density between 6 to 65 mA/cm^2 of working electrode was controlled to investigate the effect of over-potential on phase formation.

3.2.2   Ex situ and in situ X-ray diffraction for the electrodeposition reaction.

Ex-situ laboratory XRD measurement was performed using a D8 Advance X-ray Diffractometer (Bruker AXS, Germany) with a Molybdenum radiation (λ Kα_1=0.7093Å). An *in situ* electrolytic cell was designed to study phase evolution under various conditions.

As mentioned previously, the samples are denoted as neutral (N), mild acid (MA), high acid low over-potential (HA-LV), and high acid high over-potential (HA-HV). Each of the sample was deposited for 20 min to form a homogeneous Co film with thickness around 25-30 µm to avoid the role of substrate in inducing topotaxial growth. *In situ* synchrotron XRD was conducted at 28-ID-2, National Synchrotron Light Source II and 17-BM-B, Argonne National Laboratory. The microstructure of Co nanoclusters, which were obtained after 1 min deposition to better visualize the primary particle morphology, was observed by Scanning Electron Microscope (Hitachi SU8010). All the electrochemical deposition and XRD measurements were conducted under room temperature (25 ℃).

3.3   Results and Discussion

3.3.1   *Ex situ study on selective phase formation of fcc and hcp Co.*

Among all the external factors that would affect phase selection of Co, pH of the solution and over-potential are two main factors that have been reported by a few works, yet with a conclusive theorem.[79,80] Therefore, a series of samples were prepared with various pH (0-1, 4-5, 6) and different applied voltage. The pH of the solution is adjusted by adding boric acid and diluted sulfate acid. Over-potential is controlled by adjusting the external voltage and therefore changes the current density applied at working electrode. The reactions at working electrode are:

$$Co^{2+} + 2e = Co, \qquad 2H^+ + 2e = H_2$$

The reaction at counter electrode is:

$$4OH^- - 4e = O_2 + 2H_2O$$
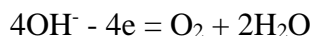
Figure 17 shows the *ex situ* X-ray diffraction (XRD) patterns of the samples. The strong peak around 19.8° is Cu substrate. When comparing the patterns of N, MA, and HA-LV samples that are obtained under low current density which minimizes the effect of over-potential, there is a clear trend that *hcp* Co is formed under relatively higher pH condition, while *fcc* Co forms under very low pH condition. The low intensity of *fcc* Co might result from the relatively thinner film obtained for HA-LV sample, which results from the lower current density, as shown in Table 4. However, if applying a high over-potential, which is 10 times higher than HA-LV in current density, there's a clear sign that *hcp* Co forms concurrently upon completion of the electrodeposition. It should be noted that the *hcp* (101) peak is not as strong as N and MA samples, suggesting that there's a preferred orientation for the *hcp* phase obtained from HA-HV sample. The co-deposition of *fcc* and *hcp* Co affect the orientation of *hcp* Co.

To understand why pH and over-potential could affect phase selection, the DFT study introduced in last chapter was applied to help reveal key factoring contributing to the overall energy of a single Co nanoparticle under various pH conditions by accounting for both bulk energy and surface energy, which is greatly affected by the pH of solution (Figure 10). It should be noted that the calculation is a more theoretical idealization, without considering the bulk defects, or the off − stoichiometry from particle segregation or agglomeration.

Figure 12 shows the energy difference between the two polymorphs accounting for pH effect only, which can be regarded as one of the main driving forces of phase formation. There is a clear trend that *hcp* Co is the more stable polymorph under relatively higher pH

for the nuclei with the size above 10 Å. On the other hand, the over-potential is closely related with reaction kinetics. According to Butler-Volmer equation,[81]

$$k \propto \exp[\frac{(1-\alpha)zF\Delta\phi}{RT}]$$

the rate constant k depends exponentially on the over-potential ($\Delta\phi$). Thereafter, it is possible to obtain concurrently of both metastable phase (*hcp*) under high acidic condition and the stable polymorph (*fcc*) with large enough over-potential, which further expediates the reaction. As a result, both stable polymorph (*fcc*) and metastable polymorph (*hcp*) can be obtained simultaneously under high over-potential condition.
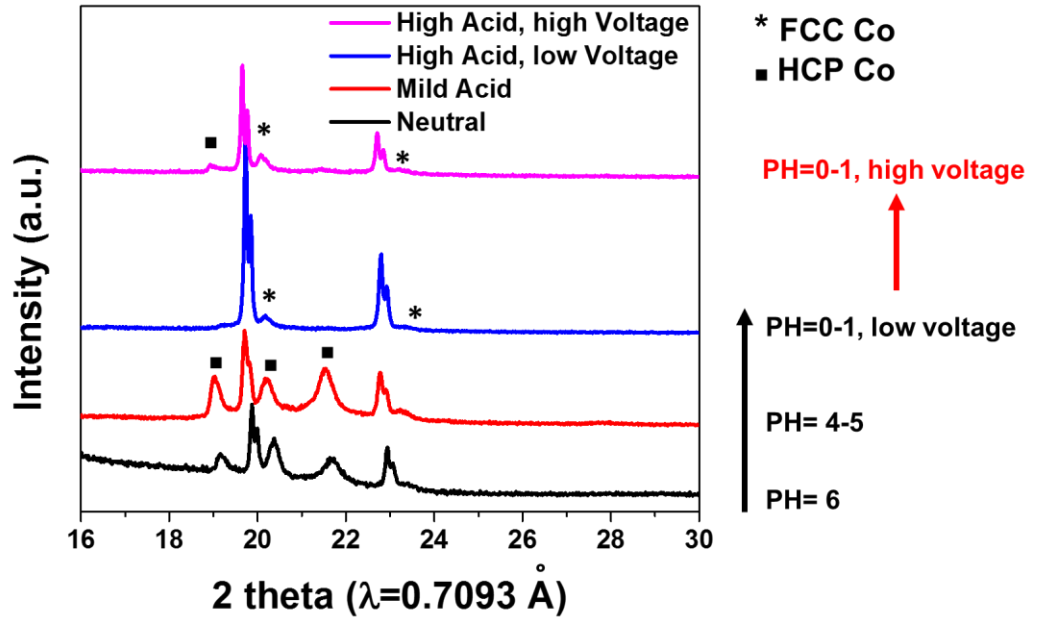
Figure 17 *Ex situ* XRD pattern of N, MA, HA-LV, and HA-HV samples under various pH conditions and different over-potential.

3.3.2   In situ study on phase formation of fcc and hcp Co.

The *ex situ* XRD results demonstrate the effect of pH and over-potential on phase selection of Co upon completion of phase formation and ripening. But a critical issue remains unsolved. What we have observed is the results after 20 min electrodeposition. Whether there is a phase transition during the process remains unknown. Therefore, it calls for the *in situ* observation to reveal the polymorph formation throughout the reaction. However, due to the challenge that electrodeposition happens within seconds, the in-house *in situ* XRD cannot serve the purpose to track the signal with satisfactory intensity. Thereafter, we design an electrolytic cell to be tested by *in situ* synchrotron XRD, of which one key advantage is the real-time observation by the 2D detector.

Figure 18 shows the *in situ* XRD patterns of N, MA, HA-LV, and HA-HV samples. As expected, the stable polymorphs concluded from previous discussion formed upon nucleation and no phase transition took place along the ripening process. There are two things should be noted: (1) The relative peak intensities of N and MA differ. For the latter case, the (002) peak of *hcp* Co, which locates around 6.6°, is much higher than the other two peaks, (100) at 6.2° and (101) at 7.1°. This preferred orientation phenomenon is likely to be correlated with the addition of boric acid,[82] which results in a different morphology – the needle-like primary particles (see Figure 19). However, the function of either additive is primarily affecting the morphology of nanoparticles, but won't affect phase formation; (2) The XRD pattern of HA-LV show that at the later stage of ripening, a minor *hcp* phase appear. It could be explained by our theory as well. With the gradual consumption of H^+ near working electrode, the local pH rises and results in the tendency of more *hcp* Co

nucleation. In comparison, the appearance of *hcp* Co of HA-HV sample forms upon nucleation, which can be explained by the kinetic impact of the over-potential. Using Scherrer equation, the particle size upon nucleation for *hcp* Co is 2 nm, while that for *fcc* Co is 1 nm. It should be noted that electrodeposition starts immediately upon charging, yet the peak signal at very early stage has much weaker signal so there are inevitable errors associated with full width at half maximum (FWHM), which is one factor for determining nucleation size.
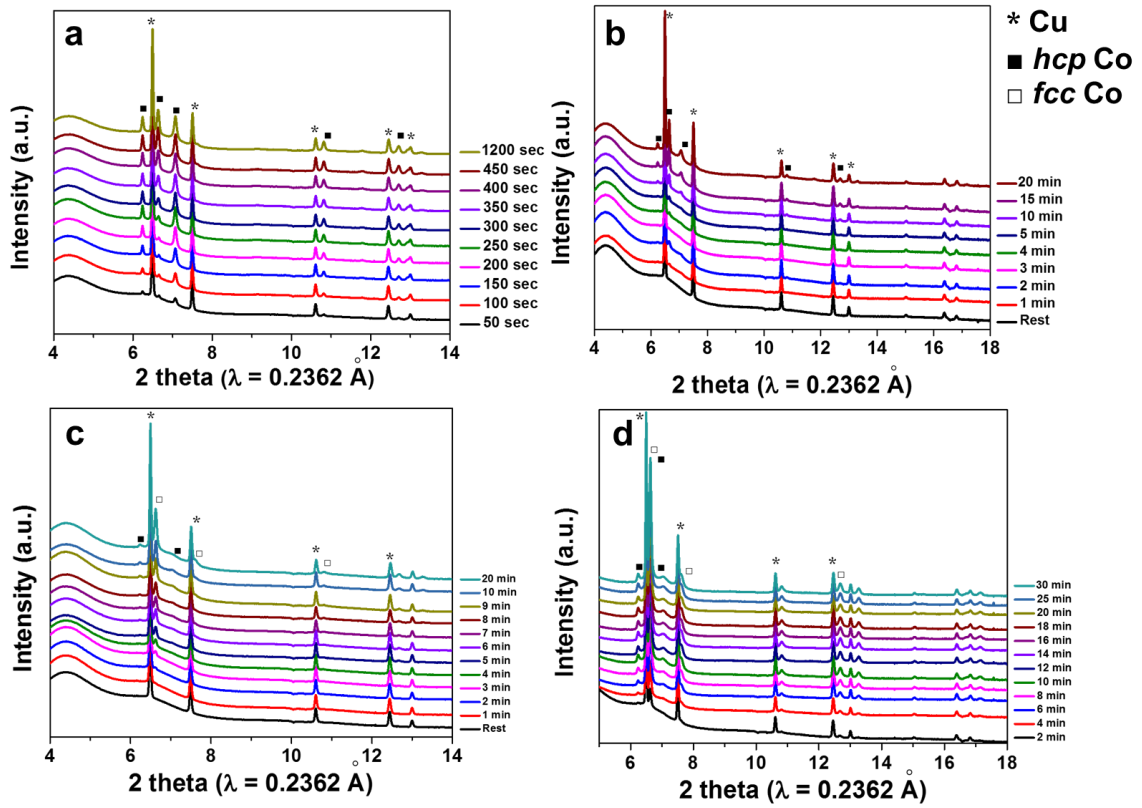
Figure 18 *In situ* **XRD of N (a), MA (b), HA-LV (c), and HA-HV (d) samples from nucleation to ripening process.**
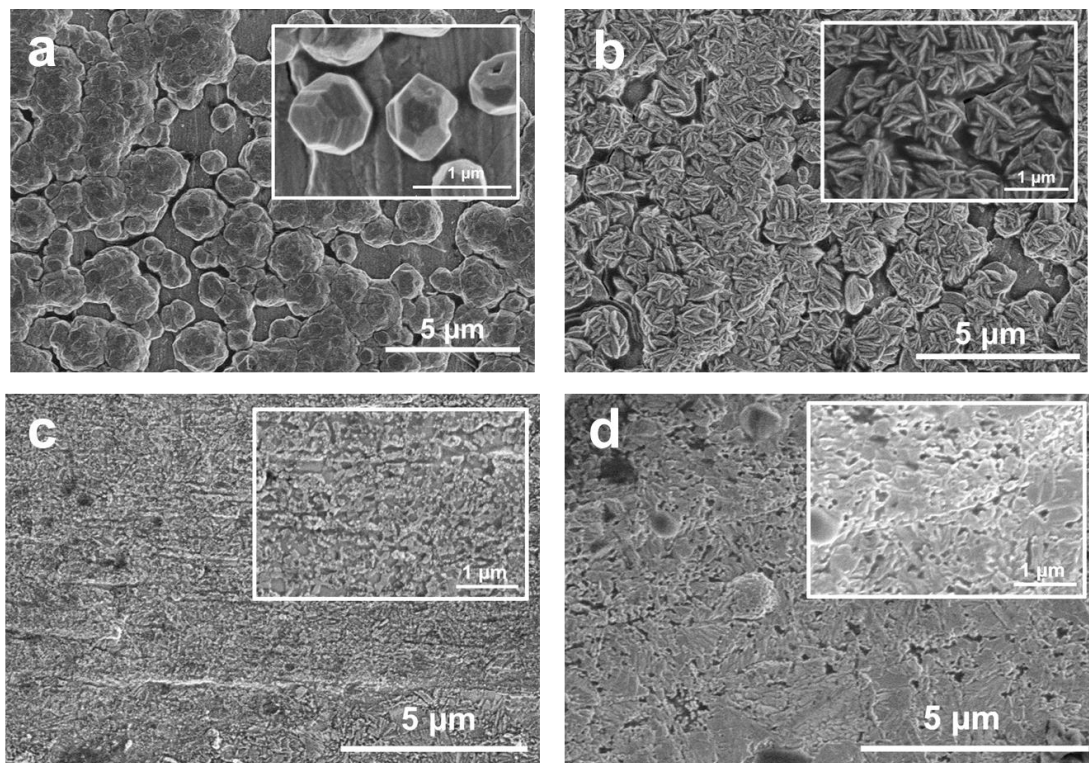
Figure 19 SEM images of N sample (a); MA sample (b); HA-LV sample (c); and HA-HV sample (d) after 1 min deposition. The blank substrate is copper foil. Scale bars are 5 μm. Insets are the zoom-in view with scale bars of 1 μm.

3.3.3   In situ study on phase tuning to get layer-by-layer (LBL) Co.

To further prove the applicable importance of our previous work, we conducted layer-by-layer deposition of Co by tuning over-potential on a single system. To avoid the side-effect from local pH change, we chose neutral sample under low over-potential (current density 10 mA/cm^2) as a starting point. After 5 min deposition, we switched the external voltage to high over-potential (current density 80 mA/cm^2) to see if the concurrent deposition can be achieved manually. Figure 20 shows the *in situ* XRD pattern of the two-step process. The *hcp* Co forms first, as expected. After switching to high over-potential around 5 min, the *fcc* phase starts to appear. Though the signal of minor *fcc* phase is weak,

there are two signs that show the co-deposition of *fcc* Co. First, the peak around 7.6° is a signature peak of *fcc* Co (200). The broad width of the peak suggests that the size of the *fcc* nanocluster is relatively small, which is due to the fact that acidic condition would reduce the amount and slows down the rate of Co reduction as H^+ has higher reduction potential than Co^{2+}. Second, the relative peak intensity near 6.6° is much higher than the other two *hcp* peaks (100) and (101), at 6.2° and 7.1° respectively, if we compare the previous *in situ* XRD pattern of neutral sample (Figure 18a). This peak is the overlapping of *hcp* (002) and *fcc* (111) of Co. The relative peak intensity suggests the coexistence of the two phases.

By far, we have used one example to demonstrate the feasibility of tuning Co phases through electrodeposition by changing the conditions. It is reasonable to claim that other multilayer structures with interesting mechanical or magnetic properties can be obtained by referring to the phase selection theory we have proposed in this work.
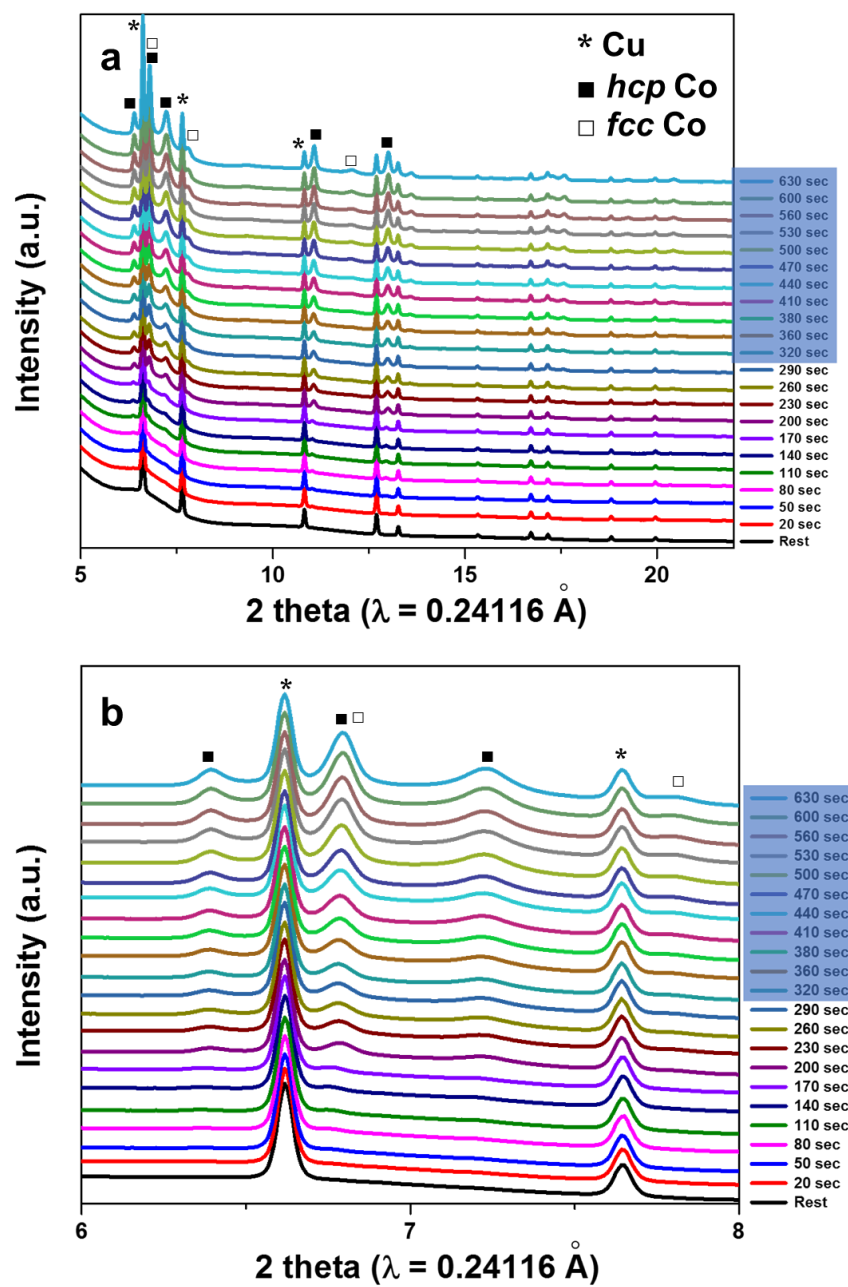
Figure 20 (a) *In situ* **XRD pattern of layer-by-layer Co neutral sample. The first 5 min is under low over-potential while the next 5 min is under high over-potential; (b) The zoom-in of patterns. The blue color blocks indicate the time when high over-potential is applied.**

3.4   Conclusion

In this work, we have demonstrated the phase selection mechanism of Co through electrodeposition by combining both *ex situ*, *in situ* XRD and DFT computation. It was found that *hcp* Co prefers to form under higher pH condition, while *fcc* Co prefers to form under lower pH condition. The key driver for this pH-control phase selection is that surface energy is highly pH sensitive and it contributes drastically to the overall ground state energy. Over-potential is another factor affecting phase selection by boosting the kinetics of the polymorph formation, resulting in co-deposition of both stable and meta-stable polymorphs. The aforementioned mechanism can serve as a foundation for the synthesis of multi-layer Co structure, as we have demonstrated using over-potential control.

CHAPTER 4.   A STUDY ON PHASE SELECTIVITY OF COBALT-NICKEL ALLOY NANOPARTICLES THROUGH AN *IN SITU* ELECTRODEPOSITION METHOD.

4.1   Introduction

Binary alloys have always been an important component in industrial application. Nowadays, more than 200 binary alloys are used in industry.[83] Among them, magnetic alloys are important functional materials that are fundamental in microelectronics, computer technology, coating industry, biotechnology application etc.[84,85] Cobalt (Co) – Nickel (Ni) is one magnetic alloy that is widely used not only as functional coating for its corrosive and resistance property, but also plays an important role in microelectronics for its magnetic properties.[86] Co and Ni can alloy at all composition, according to their phase diagram, resulting in a tunable property that could be useful for both hard and soft magnetics.

Electrodeposition is a common approach to obtain Co-Ni alloy due to its high degree of control obtainable by varying the experimental conditions. Many previous work have synthesized Co-Ni under different electrolytes (pH, surfactant, pH buffer etc.) and varying deposition condition (current density, time etc.) to obtain desired property.[87,88] However, we rarely see a systematic study on the fundamental of phase formation for Co-Ni, which is the key controlling factor of their properties.

In this work, we applied the same *in situ* synchrotron X-ray diffraction (XRD) technique to study phase formation under nanometer scale for bimetallic system through

electrodeposition, as the second step based on the findings through single element system. By studying Cobalt (Co) – Nickel (Ni) system, we found out that there are 3 factors contributing to phase formation. Intrinsically, the composition of starting materials affects the stable polymorph obtained; extrinsically, the pH of the electrodeposition solution and over-potential could alter the stable polymorph to some extent by tuning surface energy or kinetics of the reaction. For the same composition, the lower pH of the solution, the more likely *hcp* phase is to be obtained; the higher over-potential, the more likely unstable polymorph is to concurrently form. However, we also found out due to the complexity of bimetallic system, the extent to externally tune the polymorph varies with different composition. The compositions that lie within *hcp* and mixture (*hcp* & *fcc*) in the original bulk Co-Ni phase diagram can be tuned easier. Overall, all the reactions were observed through *in situ* synchrotron XRD and it was found out that no phase transition occurred during the reaction, suggesting the phase tuning strategy was effective from nucleation stage. This work opens up opportunities for the study of more complex system, by demonstrating the three key factors contributing to polymorph formation. It also justifies the broad applicability of *in situ* electrodeposition method we developed to study multi-element systems in the future.

4.2   Methods

4.2.1   Electrodeposition synthesis

The electrolyte composes of 0.5 M cobalt sulfate pentahydrate (99.9%, GFS Chemicals) and nickel chloride hexahydrate (98%, Sigma-Aldrich) in total with various starting molar ratio in 20 mL aqueous solution (i.e., CoNi6040, CoNi5050, CoNi4060,

CoNi3070). The pH control of Co-Ni5050 and CoNi6040 were obtained through the addition of 0.5 M boric acid, and 0.1 M diluted sulfate acid into the 0.5 M starting material solution. The overpotential variable was investigated by using CoNi4060, CoNi5050, and CoNi6040 to see the effect of kinetic factor on phase selection, with the current density ranging from $10 - 110$ mA cm^{-2}.

4.2.2 Ex situ and in situ X-ray diffraction for the electrodeposition reaction.

Ex-situ laboratory XRD measurement was performed using a D8 Advance X-ray Diffractometer (Bruker AXS, Germany) with a Molybdenum radiation (λ Kα_1=0.7093Å). An *in situ* electrolytic cell was designed to study phase evolution under various composition, under various pH condition for different sample, or under various over-potential condition for different samples. Each of the sample was deposited for 20 min to form a homogeneous Co-Ni film with thickness around 25-30 µm to avoid the role of substrate in inducing topotaxial growth. *In situ* synchrotron XRD was conducted at 28-ID-2, National Synchrotron Light Source II and 17-BM-B, Advanced Photon Source. All the electrochemical deposition and XRD measurements were conducted under room temperature (25 ℃).

4.2.3 Composition characterization

Inductively coupled plasma mass spectrometry (ICP-MS) (Agilent 7500a series) was used to determine the actual composition of post-deposited Co-Ni samples with various starting ratio. Aliquots were diluted in 2% trace metal grade HNO$_3$ (Fisher Scientific, Inc.) containing 20 ppb indium as an internal standard to correct for instrument drift. Calibration standards were prepared with a certified stock solution (SPEX CertiPrep) in 2% HNO$_3$

containing the internal standard and measured approximately every 15–20 samples as quality controls. Energy-dispersive X-ray spectroscopy (EDX, Zeiss Ultra 60) was used to map out Co-Ni elemental distribution and their relative ratio of CoNi5050 samples under different pH and over-potential conditions.

4.3 Results and Discussion

4.3.1 *Ex situ results on electrodeposited Co-Ni alloy with various starting composition.*

There are 3 key factors for investigation, i.e., composition, pH, and overpotential. Thereafter, a serial of laboratory synthesis with using control-factor approach was conducted as a fundamental to understand the polymorph formation mechanism at room temperature. The electrolyte composes of 0.5 M cobalt sulfate pentahydrate (99.9%, GFS Chemicals) and nickel chloride hexahydrate (98%, Sigma-Aldrich) in total with various starting molar ratio in 20 mL aqueous solution (i.e., CoNi6040, CoNi5050, CoNi4555, CoNi4060, CoNi3070). The pH control of one composition, Co-Ni5050 was obtained through the addition of 0.5 M boric acid, and 0.1 M diluted sulfate acid. The overpotential variable was investigated by using CoNi4060, CoNi5050, and CoNi6040 as examples to see the effect of kinetic factor on phase selection, with the current density ranging from 10 – 110 mA cm^{-2}. The detailed composition is summarized and shown in Table 5. Each reaction takes 20 min to ensure getting a uniform film with good-quality x-ray signals.

Table 5 Summary of various ex situ laboratory synthesis of Co-Ni alloy nanoparticles.

	CoSO$_4$/M	NiCl$_2$/M	Co:Ni	Boric acid/M	Diluted Sulfate/M	Current density/ mA cm^{-2}	Notes
1	0.3	0.2	60:40	-	-	10	Composition Control
2	0.25	0.25	50:50	-	-	10	
3	0.2	0.3	40:60	-	-	10	
4	0.15	0.35	30:70	-	-	10	
5	0.25	0.25	50:50	0.5	-	12	pH control
6	0.25	0.25	50:50	0.5	0.1	13	
7	0.25	0.25	50:50	-	-	25	Overpotential control
8	0.25	0.25	50:50	-	-	40	
9	0.25	0.25	50:50	-	-	110	

Figure 21 shows the trend of varying composition of Co-Ni alloy while keeping the electrolyte pH as neutral and overpotential low to minimize the influence of surface energy and kinetic factor, respectively. It can be seen clearly that with increasing amount of Ni, the bimetallic nanoparticles gradually change from pure *hcp* phase to a mixture of *hcp* and *fcc*, then eventually, to pure *fcc* phase. Interestingly, the peak (002) ($2\theta = 20.5°$) of CoNi6040 has the lowest intensity, suggesting a possible preferred orientation in this case. The trend indicates that with increasing amount of Ni in the composite, the more tendency it has towards formation of *fcc* phase, for that *hcp* Ni is a metastable phase and can only be synthesized under certain condition.[89,90] However, a key question for this batch of tests is that whether the as-synthesized composite has the same ratio as starting materials, for that Co and Ni have slightly different reduction potential and according to anomalous co-deposition theory,[91] there is a difference in kinetics as well. Therefore, we conducted ICP-MS tests for this batch, to elucidate the composition of as-synthesized samples (Table 6).

Rietveld refinements was carried out on pure phase samples (e.g., CoNi6040, CoNi5050, and CoNi3070) to further prove whether the as-synthesized composites are solid-solution, and the results are summarized in Table 7. It was found that for the pure phases we obtained, *hcp* or *fcc*, all of which are solid-solution with less than 0.4% error when comparing the refinement value with the one applying Vegard's law:[92]

$$a_{A_{(1-x)}B_x} = (1-x)a_A + xa_B$$

where:

a_A and a_B are the lattice parameters of the pure elements, A and B.

x is the molar ratio of B in the solid solution.

$a_{A_{(1-x)}B_x}$ is the lattice parameter of the solid solution.

In summary, we have concluded that under nanoscale neutral condition, the rough boundary limit of *hcp* Co-Ni is Co 77% (a.t.) and the boundary of *fcc* Co-Ni is Co 64% (a.t.), in accordance with Co-Ni bulk phase diagram (Figure 3).
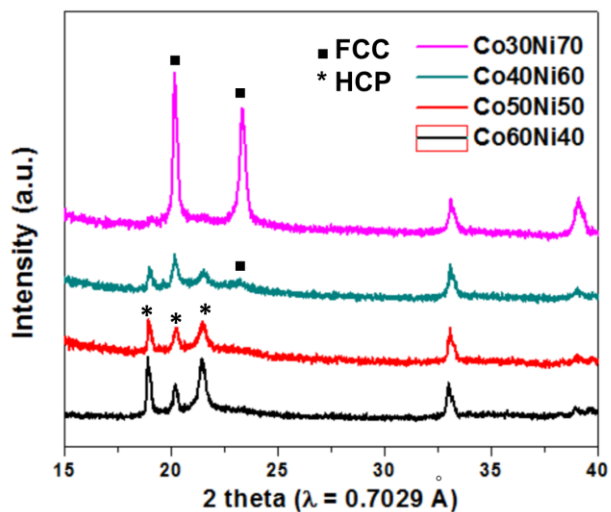
Figure 21 XRD patterns of Co-Ni with various composition under neutral, and low-overpotential condition.

Table 6 ICP results of various composition of CoNi samples

Sample type	Dilution Factor	Standard	Co/ppb	Ni/ppb	Co:Ni	Actual Composition	Polymorph
60:40	2	19975970.0	235.63	54.06	4.359		
60:40	2	19963330.0	230.55	53.71	4.292	$Co_{85}Ni_{15}$	*hcp*
60:40	4	19826390.0	247.49	57.61	4.296		
50:50	50	20482140.0	2411.05	918.11	2.626	$Co_{77}Ni_{23}$	*hcp*
50:50	100	20702700.0	2719.84	1022.33	2.660		
40:60	50	20162390.0	2758.43	1189.12	2.320		*hcp + fcc*
40:60	20	19895130.0	2459.50	1087.82	2.261	$Co_{75}Ni_{25}$	(very minor)
40:60	100	20607740.0	1854.41	789.86	2.348		
30:70	50	19854520.0	2574.17	1861.76	1.383	$Co_{64}Ni_{36}$	*fcc*

Table 7 Rietveld Refinement results of CoNi with various composition

Sample Type	Actual Composition	wRp	Rp	CHI2	a,b/Å	Error	c/Å	Error
60:40	Co85Ni15	0.1278	0.0971	1.913	2.517	0.32%	4.095	0.32%
50:50	Co77Ni23	0.099	0.0727	1.853	2.531	0.23%	4.116	0.24%
30:70	Co64Ni36	0.1019	0.0787	2.459	3.546	0.31%	3.546	0.31%

4.3.2   In situ results on electrodeposited Co-Ni alloy with various starting composition.

The ex situ results on various composition demonstrates the "intrinsic" factor that have impacting phase formation of Co-Ni system. Based on the previous work, it is necessary to observe the phase formation process starting from nucleation upon phase ripening to confidently discuss other factors that might affect phase formation, without considering phase transition during reaction. Therefore, we conducted two *in situ* tests of CoNi5050 and CoNi3070 samples at 17-BM-B, APS, by using the *in situ* electrolytic set up discussed in Chapter 3. Figure 22 shows the results we obtained, with Figure 22a and Figure 22b demonstrate CoNi5050 while that of Figure22c and d show the result of CoNi3070. As can be seen, the reactions, regardless of producing *hcp* or pure *fcc* solid solution, start from nucleation. The signal can be observed starting from about 2-3 min, and the intensity keeps increasing afterwards. For CoNi5050 sample, (002) peak demonstrates the highest intensity from nucleation, suggesting that the preferred orientation is not affected by later kinetic factor but from the beginning stage. With these two polymorphs' results, we could speculate that other Co-Ni series sample would have

similar mechanism, which is forming the final phase upon nucleation, without phase transition.
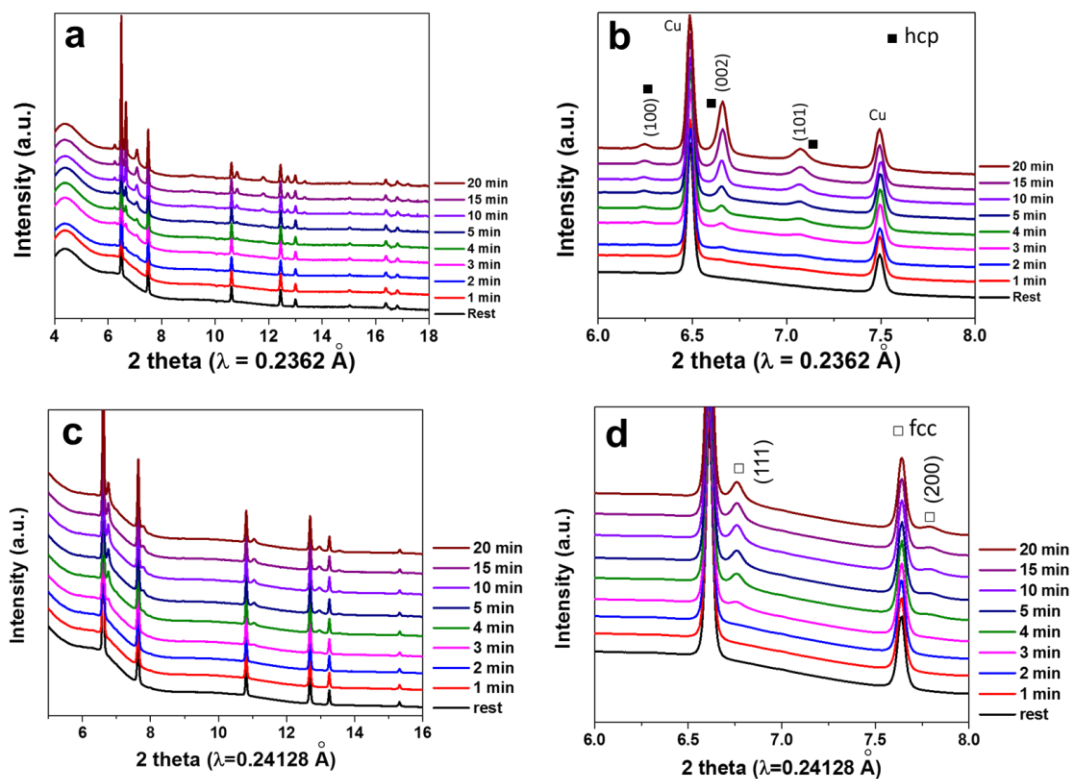
Figure 22 *In situ* XRD of CoNi5050 (a) & (b) and CoNi3070 (c) & (d) samples from nucleation to ripening process.

4.3.3   Ex situ results on electrodeposited Co-Ni alloy with different pH of the solution.

The composition mainly determines the stable polymorph (the one with lowest bulk energy) without impact of external factors. A natural thought to explore as next step is to study external factors that might potentially tune the Co-Ni polymorph, including thermodynamic and kinetic factors.

In Chapter 2 and 3, we discussed how surface energy of Co would affect the total energy for nanometric particles. Based on this, we conducted an experiment on CoNi5050 to see if that also works for the bimetallic system. As can be shown in Figure 23, under neutral condition, the stable phase is *hcp* solid solution, as expected. However, under highly acidic condition, the only phase we observed is *fcc,* suggesting that the pH of the solution might affect the alloy in the similar way as with Co system. Under acidic condition, the stable polymorph for Co is *fcc*, for the reason that the surface energy of *fcc* is much lower under that pH regime. Since Co-Ni will alloy together instead of separate as two phases, and Ni *fcc* is the more stable phase compared with *hcp* Ni, therefore, we could speculate that the *fcc* bimetallic system has a much lower total energy under this condition. This also demonstrates another approach to obtain *fcc* Co-Ni starting from metastable *fcc* composition regime.
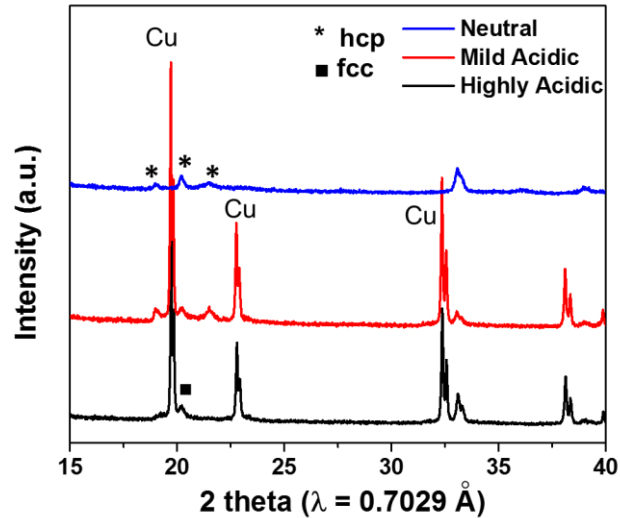
Figure 23 Ex situ XRD patterns of CoNi5050 sample under various pH conditions.

4.3.4 *In situ results on electrodeposited Co-Ni alloy with different pH of the solution.*

Two starting compositions were chosen to study the pH effect of phase formation, CoNi6040 and CoNi5050. Since $Co(OH)_2$ and $Ni(OH)_2$ has little solubility in aqueous solution, therefore, our strategy is to tune the pH to lower range and see how this would affect the obtained polymorphs.

As can be seen in Figure 24, both CoNi6040 and CoNi5050 samples show the appearance of *fcc* phase, which is the metastable polymorph without introducing external factors for this composition. Furthermore, CoNi6040 shows a little mixture of *fcc* within the majority of *hcp* phase, while CoNi5050 can be fully tuned to *fcc* solid solution. We think this is mainly due to the competing effect of bulk energy of Co-Ni system and the change in surface energy. For the former case, the bulk phase of *hcp* is more stable, as it is farther away from the two-phase region on Co-Ni phase diagram. Therefore, tuning the surface energy would have less effect compared with the latter case. However, these two examples still show that pH could be one external factor that help tuning the phase in Co-Ni system.
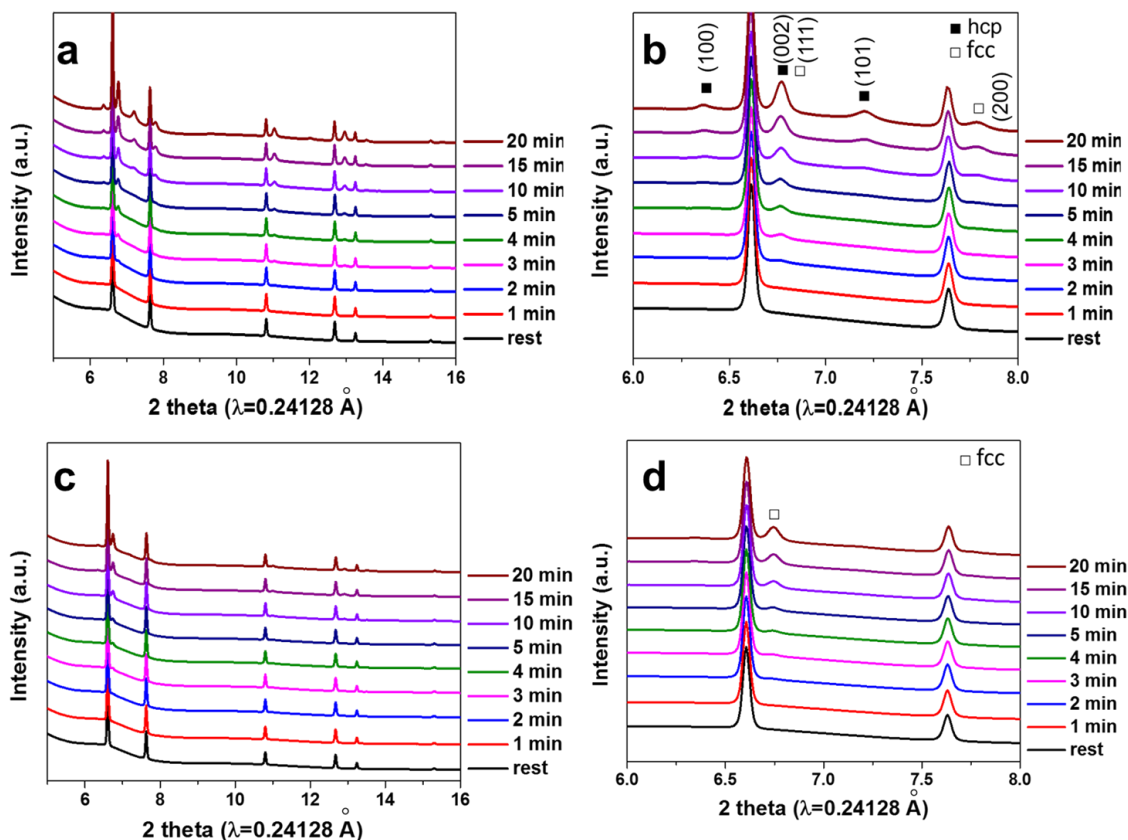
Figure 24 *In situ* **XRD of CoNi6040 (a) & (b) and CoNi5050 (c) & (d) samples under acidic condition from nucleation to ripening process.**

4.3.5   Ex situ results on electrodeposited Co-Ni alloy with different over-potential.

Aside from external thermodynamic factor, another key factor that might come into play for electrodeposition is over-potential. By changing the kinetics of electrodeposition, it is possible to obtain metastable phase concurrently with the stable one under certain composition regime. Therefore, we conducted two tests on CoNi5050 and CoNi4060 under neutral condition but with various over-potential, as shown in Figure 25. For CoNi5050, the stable phase is *hcp*, however, with increasing over-potential, there is a gradual appearance of the metastable *fcc* phase. In comparison, for the case of CoNi4060, which locates in the regime that is closer to *fcc* solid solution in bulk phase diagram, the trend is

more obvious than CoNi5050. By increasing current density of about 4 time, a pure *fcc* phase could be obtained, suggesting that *fcc* phase grows faster in this case, and kinetics factor surpass the thermodynamic factor. As a conclusion, over-potential could be another approach to control the phase formation, and the impact it has on different composition varies, depending on the regime of the starting material composition.
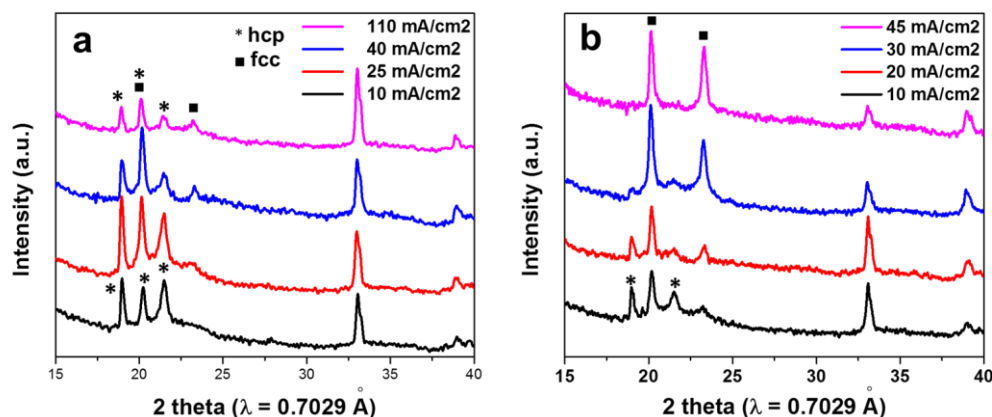
Figure 25 Ex situ XRD patterns of CoNi5050 (a) and CoNi4060 (b) samples under various over-potential conditions.

4.3.6   In situ results on electrodeposited Co-Ni alloy with different over-potential.

A series of *in situ* XRD tests were done on multiple composition, including CoNi6040, CoNi5050, and CoNi4060. It is necessary to track if the concurrent formed phase occurred in later stage during the process. In addition, by studying compositions that span across different regime on Co-Ni phase diagram, the impact of over-potential could be revealed as well. As shown in Figure 26, CoNi6040 shows the appearance of *fcc* metastable phase upon nucleation and eventually takes quite a portion in the final product. CoNi5050 is following the similar trend, yet with even higher ratio of *fcc* phase. In the case of CoNi4060, the final product is almost pure *fcc* phase. All of which demonstrate the effect

of over-potential on the final product of the system, which increases with approaching *fcc* regime on bulk phase diagram. No phase transition takes place during the reaction.
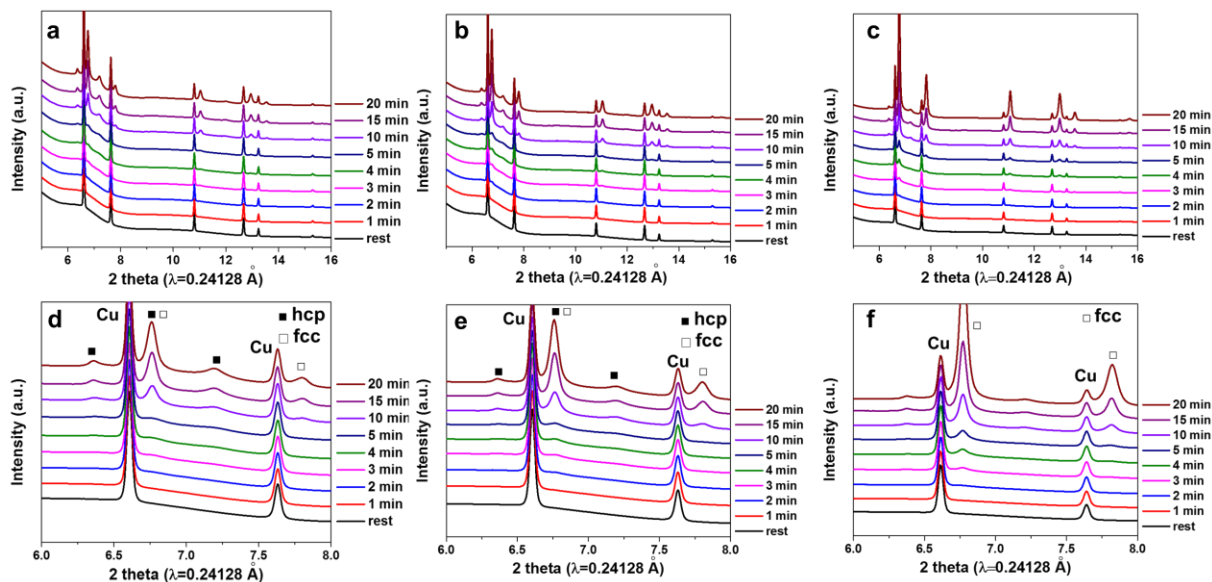
Figure 26 *In situ* XRD of CoNi6040 (a) & (d), CoNi5050 (b) & (e), and CoNi4060 (c) & (f) samples under high over-potential from nucleation to ripening process.

4.3.7   Composition of CoNi5050 samples under different pH and current density.

EDX was conducted for CoNi5050 sample under acidic condition and high current density to reveal the new actual composition after reaction. As shown in Figure 27, the distribution of Co and Ni is homogeneous without any segregation, suggesting a solid-solution alloy. According to the analysis, the CoNi5050 under acidic condition has a composition of $Co_{62}Ni_{38}$ while that under high current density has a composition of $Co_{62}Ni_{38}$ as well. The standard deviation of the above elemental analysis is 0.3% and 0.2%, respectively. The results are in accordance with the XRD observations: with reduction in pH of solution or higher current density, the ratio of *fcc* solid solution would increase. And based on the previous results, the *fcc* is Ni-rich phase. Therefore, the shift from $Co_{77}Ni_{23}$

to $Co_{62}Ni_{38}$ for these two samples suggesting the possibility of tuning post reaction composition of Co-Ni alloy.
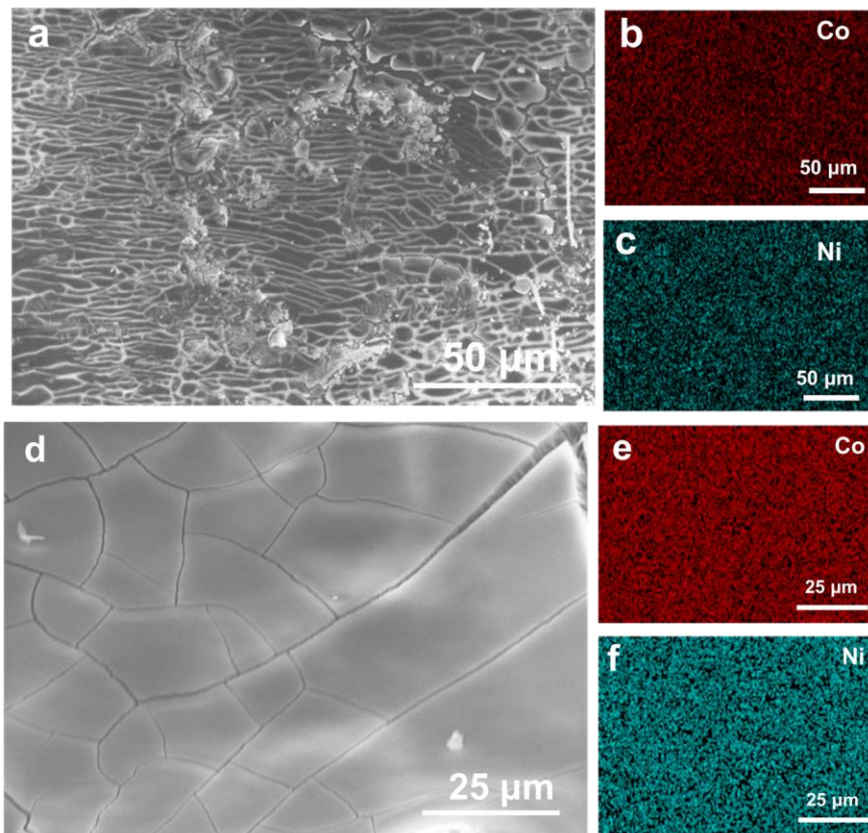
Figure 27 EDX results of CoNi5050 sample under acidic condition (a-c) and high current density condition (d-f).

4.4 Conclusion

In this work, we take one step further and explore phase formation of Co-Ni bimetallic system through ex situ and *in situ* electrodeposition. By introducing another element, there are three key factors that would affect phase formation. Internally, the initial starting ratio of Co and Ni would affect the bulk energy of obtained phase, so as to obtain solid solution that are in accordance with bulk phase diagram. Externally, the pH of the

solution and over-potential would tune phase formation as well. By reducing pH of the solution, the metastable *fcc* phase of CoNi at stable *hcp* dominant phase diagram region would form, mainly due to the contribution of surface energy. By increasing over-potential, the metastable phase could be concurrently obtained by expediated kinetics, and the effect is more severe as the composition moves more towards mixture region. *In situ* XRD was conducted to reveal that the different phase formation behavior originates from nucleation upon phase ripening. Therefore, it could be concluded that, by selectively tuning the factors for CoNi system, as an example, the final deposited phase could be tuned accordingly. This work paves the way for exploring other bimetallic system or even multi-element system.

CHAPTER 5.   FACILE AND SCALABLE ELECTRODEPOSITION OF COPPER CURRENT COLLECTORS FOR HIGH-PERFORMANCE LI-METAL BATTERIES

5.1   Introduction

One key advantage of electrodeposition is that it could tune the morphology of as-synthesized particles through the appropriate addition of additives. This particularly shed light on material synthesis for energy storage application (e.g., lithium ion batteries), for that the electrochemical performance of electrodes is closely related with its morphology.[93,94] A recent popular trend on modification of Copper (Cu) current collector of lithium metal batteries inspires us to investigate a synthesis of 3-D Cu current collector with suitable morphology that can effectively suppress the formation Li dendrite through electrodeposition.

With the growing needs for rechargeable batteries with ultrahigh energy densities for portable electronics, electric vehicles, and electrical grids, research efforts beyond conventional Li-ion batteries, such as Li-S,[95] Li-O$_2$,[96] and solid-state batteries[97,98] have been thriving in the last decade. Among the approaches, Li-metal batteries attract a lot of attention, where Li-metal is used as the anode while the cathodes of Li-ion batteries are still used.[99,100] This approach adapts the mature cathode technology from Li-ion batteries and focuses on solving the problems in Li-metal anode, e.g., the dendrite growth and low cyclability.[101–103] This approach not only has the potential for very high energy density, benefiting from the high capacity of Li-metal anode (3840 mAh g^{-1}), but also has the

advantage that it does not need to address the problems in cathode side as Li-S or Li-O$_2$ batteries do.

The problems of Li-anode are, however, very challenging. Besides the well-known safety problem,[104] stripping of Li from the root of the dendrites also results in electrical isolation of some small Li metal pieces (i.e., the "dead Li"[105]) and thus low Coulombic efficiency. A widely accepted model for Li dendrite growth is the space charge model.[106] When the local current density J at the anode exceeds the diffusion-limited value J^*, limitation in mass transport results in depletion of ions near the surface of the electrode, creating a space charge layer and a strong local electric field, which accelerates a local deposition or dendritic growth of Li. The space charge theory, however, cannot explain the occasional dendrite growth in low current below J^*. Another model[107] indicates dendrites can also grow at nucleation sites where local resistivity is low, i.e. areas with good SEI or defects.

Tremendous efforts have been made to address the challenges regarding suppression of Li dendrite and stabilization of SEI, including 1) electrolyte engineering;[108–112] 2) interfacial engineering;[113–120] 3) use of solid electrolyte,[121–123] and 4) use 3-D structured current collectors.[124-137] Among these promising approaches, interfacial engineering and the use of 3-D current collector represent some new promise. Compared to flat foil current collectors, 3-D structured current collectors have much larger active surfaces area, thus effectively reduce the actual current density J for the same apparent current and lower the possibility of stimulating dendritic growth. Many 3-D structures of current collectors have been demonstrated to have positive effects to mitigate Li dendrite growth (as shown in Figure 28), such as 3D submicron Copper (Cu) skeleton,[124] free-standing Cu nanowires

(NW),[125] hollow carbon fibers,[126] graphitized carbon fibers,[127] de-alloyed 3D porous Cu,[128] vertically aligned Cu microchannels,[129] crumbled graphene balls,[130] pie-like porous Cu NW/graphene,[131] carbon fiber papers,[132] nitrogen doped graphene,[133] nitrogen doped graphitic carbon foams,[134] direct growth of 3-D carbon host[135], compact 3-D copper paper[136], and oriented graphene foams.[137] Interfacial modification is usually realized by introducing heterogeneous nucleation sites by coating conductive materials (e.g., hollow carbon spheres with nanoparticles seeds inside,[138] Li-rich composite alloy films[139]) or insulating layers (e.g., glass fiber cloth,[140] poly(dimethylsiloxane)[141]) to facilitate the simultaneous plating of Li on the modified surface.
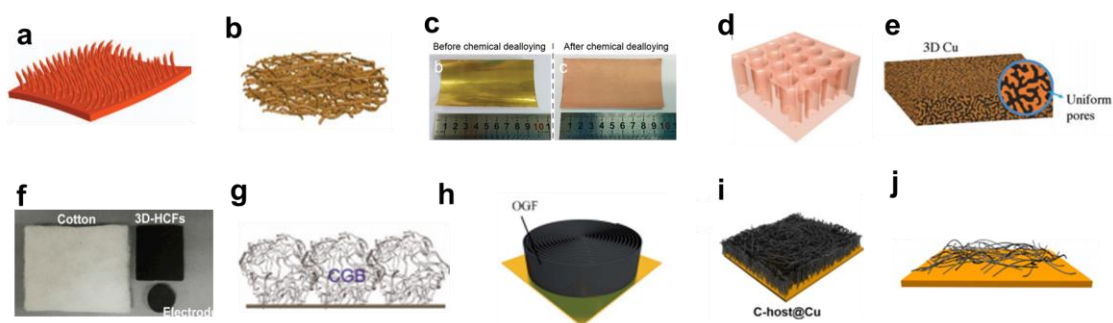
Figure 28 Selected examples of 3-D current collectors. (a) 3-D submicron Cu [124]; (b) Cu nanowires [125]; (c) de-alloyed 3-D porous Cu [128]; (d) vertically-aligned Cu microchannels [129]; (e) 3-D Cu obtained through electrochemically etched Cu-Zn tape [136]; (f) hollow carbon fibers [126]; (g) crumbled graphene balls [130]; (h) oriented graphene foam current collectors [137]; (i) carbon-host on Cu current collector[135]; (j) carbon nanofiber film on Cu current collector [132].

Inspired by the reported work and our previous efforts on electrodeposition, we propose a facile and scalable method to produce a 3-D Copper (Cu) current collector that could be applied in large scale of the current roll-to-roll battery manufacturing process. The aforementioned 3D current collector strategies demonstrate promise by increasing nucleation sites, yet most of these successes are in lab-scale with coin cells and most of the

methods are sophisticated and expensive, not scalable and not compatible with mass manufacturing processes of current Li-ion battery industry. For example, the synthesis of Cu nanowire or nanoparticles requires multi-step wet chemistry reaction and following heat treatment.[125] The carbonaceous current collectors, although having excellent performance, do not have high enough mechanical strength to be used as the current collectors for roll-to-roll processing, and it is difficult to bind the carbon films tightly onto any metal foils. Therefore, our strategy of utilizing electrodeposition demonstrate practical advantage over most of the reported work. Furthermore, the morphology could be further improved through controlling deposition current density, time, and co-deposition of other elements, all of which are worthy to explore as next step.

Lithium metal is a promising anode for high-energy-density batteries owing to its large theoretical capacity and highly negative electrochemical potential. However, its commercial application is stalled by the undesired dendritic growth of lithium during cycling. Among the approaches to address this critical issue, designing a 3-D current collector is a promising strategy, as the increasing nucleation sites introduced by the 3-D structure could effectively reduce local current density, and thus lower the possibility of stimulating dendritic growth.

As discussed in Chapter 1, the major categories of reported 3-D current collectors include copper-based and carbon-based materials. Methods that have been adopted including chemical synthesis, dealloying, laser micro-processing, linear sweep voltammetry, thermal oxidizing etc. Many of which involves long time (longer than 12 hours) and high temperature reaction. Considering the practical manufacturing process and the advantages associated with electrodeposition, as we discussed previously in Chapter 1,

we designed a 3-D Cu-based structure by fabricating favorable morphology that could provide sufficient amount of nucleation sites for Li.

In this work, we discuss a facile one-step electrodeposition process for low-cost, scalable fabrication of copper current collectors with 3-D architected porous structures composed of interconnected nanoparticles of Cu. Li anode deposited into this porous current collector exhibits good cycling stability of >340 hours in symmetric cells without short-circuit. When tested in full cells with liquid or solid-state electrolyte, the Li anode hosted in the 3-D Cu current collector demonstrates excellent cycling performance with no dendrites formation. This process is extremely simple and scalable for mass production of dendrite-free and high capacity current collector for Li-batteries, which can be easily incorporated into the roll-to-roll manufacturing processes of battery industries.

5.2 Methods

5.2.1 Preparation of electrodeposited Cu film.

A typical electrodeposition processing of copper current collector is as follows: A two-electrode system was used and a constant voltage electrodeposition process was controlled with using a battery cycler (Arbin, BT2043). Copper foil with thickness of 0.0005 inch (MTI corp.) and area of about 6.75 cm^2 was used as the working electrode, while a platinum plate with area of 0.25 cm^2 was used as the counter electrode. The electrolyte consists of 0.5 M copper sulfate heptahydrate (VWR International LLC) in 20 mL deionized water. In addition, poly(acrylic acid)-5000 (PAA-5000, 50 wt%, ACROS Organics) and sulfuric acid (95-98%, BDH Chemicals) were used as additives to control the morphology of the deposited Cu surface layer. With using 0.5 mM PAA and 0.1M

sulfate acid as additives, nanometer-sized clusters can be obtained. The current density of working electrode was controlled between 3.5 - 3.7 mA cm^{-2}, to ensure no Cu dendrite is formed.[142] Nanometer sized Cu was electrodeposited on Cu substrate with a constant potential of 2.5 V for 20 min. The reactions at the working electrode and counter electrode are (1) and (2) below, respectively.

$$Cu^{2+} + 2e \rightarrow Cu \qquad\qquad (1)$$

$$2H_2O \rightarrow O_2 + 4e^- + 4H^+ \qquad\qquad (2)$$
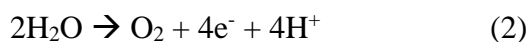
5.2.2   XRD and SEM characterization.

Ex-situ X-ray diffraction (XRD) measurement was performed using a D8 Advance X-ray Diffractometer (Bruker AXS, Germany) equipped with a Molybdenum radiation source (λ Kα_1=0.7093Å) to examine the phase of the deposited copper. Morphology of the surface of the Cu foils before and after electrodeposition processing, and the foils before and after Li plating/stripping were investigated with using a Scanning Electron Microscope (Hitachi SU8010).

5.2.3   Li plating/stripping tests and cycling performance tests in liquid electrolyte.

Standard CR2016-type coin cells were assembled in an Argon (Ar) filled glove box for all liquid-based electrochemical testing, including Li plating/stripping stability tests, Coulombic efficiency tests, electrochemical impedance spectroscopy (EIS), and full-cell cycling tests. For Li plating/stripping and Coulombic efficiency tests, a piece of Li foil with thickness of 0.25 mm was used as the counter electrode, while the electrodeposited Cu foil was used as the working electrode. The electrolyte was 1 M LiTFSI (99.95%,

Sigma-Aldrich) in DOL/DME (1,3-Dioxolane, 99%, Sigma-Aldrich/1,2-Dimethoxyethane, 99.5%, Sigma-Aldrich) in 1:1 volume ratio. No additive was used unless otherwise noted. The Li plating/stripping behavior was tested under current density of 2 and 8 mA cm^{-2} for 1 and 4 mAh cm^{-2} respectively in each cycle with using an Arbin BT2043 battery cycler. Bare Cu foils (b-copper) with no deposition and electrodeposited Cu foils with nanometer-sized structure (n-copper) were tested under the same conditions for comparison. In further electrochemical tests, n-copper was used. Columbic efficiency was calculated based on the ratio of Li stripped to Li plated. One wt% LiNO$_3$ was added into the electrolyte in this test to stabilize the solid-electrolyte-interphase (SEI). The cell was first cycled between 0 and 1 V (versus Li$^+$/Li) at 50 µA for 5 cycles to remove surface contamination and stabilize the SEI. Then, 1 mAh cm^{-2} of Li was plated onto the Cu current collector under a 1 mA cm^{-2} current density, followed with charging to 0.5 V under a current density of 0.5 mA cm^{-2}. EIS measurement was conducted using a Bio-Logic MP3 impedance spectrometer in the frequency range of 100 mHz and 100 kHz. For the full-cell tests, LiFePO$_4$ (MTI Corp.) was blended with carbon black (Super P, MTI Corp.) and Polyvinylidene fluoride (PVDF) (Sigma-Aldrich) with a weight ratio of 8:1:1 as the cathode. The cathode film was made using a typical doctor-blade method, with using N-Methyl-2-pyrrolidone (NMP) (J.T. Baker) as the solvent and applying the slurry onto an aluminum foil with an areal capacity of ~0.73 mAh cm^{-2}. 2 mAh cm^{-2} Li was electrochemically deposited onto n-copper to be used as the anode. The full cell was assembled and tested under the rate of 1C between 2 and 4.2 V. One wt% LiNO$_3$ was added into the electrolyte. All the reaction and measurement were conducted under room temperature.

5.2.4 Preparation of solid-state symmetric cells.

The solid-state symmetric cells were fabricated as follows: the n/b-copper was used as the working electrode, as-synthesized Li_6PS_5Cl was used as the solid electrolyte, and Li foil was used as counter and reference electrode. The three components were added in order into a polycarbonate tube (12.7 mm inner diameter) and pressed together under a pressure of 50 bar. Finally, the tri-layer assembly was sandwiched between two stainless steel rods which were used as current collectors. The solid state symmetric cells were tested under the same electrochemical parameters as the symmetric coin cells.

5.2.5 Preparation of solid-state full cells.

The solid-state Li@Cu/ Li_6PS_5Cl /TiS_2 full cells were fabricated as follows: a composite of TiS_2 and Li_6PS_5Cl (9 mg, TiS_2: Li_6PS_5Cl =1:2 in weight) was used as the cathode, with Li_6PS_5Cl (150 mg) as the solid electrolyte, and pre-lithiated Li@Cu as the anode. The anode was pre-lithiated by plating 2 mAh cm^{-2} of Li onto the n-copper foil in a symmetric coin cell and disassembled in the glove box. The tri-layer full cell was set in a polycarbonate tube (1.27 mm in diameter) and pressed together under 50 bars and then sandwiched between two stainless steel current collectors.

5.3   Results and Discussion

5.3.1 Processing and characterization of electrodeposited Cu current collector.

To create more nucleation/deposition sites on the surface of the current collector, an electrodeposition process was used to control nanometer-sized structure of Cu on the surface of a conventional copper current collector foil in a 0.5 M copper sulfate

heptahydrate solution with PAA-5000 and sulfuric acid as additives. Figure 29a shows the XRD patterns of the bare and deposited samples and it can be clearly seen that only metallic Cu phase is formed in both electrodeposited films. The insets in Figure 29a show the photographs of these samples. The nanometer-structured Cu foil sample (hereby denoted as n-copper) shows a dark color, likely due to strong absorption of visible light by the nano-porous film on the surface, unlike the bare copper foil (hereby denoted as b-copper). Figure 29b and 29c show the SEM images of b-copper and n-copper respectively. The n-copper film has a porous 3-D nanostructure consisting of interconnecting primary particles of ~50 nm and the porosity was estimated to be ~76% (see Table 8 for parameters). The calculation of porosity and maximum capacity is as follows:

1) Measure the thickness (L_{total}) of total film (Cu substrate and deposited film) using a micrometer caliper by taking average of multiple positions.

2) Calculate the thickness of electrodeposited Cu film, $L_{film} = L_{total} - L_{Cu}$. L_{Cu} was measured to be 12.7 μm.

3) Measure the area (S) of the electrodeposited film.

4) Calculate the total volume (V_{total}) of electrodeposited film.

5) Use charge capacity (C) of Cu from electrodeposition to calculate the molar amount of deposited Cu ($M=0.5*C*3600/96360$) and the volume of Cu ($V_{Cu}=63.546*M/8.9$) accordingly.

6) Calculate porous volume, $V_{porous} = V_{total} - V_{Cu}$; calculate porosity $= V_{porous}/V_{total}$

7) Calculate maximum capacity by assuming all the porous can be utilized to accommodate Li during plating. $C_{max} = [(Surface\ area) / (Electrodeposited\ area$

71

S)]* V_{porous}* specific capacity density of Li (2062 mAh cm^{-3}) / surface area (0.7 cm^2).

Careful analysis of the microstructures indicates that the size of the primary particles, the porosity, and the surface morphology of the porous Cu films can be tuned in a wide range by the type and amount of additives used, which form intermediate complex at the copper substrate and function as seeds to form nanoclusters.[143] The optimal condition of electrodeposition, including the concentration of additives and the deposition time, was determined by a series of tests. Both homogeneity and porosity of the deposited layer are critical for the subsequent electrochemical tests. We expect that the nanometer-sized primary particles in the n-copper sample can serve as the deposition/nucleation sites for Li plating and the high porosity of the deposited layer may allow more Li storage inside the porous Cu layer, in addition to the Li plated on the top of the Cu layer. It is worth noting that the deposited layers in n-copper are very robust and adhere well to the Cu substrate, implying a good electrical connectivity and good mechanical integrity. The deposited n-copper layer is typically of ~5 μm thick and the copper foil is as flexible as previous and can be directly used as in roll-to-roll processes.
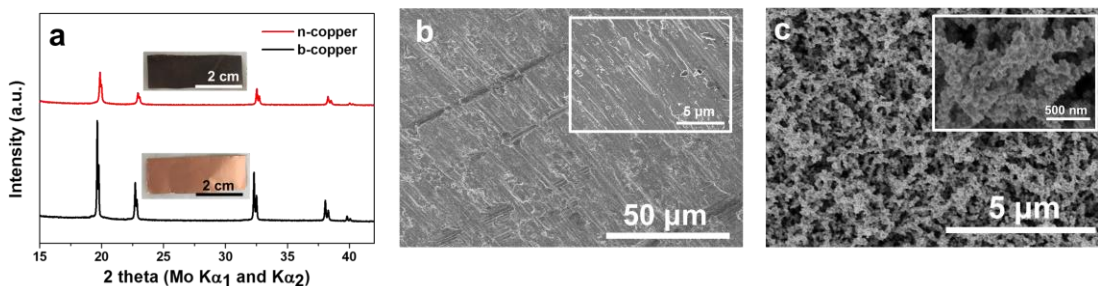
Figure 29 (a) XRD patterns of bare Cu (b-copper) and electrodeposited nanometer-sized Cu (n-copper). Insets are the corresponding photographs of b-copper, and n-copper; (b) SEM image of b-copper with a scale bar of 50 μm. Inset is the zoom-in view with a scale bar of 5 μm; (c) SEM image of n-copper Cu with a scale bar of 5 μm. Inset is the zoom-in view with a scale bar of 500 nm.

Table 8 Parameters of n-copper

Cu film thickness L_{film} (μm)	5.2
Electrodeposited area S (cm^{-2})	6.75
Total volume V_{total} (cm^{-3})	0.00351
Charge capacity of Cu C (Ah)	0.006216
Volume of Cu V_{Cu} (cm^{-3})	0.000829
Volume of porous V_{porous} (cm^{-3})	0.002681
Porosity (%)	76.31
Maximum capacity (mAh cm^{-2})	0.82

5.3.2   *Li metal plating/stripping behaviour.*

The performance of the n-copper current collectors in Li plating-stripping cycles in various areal capacities was evaluated in symmetric Li/Li@Cu cells using a Li counter/reference electrode and a Cu working electrode, as reported previously. For all cells, 2 mAh cm^{-2} of Li was first plated onto the electrodeposited Cu current collectors at a constant current density of 2 mA cm^{-2}. Then, the symmetric cells were cycled with various areal capacities of 1 and 4 mAh cm^{-2}, respectively, with both charge and discharge times of each cycle being set to be 0.5 h (i.e., with current density of 2 and 8 mAh cm^{-2},

respectively). The voltage profiles are shown in Figure 30. In the tests of 1 mAh cm^{-2}, shown in Figure 30a, the symmetric cell with b-copper shows spiky voltage oscillations as large as 1 V, implying internal short-circuits, as also reported by others, likely due to the formation of Li dendrites. In contrast, the n-copper cell shows much better cycling stability with reasonably small voltage amplitude and negligible voltage fluctuations up to 340 hours cycling, indicating significantly improved lithium plating/stripping stability. Figure 30b shows the zoom-in voltage profiles of the three cells within 320-340 hours. The voltage amplitude of n-copper is ~ 50 mV, indicating low interfacial resistance and facilitated ionic and electronic conduction, which can be ascribed to the much larger electroactive surface area than those of b-copper and a more uniform SEI. The large active surface area of n-copper foil is ascribed not only to the nanostructured top surface, but also the pores in which electrolyte can easily throughout percolate. The resistance to interfacial ionic transport is drastically reduced. In the tests with larger areal capacities of 4 mAh cm^{-2} (current density 8 mA cm^{-2}), n-copper cells also show excellent stability and far lower resistance than those of the b-copper, as shown in Figure 30c and 30d. In commercial Li-ion batteries with graphite or Si-C anode, typical areal capacity ranges from 1.5 to 3 mAh cm^{-2}. [144,145] The excellent reversibility and stability in a long time for the n-copper samples at high areal capacities of 4 mAh cm^{-2} demonstrates the promise for it to be used in large form cylindrical or pouch cells.
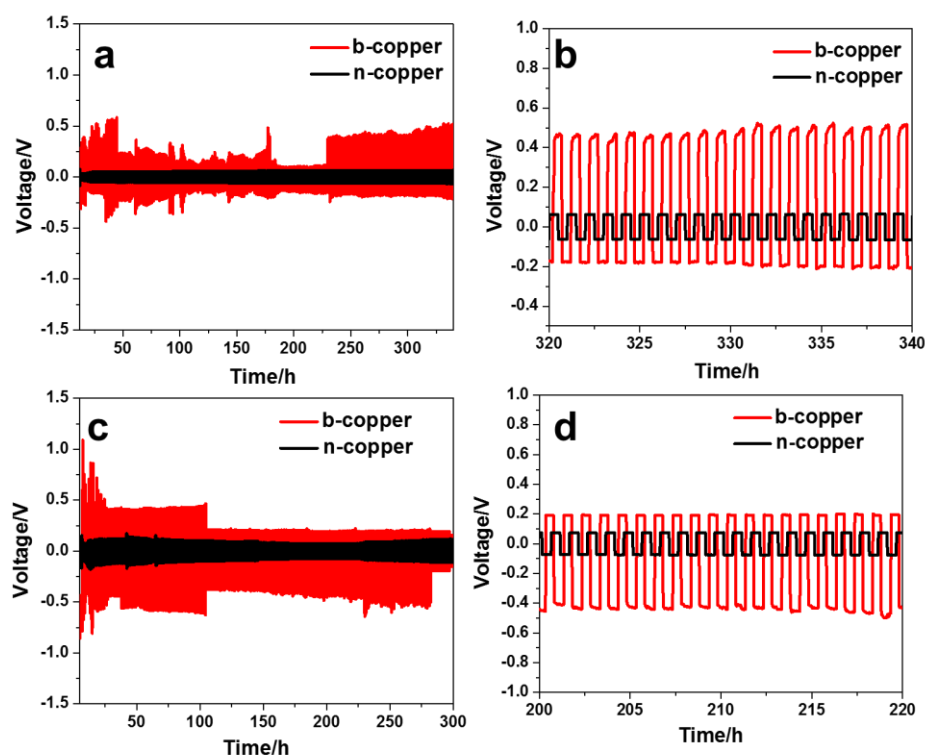
Figure 30 Voltage profiles of Li plating/stripping of the b-copper and n-copper symmetric cells at (a) 1 mAh cm^{-2} and (c) 4 mAh cm^{-2}, respectively. (b) The detailed voltage profiles from 320th-340th cycle in (a). (d) The detailed voltage profiles from 200th-220th cycle in (c).

5.3.3   Morphology evolution of Li deposited on the current collectors.

Careful SEM characterizations were used to understand the excellent cycling performance of the electrodeposited copper current collector and to explore the Li storage mechanism. Figure 31 shows the top view and cross-sectional view of the n-copper foil after Li plating and Li stripping of various capacities, respectively. In Figure 31a, the size of the primary particles obviously increases from ~50 nm in pristine film (Figure 29c) to ~200 nm after 1 mAh cm^{-2} plating, indicating substantial amount of Li is plated onto the surface of Cu particles. Meanwhile, the porosity of the surface layer visually decreased significantly, implying that Li is also deposited into the pores. For comparison, images of

75

b-copper are also provided in Figure 32, from which large amount of Li dendrites formed on top of b-copper can be seen. With increasing amount of Li plated to 2 and 4 mAh cm^{-2}, it can be clearly seen that the size of the primary particles further increases to ~400 nm (2 mAh cm^{-2}), and eventually, ~800 nm (4 mAh cm^{-2}), yet still with a smooth and granular surface, as shown in Figure 31b and 31c. When the capacity increases to 6 mAh cm^{-2}, as shown in Figure 31d, the individual particles are large enough to interconnect and form locally flat surfaces where island-like Li dendrites can grow from, same as what commonly occurs on the surface of Li foil. The suppression of Li dendrite growth is due to the direct deposition only on the highly conductive Cu both on top surface and into the pores, but not on the flat surface of Li.

For Li metal anode, it is confusing to use "theoretical capacity" as the capacity limit, as the maximum amount of Li deposition that would not stimulate dendrites growth oftentimes is not as clear cut. Therefore, we suggest using "practical capacity" to refer to the capacity limit. In this case, the practical areal capacity of n-copper sample processed with current electrodeposition parameters seems to be between 4 and 6 mAh cm^{-2}. This capacity is higher than the maximum amount of Li that can be stored in the pores of the 3-D structure, indicating the structure itself could effectively reduce local current density and accommodate more homogeneous Li deposition on top of the structure. However, this value already exceeds that of commercial graphite anodes and can be further improved with increasing the thickness and porosity and tuning the morphology and composition of the deposition layer.

In the Li stripping tests with capacities of 1, 2, 4, and 6 mAh cm^{-2}, the current densities were set at 2, 4, 8, and 12 mA cm^{-2}, as shown in Figure 31e, f, g, and h,

respectively. It is shown that for the tests of 1, 2, and 4 mAh cm^{-2}, after stripping, the granular morphology of n-copper is retained, yet with decreased porosity and increased size of primary particles, which is mainly due to the remaining SEI covering on the surface of Cu particles. However, after 6 mAh cm^{-2} deposition, as shown in Figure 31h, the stripping of same capacity results in a very different morphology, with irregular matrix of connecting large particles and some voids.

From the cross-sectional view of Li plating/stripping in Figure 31 (i-l), there is a clear trend that with increasing plating capacity, the primary particle size increases throughout the whole thickness of the porous layer yet with little Li dendrite grown on top of the surface, confirming the Li storage in the pores and preferably deposit on Cu nanoparticle sites due to the lower local current density. Compared with bare Cu (Figure 32), the n-copper offers more nucleation sites for Li to avoid dendrite formation. With the proceeding of Li stripping, the pristine porous structure can be largely retained, comparing with cross-sectional view image of pristine n-copper (Figure 33). In both plating and stripping processes, the thickness of the electrodeposited Cu layer does not change significantly, implying the Li deposition pathway is good for maintaining a more homogeneous morphology thus relatively constant volume of the anode during cycling. Figure 31m schematically shows the Li storage mechanism with increasing deposition capacities. The practical capacity limit is that all the pores are filled up and the top surface becomes a flat surface like Li foil, connected by deposited Li and SEI. If more Li is plated, the Li dendrites likely start to growth, as what occurs on pure Li foil.
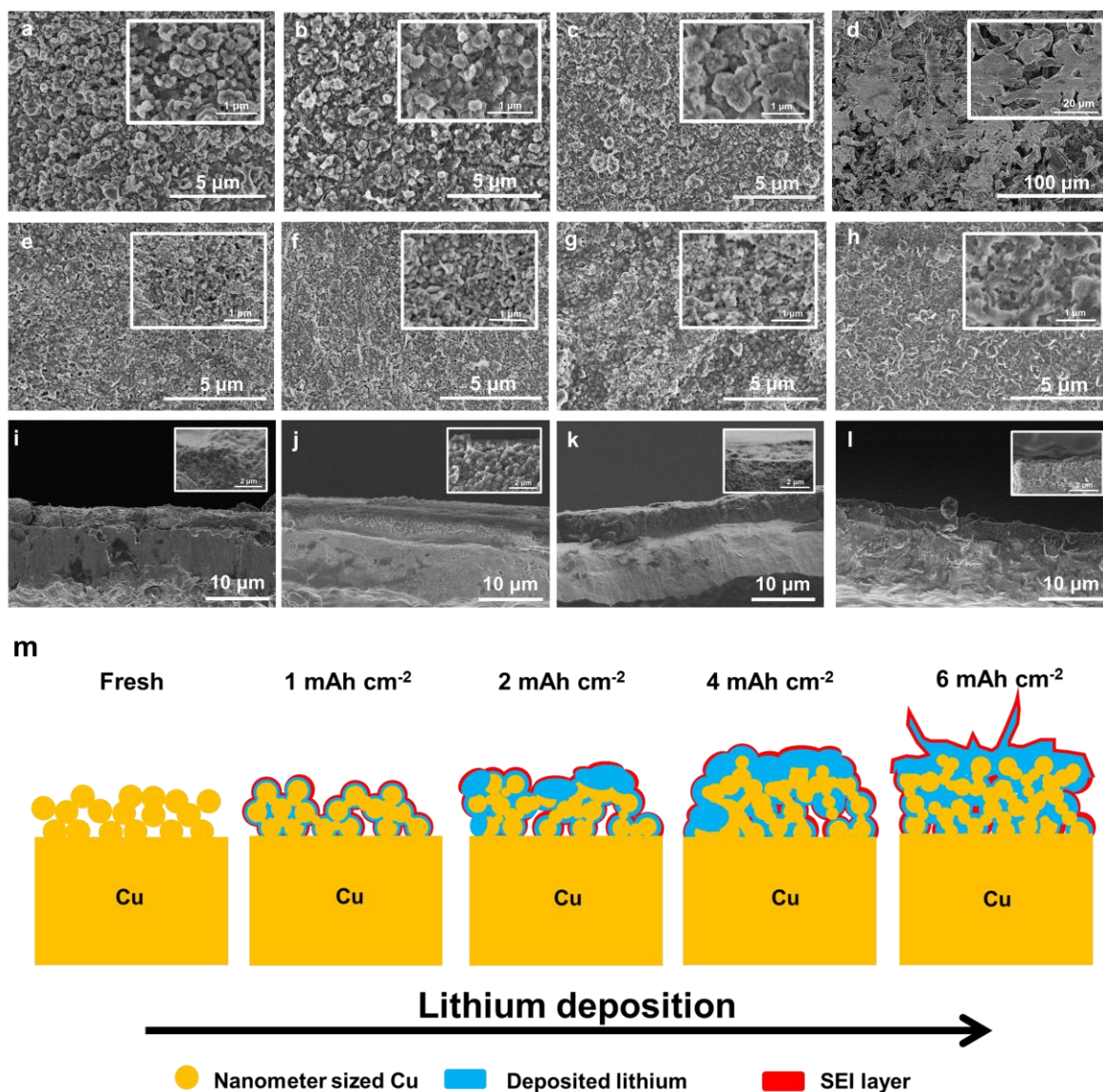
Figure 31 Morphology of deposited Li metal characterized by SEM. Top view images of n-copper electrode after Li plating of (a) 1 mAh cm⁻², (b) 2 mAh cm⁻², (c) 4 mAh cm⁻², and (d) 6 mAh cm⁻². Top view images of n-copper electrode after Li stripping of (e) 1 mAh cm⁻², (f) 2 mAh cm⁻², (g) 4 mAh cm⁻², and (h) 6 mAh cm⁻². Scale bars are 5 μm. Insets are the zoom-in view with scale bars of 1 μm; Cross-sectional SEM images of n-copper electrode after (i) 1 mAh cm⁻² and (j) 4 mAh cm⁻² of Li plating. Scale bars are 10 μm. Insets are the zoom-in views with scale bars of 2 μm; Cross-sectional SEM images of n-copper after Li stripping of (k) 1 mAh cm⁻² and (l) 4 mAh cm⁻². Scale bars are 10 μm. Insets are the zoom-in views with scale bars of 2 μm. The yellow dotted lines denote the boundaries between n-copper (top)

78

and Cu substrate (bottom); (m) Schematic illustration of n-copper current collector deposited with various amount of Li.
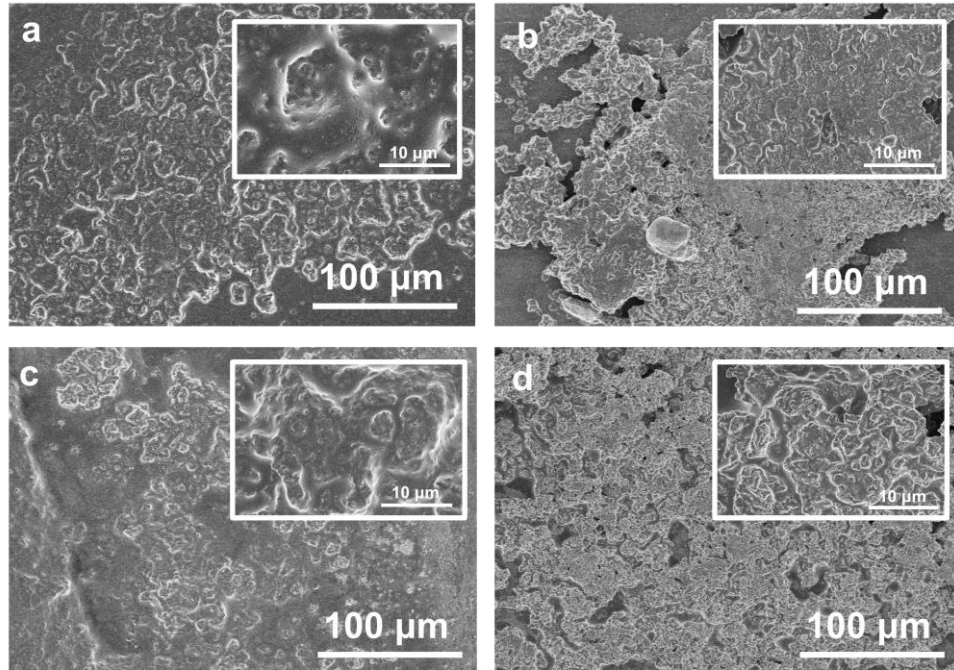
Figure 32 SEM images of b-copper after Li plating for 1 mAh cm-2 (a), 2 mAh cm-2 (b); and stripping of 1 mAh cm-2 (c), 2 mAh cm-2 (d). Scale bars are 100 μm. Insets are the zoom-in view with scale bars of 10 μm.
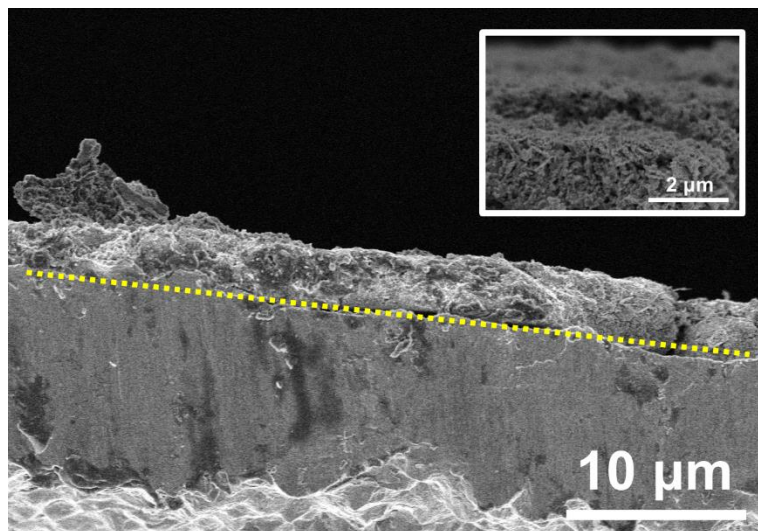
Figure 33 Cross-sectional view of fresh n-copper sample with a scale bar of 10 µm. The inset is the zoom-in view with a scale bar of 2 µm. The yellow dotted lines denote the boundaries between n-copper (top) and Cu substrate (bottom).

5.3.4   Electrochemical characterization and testing.

Electrochemical cycling tests on symmetric cells with constant-current plating (cut with designed capacities) and constant-current stripping (cut with 0.5 V voltage limit) were done and the results are shown in Figure 34. From Figure 34a to Figure 34c, the areal capacity for each Li plating step was fixed at 1 mAh cm^{-2} while the charge step was set to 0.5 V under 0.5 mA cm^{-2}. The voltage plateau of Li plating and stripping of b-copper exhibits a larger voltage hysteresis which can be attributed to the unstable Li/electrolyte interface of bare Cu foil. The smaller voltage hysteresis and higher amount of Li stripped (i.e. highest Coulombic efficiency) is demonstrated by n-copper current collector in Figure 34b. This is due to the low interfacial resistance resulted from the stable Li/electrolyte interface formed in n-copper current collector. The cycling Coulombic efficiencies (CE) of the two types of current collectors were further examined in extended cycles. CE was calculated as the ratio of the amount of Li stripped versus plated in each cycle. The results

are shown in Figure 34c. The CE of b-copper is 60% after 80 cycles, with significant fluctuations. The CE of n-copper is 95% after 80 cycles.

To evaluate the feasibility of using this electrodeposited Cu in practical battery systems, full-cell tests were performed. Both n-copper and b-copper were first pre-lithiated in a symmetric cell with 2 mAh cm^{-2} of Li. Then the symmetric cell was taken apart and the obtained lithiated n-copper was used as the anode coupled with a LiFePO$_4$ cathode. Figure 35a shows the voltage-capacity profiles of the cells with b-copper and n-copper anodes at 0.1 C (1C=170 mA g^{-1}) in a voltage window of 2.0 to 4.2 V. The cell with n-copper anode delivers an initial discharge capacity of 154.6 mAh g^{-1}, slightly higher than 149.5 mAh g^{-1} for the b-copper cell. Figure 35b presents the charge/discharge curves of the cell with n-copper substrate in the 1st, 2nd, and 10th charge/discharge cycles at 0.1 C, showing good consistency of the voltage profile. In the higher rate cycling tests at 1 C (Figure 35c), the cell with b-copper anode presents a capacity decay from 132.6 to 92.6 mAh g^{-1} in 100 cycles with a capacity retention of 69.8 %. In comparison, the cell with n-copper anode exhibits excellent cycling performance. It delivers a capacity of 127.6 mAh g^{-1} after 100 cycles and with a capacity retention of 95 %. The Coulombic efficiency of the cell with electrodeposited n-copper anode is ~99.66 % at 1 C upon 100 cycles, which is much better than that with b-copper substrate and is comparable to high performance carbonaceous-based current collector material. The electrochemical performance of n-copper used in the LiFePO$_4$ full cell shows its potential in practical application.
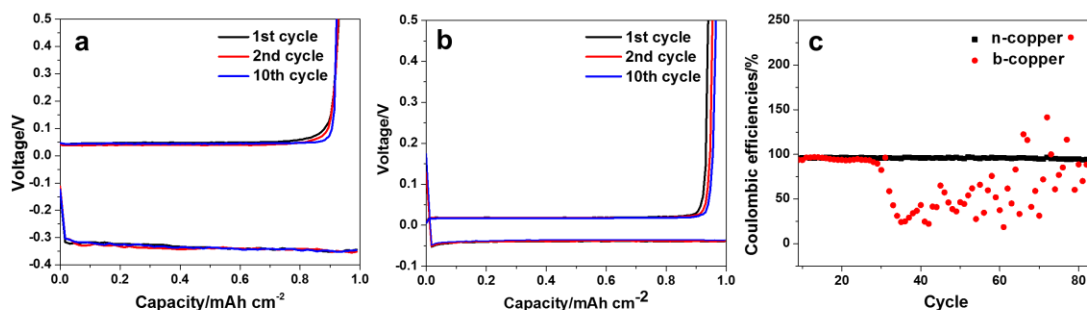
Figure 34 Voltage profiles of Li plating/stripping on planar Cu (a), the electrodeposited n-copper (b), and the CE for the samples (c).
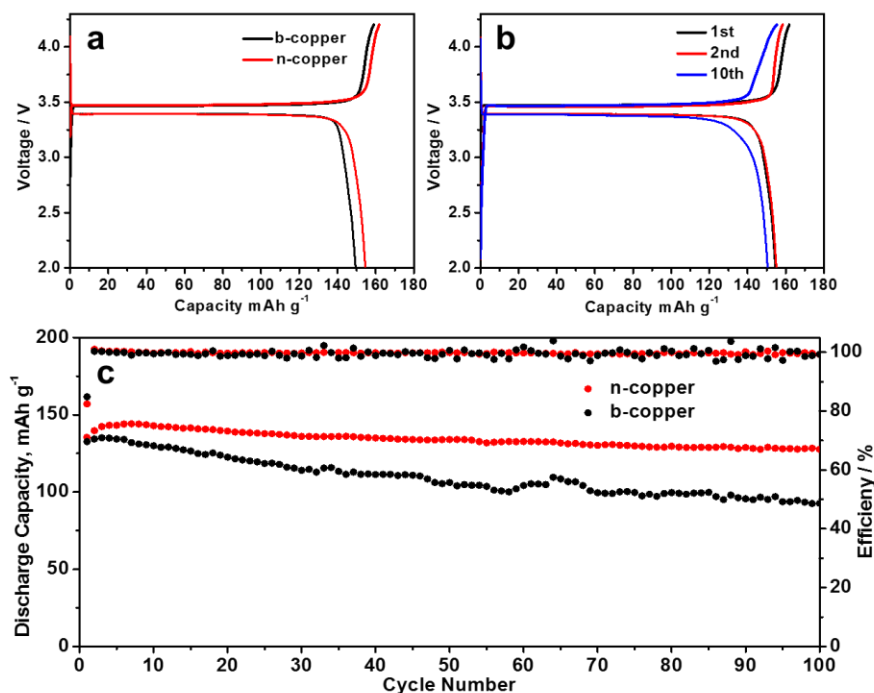
Figure 35 (a) Charge/discharge profiles of the full cells with Li@b-copper and Li@n-copper, respectively. (b) Charge/discharge profiles at 1st, 2nd, and 10th cycle of the full cell with Li@n-copper electrode. (c) Cycling performance and CE of full cells with Li@b-copper and Li@n-copper at 1 C.

To explore the possibility of using this novel 3-D nanostructured current collector in all-solid-state batteries, which is another promising technology that requires usage of Li-metal anodes, tests were conducted in both symmetric and full cells. The symmetric cells (Li/Li@Cu) used Li_6PS_5Cl as electrolyte, Li foil as counter electrode, and b-copper or n-copper as working electrode. As shown in Figure 36a, cell with b-copper shows larger voltage fluctuations, while for the cell with n-copper, excellent cycling stability as well as much smaller voltage hysteresis is observed and the performance stays unchanged for more than 500 hours (Figure 36b), indicating good interface compatibility and stable plating/stripping at the solid-solid interface as well. Cycling tests at various current densities were also conducted to evaluate the rate performance. It is obvious that cell with n-copper current collector exhibits smaller voltage fluctuations than that of b-copper upon different areal densities (Figure 36c). An all-solid-state full cell was also assembled with using pre-lithiated n-copper as anode and TiS_2 as cathode to explore the potential of applications in all-solid-state batteries. As shown in Figure 37, the solid-state full cell shows the typical charge and discharge curve of TiS_2, which is in consistent with previous reports.[146] As shown in Figure 36d, solid-state cell with n-copper can deliver an initial reversible capacity of 179 mAh g^{-1} at 0.2 C (1C = 239 mA g^{-1}) at 20 °C. After 20 cycles, it can still maintain a reversible capacity of 156.5 mAh g^{-1} with a CE of 99.3%, corresponding to the capacity retention of 87.5 %. This result demonstrates the possible practical application of the electrodeposited n-copper current collector in all-solid-state battery systems.
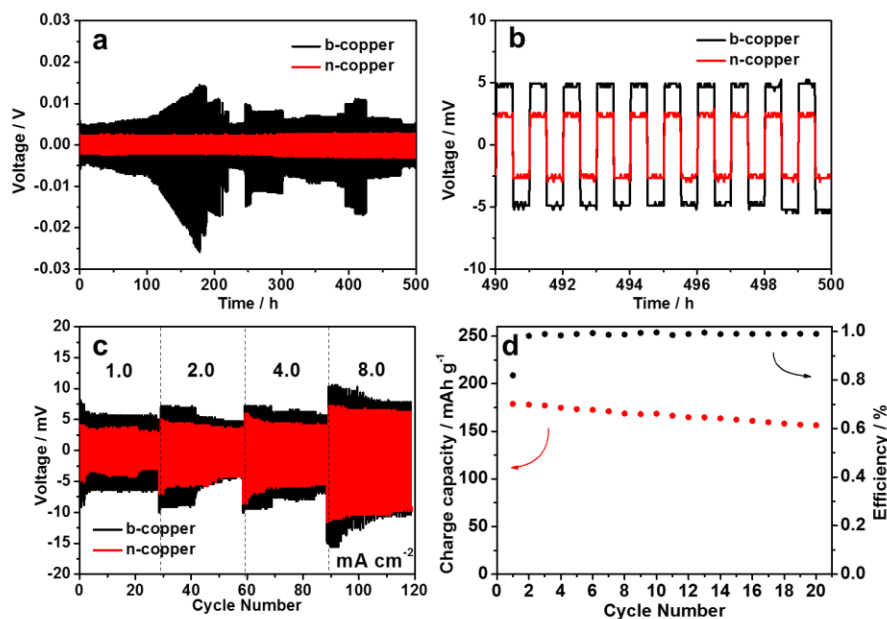
Figure 36 (a) Voltage profiles of Li plating/stripping of the solid state symmetric cells (n-copper and b-copper at 1 mAh cm^{-2}, respectively); (b) The detailed voltage profiles from 490th-500th cycle in (a); (c) Rate performance of Li plating/stripping of the solid-state symmetric cells (n-copper and b-copper at various current densities); (d) Cycling performance of the solid-state Li@n-copper/TiS$_2$ full cells at 0.2C.
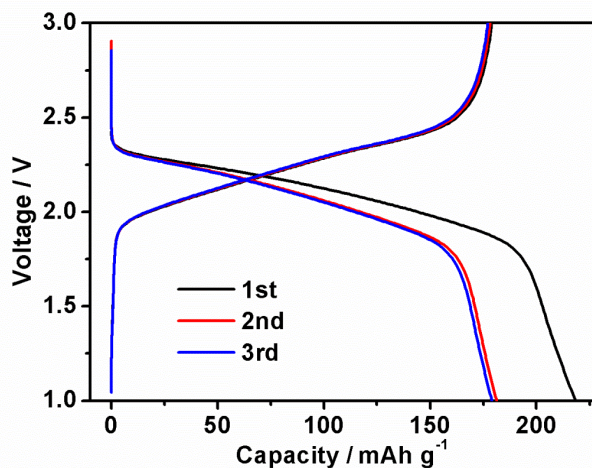
Figure 37 Charge-discharge curves (first 3 cycles) of the Cu@Li/TiS2 all-solid-state cell using Li6PS5Cl as electrolyte.

84

5.4   Conclusion

In conclusion, we have demonstrated the capability of electrodeposited Cu 3-D nanostructures of accommodating Li within its porous structure, which effectively suppresses Li dendrite formation and provides a very high practical Li storage areal capacity of >4 mAh cm^{-2}. The full-cell tests with using both liquid electrolyte and solid electrolyte show exciting high performances. Most importantly, this facile one-step electrodeposition method is very scalable for mass production. One easy configuration to realize it in industrial scale is schematically shown in Figure 38. The 3-D structure of Cu can be simultaneously deposited on both sides of standard Cu foils for bi-polar designs. As the deposited Cu layer is robust and has much better mechanical strength than graphite anode, the thickness of Cu foil substrate can be further reduced from currently used, which can further increase the energy density of the cell. In addition, this current collector can be used in not only Li-ion, but also in Li-S and Li-O$_2$ batteries, provided cathode problems solved. The electrodeposition method also provides a lot of flexibility and tunability of the deposited structure, which suggests more Li may be accommodated and ultrahigh energy density batteries may be developed along this promising approach.
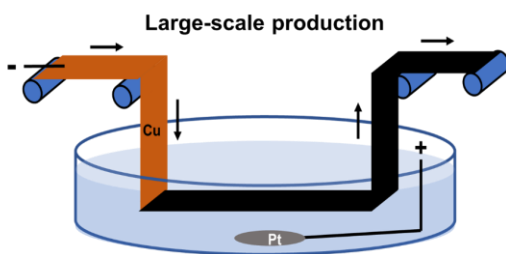
Figure 38 A schematic picture of scale-up production of electrodeposited Cu foils as current collectors of Li-metal batteries.

CHAPTER 6.   CONCLUSION AND FUTURE PERSPECTIVES

6.1   Conclusion

In this thesis, we study the formation of nanometric polymorphs of metal and alloy with using advanced *in situ* structure characterization techniques. To begin with, Co was used as a model system to build a generalized theorem of understanding phase formation. It was found that, in the solvothermal reaction, the surface energy was largely affected by the adsorbents, namely OH^-, from the solution. In competing with the bulk energy of particles, the surface energy plays an important role in determining the overall energy of the polymorphs for nanometric Co particles, resulting in the formation of various phases under different pH levels. The *in situ* solvothermal platform we built at two national laboratories leveraged the advantage of synchrotron x-ray and enable real-time observation from nucleation upon phase ripening. This work could not only serve as a reference for selective synthesis of various polymorphs of nanoscale Co for specific applications, but also may be extended to other functional materials besides simple elemental materials, such alloys, oxides, or carbonates.

The second part of this thesis explores factors impacting phase formation with another important synthesis approach – electrodeposition. Electrodeposition plays an important role in synthesizing functional nanometric materials for its tunable and facile features. It was found that aside from pH of the solution, which would change the surface energy of newly formed nuclei, over-potential is another factor affecting phase selection by boosting the kinetics of the polymorph formation, resulting in co-deposition of both stable and meta-stable polymorphs. In addition, based on the theorem, we successfully

demonstrated the feasibility of obtaining layer-by-layer Co structure with desired phase by choosing appropriate synthesis conditions. The *in situ* electrodeposition platform we built enable the observation for the ultra-fast reaction with high quality signal for the first time, and would pave the way for studying phase formation of multi elements through electrodeposition.

In the third part of the thesis, we moved towards two elements system by starting with Co and Ni. By introducing another element, there are three key factors that would affect phase formation. Internally, the initial starting ratio of Co and Ni would affect the bulk energy of obtained phase, results in obtaining solid solution that are in accordance with bulk phase diagram. Externally, the pH of the solution and over-potential would tune phase formation as well. By reducing pH of the solution, the metastable *fcc* phase of CoNi at stable *hcp* dominant phase diagram region would form, mainly due to the contribution of surface energy. By increasing over-potential, the metastable phase could be concurrently obtained by expediated kinetics, and the effect is more severe as the composition moves more towards mixture region. This part of the work demonstrates the universal applicability of *in situ* electrodeposition approach we developed, and demonstrate the more complicated factors of tuning polymorphs for multi-elements system.

In the last part, we switched gear and explored another aspect associated with electrodeposition – morphology tuning and its application in energy storage area. Based on the observation from Co electrodeposition that simply adding additives, the morphology of as-synthesized particle could drastically change, we developed a one-step electrodeposition method to obtain a 3-D Cu current collector to be used in lithium metal batteries. We have demonstrated the capability of electrodeposited Cu 3-D nanostructures of accommodating

Li within its porous structure, which effectively suppresses Li dendrite formation and provides a very high practical Li storage areal capacity of >4 mAh cm^{-2}. The full-cell tests with using both liquid electrolyte and solid electrolyte show exciting high performances. Most importantly, this facile one-step electrodeposition method is very scalable for mass production.

6.2   Future perspectives

The work in this thesis propose a generalized theorem to guide synthesis of nanometric materials. Various potential future work could stem from this research. First, Co-based alloys (e.g., Fe, Zn, Cu etc.) have importance in various industries and their properties is closely related with the alloyed phase. By implementing the approach we proposed in this work, it would be interesting to study other Co-based system and investigate how to tune their nanometric phase selectively through electrodeposition. The principles would guide selective synthesis of desired phase under nanometer scale. Ultimately, up to 5 elements system could have interesting magnetic, electrical, or mechanical properties, as high-entropy-alloy has growing interests among scientific community. Second, the morphology tuning for 3-D Cu current collectors could still be improved. The current structure has a theoretic capacity of 0.82 mAh/cm^2, which still has room to improve. Increasing porosity by either adding other additives or tuning deposition condition (current density or time) would be a possible way to get a structure with more nucleation sites for Cu to suppress Li dendrites. In addition, by incorporating another element, e.g., Ni, to get an alloyed 3-D current collector, would help improve conductivity and tune the morphology, which would benefit battery cycling.

REFERENCES

(1) Issa, B.; Obaidat, I. M.; Albiss, B. A.; Haik, Y. Magnetic Nanoparticles : Surface Effects and Properties Related to Biomedicine Applications. *Int. J. Mol. Sci.* **2013**, *14*, 21266–21305.

(2) Castleman, A. W.; Park, U. V; Pennsyl, V.; Bowen, K. H. Clusters : Structure , Energetics , and Dynamics of Intermediate States of Matter. *J. Phys. Chem.* **1996**, *3654* (96), 12911–12944.

(3) Malik, R.; Burch, D.; Bazant, M.; Ceder, G. Particle Size Dependence of the Ionic Diffusivity. *Nano Lett.* **2010**, *10*, 4123–4127.

(4) Khlebtsov, N. G.; Dykman, L. A. Optical Properties and Biomedical Applications of Plasmonic Nanoparticles. *J. Quant. Spectrosc. Radiat. Transf.* **2010**, *111* (1), 1–35.

(5) Leslie-Pelecky, D. L.; Rieke, R. D. Magnetic Properties of Nanostructured Materials. *Chem. Mater.* **1996**, *8* (8), 1770–1783.

(6) Levchenko, A. A.; Li, G.; Boerio-goates, J.; Woodfield, B. F.; Navrotsky, A. TiO2 Stability Landscape : Polymorphism , Surface Energy , and Bound Water Energetics. *Chem Mater* **2006**, *84* (4), 6324–6332.

(7) Sun, W.; Jayaraman, S.; Sun, W.; Jayaraman, S.; Chen, W.; Persson, K. A.; Ceder, G. Nucleation of Metastable Aragonite CaCO3 in Seawater. *PNAS* **2015**, *112* (11), 3199–3204.

(8) Chen, B.; Sun, W.; Kitchaev, D. A.; Ginley, D. S.; Gorman, B. P.; Stone, K. H.; Schelhas, L. T.; Mangum, J. S.; Thampy, V.; Garten, L. M.; et al. Understanding Crystallization Pathways Leading to Manganese Oxide Polymorph Formation. *Nat. Commun.* **2018**, *9* (1), 2553.

(9) Chan, E. M.; Mathies, R. A.; Alivisatos, A. P.; Di, V.; Berkeley, L. Size-Controlled Growth of CdSe Nanocrystals in Microfluidic Reactors. *Nano Lett.* **2003**, *3* (2), 1–3.

(10) Sun, S.; Zeng, H. Size-Controlled Synthesis of Magnetite Nanoparticles. *JACS Commun.* **2002**, *124* (28), 8204–8205.

(11) Wiley, B.; Sun, Y. Synthesis of Silver Nanostructures with Controlled Shapes and Properties. *Acc. Chem. Res.* **2007**, *40* (10), 1067–1076.

(12) Peng, X.; Manna, L.; Yang, W.; Wickham, J.; Scher, E.; Kadavanich, A.; Alivisatos, A. P. Shape Control of CdSe Nanocrystals. *Nature* **2000**, *404* (6773), 59–61.

(13) Chen, H.; Wu, L.; Zhang, L.; Zhu, Y.; Grey, C. P. LiCoO2 Concaved Cuboctahedrons from Symmetry-Controlled. *J. Am. Chem. Soc.* **2011**, *133* (2), 262–270.

(14) Lu, Z.; Chen, H.; Robert, R.; Zhu, B. Y. X.; Deng, J.; Wu, L.; Chung, C. Y.; Grey, C. P. Citric Acid- and Ammonium-Mediated Morphological Transformations of Olivine LiFePO 4 Particles. *Chem. Mater.* **2011**, *23* (11), 2848–2859.

(15) Han, X.; Jin, M.; Xie, S.; Kuang, Q.; Jiang, Z.; Jiang, Y.; Xie, Z.; Zheng, L. Synthesis of Tin Dioxide Octahedral Nanoparticles with Exposed High-Energy {221} Facets and Enhanced Gas-Sensing Properties. *Angew. Chemie - Int. Ed.* **2009**, *48* (48), 9180–9183.

(16) Chen, B. H.; Grey, C. P. Molten Salt Synthesis and High Rate Performance of the "Desert-Rose" Form of LiCoO2. *Adv. Mater.* **2008**, *2* (110), 2206–2210.

(17) Burda, C.; Chen, X.; Narayanan, R.; El-Sayed, M. A. *Chemistry and Properties of Nanocrystals of Different Shapes*; 2005; Vol. 105.

(18) Bilecka, I.; Elser, P.; Niederberger, M. Kinetic and Thermodynamic Aspects in the Microwave-Assisted Synthesis of ZnO Nanoparticles in Benzyl Alcohol. *ACS Nano* **2009**, *3* (2), 467–477.

(19) Tao, A. R.; Habas, S.; Yang, P. Shape Control of Colloidal Metal Nanocrystals. *Small* **2008**, *4* (3), 310–325.

(20) Finnegan, M. P.; Zhang, H.; Banfield, J. F. Phase Stability and Transformation in Titania Nanoparticles in Aqueous Solutions Dominated by Surface Energy. *J. Phys. Chem. C* **2007**, *111* (5), 1962–1968.

(21) Seriani, N. Abinitio Thermodynamics of Lithium Oxides: From Bulk Phases to Nanoparticles. *Nanotechnology* **2009**, *20* (44).

(22) Li, R.; Zhang, X.; Dong, H.; Li, Q.; Shuai, Z.; Hu, W. Gibbs-Curie-Wulff Theorem in Organic Materials: A Case Study on the Relationship between Surface Energy and Crystal Growth. *Adv. Mater.* **2016**, *28* (8), 1697–1702.

(23) Choon, H. B. N.; Wai, Y. F. Shape Evolution of Cu2O Nanostructures via Kinetic and Thermodynamic Controlled Growth. *J. Phys. Chem. B* **2006**, *110* (42), 20801–20807.

(24) Sun, Y.; Xia, Y. Shape-Controlled Synthesis of Gold and Silver Nanoparticles. *Source Sci. New Ser.* **2002**, *298* (5601), 2176–2179.

(25) Zeng, J.; Zheng, Y.; Rycenga, M.; Tao, J.; Li, Z. Y.; Zhang, Q.; Zhu, Y.; Xia, Y. Controlling the Shapes of Silver Nanocrystals with Different Capping Agents. *J. Am. Chem. Soc.* **2010**, *132* (25), 8552–8553.

(26)   Murphy, C. Nanocubes and Nanoboxes. *Science.* **2002**, *298*, 64–65.

(27)   Patel, A. A.; Wu, F.; Zhang, J. Z.; Torres-Martinez, C. L.; Mehra, R. K.; Yang, Y.; Risbud, S. H. Synthesis, Optical Spectroscopy and Ultrafast Electron Dynamics of PbS Nanoparticles with Different Surface Capping. *J. Phys. Chem. B* **2000**, *104* (49), 11598–11605.

(28)   Kitchaev, D. A.; Ceder, G. Evaluating Structure Selection in the Hydrothermal Growth of FeS2 Pyrite and Marcasite. *Nat. Commun.* **2016**, *7*, 1–7.

(29)   Kitchaev, D. A.; Dacek, S. T.; Sun, W.; Ceder, G. Thermodynamics of Phase Selection in MnO 2 Framework Structures through Alkali Intercalation and Hydration. *J. Am. Chem. Soc.* **2017**, *139* (7), 2672–2681.

(30)   Hu, X.; Kitchaev, D. A.; Wu, L.; Zhang, B.; Meng, Q.; Poyraz, A. S.; Marschilok, A. C.; Takeuchi, E. S.; Takeuchi, K. J.; Ceder, G.; et al. Revealing and Rationalizing the Rich Polytypism of Todorokite MnO 2. *J. Am. Chem. Soc.* **2018**, *140*, 6961–6968.

(31)   Levchenko, A. A.; Li, G.; Boerio-Goates, J.; Woodfield, B. F.; Navrotsky, A. TiO2 Stability Landscape: Polymorphism, Surface Energy, and Bound Water Energetics. *Chem. Mater.* **2006**, *18* (26), 6324–6332.

(32)   Erbudak, M.; Wetli, E.; Hochstrasser, M.; Pescia, D.; Vvedensky, D. D. Surface Phase Transitions during Martensitic Transformations of Single-Crystal Co. *Phys. Rev. Lett.* **1997**, *79* (10), 1893–1896.

(33)   Lu, A. H.; Salabas, E. L.; Schüth, F. Magnetic Nanoparticles: Synthesis, Protection, Functionalization, and Application. *Angew. Chemie - Int. Ed.* **2007**, *46* (8), 1222–1244.

(34)   Song, Y.; Modrow, H.; Henry, L. L.; Saw, C. K.; Doomes, E. E.; Palshin, V.; Hormes, J.; Kumar, C. S. S. R.; Bonn, D.-; V, S. U.; et al. Microfluidic Synthesis of Cobalt Nanoparticles. *Chem Mater* **2006**, *127* (47), 2817–2827.

(35)   Grass, R. N.; Stark, W. J. Gas Phase Synthesis of Fcc-Cobalt Nanoparticles. *J. Mater. Chem.* **2006**, *16*, 1825–1830.

(36)   Diana, S.; Lee, S.; Petroff, P. M.; Kramer, E. J. Fabrication of Hcp-Co Nanocrystals via Rapid Pyrolysis in Inverse PS- B -PVP Micelles and Thermal Annealing. *Nano Lett.* **2003**, *3* (7), 891–895.

(37)   Puntes, V. F.; Zanchet, D.; Erdonmez, C. K.; Alivisatos, A. P. Synthesis of Hcp-Co Nanodisks. *J. Amer. Chem. Soc.* **2002**, No. 11, 12874–12880.

(38)   Guo, F.; Zheng, H.; Yang, Z.; Qian, Y. Synthesis of Cobalt Nanoparticles in Ethanol Hydrazine Alkaline System (EHAS) at Room Temperature. *Mater. Lett.* **2002**, *56* (6), 906–909.

(39) Vaný́sek, P. *Handbook of Chemistry and Physics: 93rd Edition.*; Chemical Rubber Company, 2012.

(40) Slater, J. C. Atomic Radii in Crystals. *J. Chem. Phys.* **2010**, *41* (10), 3199–3204.

(41) Predel, B. Co-Ni (Cobalt-Nickel). In *Ca-Cd–Co-Zr*; Springer, Berlin, Heidelberg, 2012; pp 1–5.

(42) Feng, G.; Kuang, Y.; Li, P. S.; Han, N. N.; Sun, M.; Zhang, G. X.; Sun, X. M. Single Crystalline Ultrathin Nickel-Cobalt Alloy Nanosheets Array for Direct Hydrazine Fuel Cells. *Adv. Sci.* **2017**, *4* (3), 1–6.

(43) Ganesan, P.; Sivanantham, A.; Shanmugam, S. Nanostructured Nickel-Cobalt-Titanium Alloy Grown on Titanium Substrate as Efficient Electrocatalyst for Alkaline Water Electrolysis. *ACS Appl. Mater. Interfaces* **2017**, *9* (14), 12416–12426.

(44) Willard, M. A.; Kurihara, L. K.; Carpenter, E. E.; Calvin, S.; Harris, V. G. Chemically Prepared Magnetic Nanoparticles. *Int. Mater. Rev.* **2004**, *49* (3–4), 125–170.

(45) Walton, R. I. Subcritical Solvothermal Synthesis of Condensed Inorganic Materials. *Chem. Soc. Rev.* **2002**, *31* (4), 230–238.

(46) Oliveira, M. M.; Schnitzler, D. C.; Zarbin, A. J. G. (Ti , Sn) O 2 Mixed Oxides Nanoparticles Obtained by the Sol - Gel Route. *Chem Mater* **2003**, *15* (9), 1903–1909.

(47) Andersson, M.; Lars, O. Preparation of Nanosize Anatase and Rutile TiO 2 by Hydrothermal Treatment of Microemulsions and Their Activity for Photocatalytic Wet Oxidation of Phenol. *J. Phys. Chem. B* **2002**, *106* (41), 10674–10679.

(48) Fayette, M.; Bertocci, U.; Stafford, G. R. In Situ Stress Measurements during Cobalt Electrodeposition on (111)-Textured Au. *J. Electrochem. Soc.* **2016**, *163* (5), D146–D153.

(49) Lai, J.; Niu, W.; Luque, R.; Xu, G. Solvothermal Synthesis of Metal Nanocrystals and Their Applications. *Nano Today* **2015**, *10* (2), 240–267.

(50) Jian, R. X. Æ.; Shang, K. Morphological Control in Solvothermal Synthesis of Titanium Oxide. *J. Mater. Sci.* **2007**, *42* (16), 6583–6589.

(51) Choucair, M.; Thordarson, P.; Stride, J. A. Gram-Scale Production of Graphene Based on Solvothermal Synthesis and Sonication. *Nat. Nanotechnol.* **2009**, *4* (1), 30.

(52) Hu, G.; Ma, D.; Cheng, M.; Bao, X. Direct Synthesis of Uniform Hollow Carbon Spheres by a Self-Assembly Template Approach. *Chem. Commun.* **2002**, *17*, 1948–1949.

(53)   Schwarzacher, W. Electrodeposition: A Technology for the Future. *Electrochem. Soc. Interface* **2006**, *15* (1), 32–35.

(54)   Valladares, L. D. L. S.; Felix, L. L.; Dominguez, A. B.; Mitrelias, T. Controlled Electroplating and Electromigration in Nickel Electrodes for Nanogap Formation. *Nanotechnology* **2010**, *21* (44), 445304.

(55)   Reference Electrodes https://www.gamry.com/application-notes/electrodes-cells/reference-electrodes/.

(56)   Bard, Allen J.; Faulkner, L. R. *Electrochemical Methods: Fundamentals and Applications (2 Ed.)*; Wiley, 2000.

(57)   League of european accelerator-based photon sources. What is a synchrotron ? https://www.leaps-initiative.eu/synchrotrons/what_is_a_synchrotron/.

(58)   Synchrotron https://en.wikipedia.org/wiki/Synchrotron.

(59)   Joubert, D. From Ultrasoft Pseudopotentials to the Projector Augmented-Wave Method. *Phys. Rev. B - Condens. Matter Mater. Phys.* **1999**, *59* (3), 1758–1775.

(60)   Kresse, G.; Furthmüller, J. Efficient Iterative Schemes for Ab Initio Total-Energy Calculations Using a Plane-Wave Basis Set. *Phys. Rev. B - Condens. Matter Mater. Phys.* **1996**, *54* (16), 11169–11186.

(61)   Perdew, J. P.; Burke, K.; Ernzerhof, M. Generalized Gradient Approximation Made Simple. *Phys. Rev. Lett.* **1996**, *77* (18), 3865–3868.

(62)   Jain, A.; Hautier, G.; Moore, C. J.; Ping Ong, S.; Fischer, C. C.; Mueller, T.; Persson, K. A.; Ceder, G. A High-Throughput Infrastructure for Density Functional Theory Calculations. *Comput. Mater. Sci.* **2011**, *50* (8), 2295–2310.

(63)   Sun, R. Photovoltaic Properties and Size-pH Phase Stability of Iron Disulfide from Density-Functional Theory. *Ph.D. thesis* **2013**.

(64)   Ong, S. P.; Wang, L.; Kang, B.; Ceder, G. Li-Fe-P-O2 Phase Diagram from First Principles Calculations. *Chem Mater* **2008**, *77* (4), 1798–1807.

(65)   Toby, B. H. EXPGUI, a Graphical User Interface for GSAS. *J. Appl. Crystallogr.* **2001**, *34* (2), 210–213.

(66)   Feldmann, B. C. Polyol-Mediated Synthesis of Nanoscale Functional Materials. *Adv. Funct. Mater.* **2003**, *13* (2), 101–107.

(67)   Li, R.; Zhang, X.; Dong, H.; Li, Q.; Shuai, Z.; Hu, W. Gibbs – Curie – Wulff Theorem in Organic Materials : A Case Study on the Relationship between Surface Energy and Crystal Growth. *Adv. Mater.* **2016**, *28*, 1697–1702.

(68)   Hwee, C.; Ng, B.; Fan, W. Y. Shape Evolution of Cu 2 O Nanostructures via Kinetic and Thermodynamic Controlled Growth. *J. Phys. Chem. B* **2006**, *110*, 20801–20807.

(69)   Ingham, B. and Toney, M. F. X-Ray Diffraction for Characterizing Metallic Films 1. *Met. Film. Electron. Opt. Magn. Appl.* **2014**, 3–38.

(70)   Kitakami, O.; Sato, H.; Shimada, Y.; Sato, F.; Tanaka, M. Size Effect on the Crystal Phase of Cobalt Fine Particles Osamu. *Phys. Rev. B* **1997**, *56* (21), 849–854.

(71)   Shinichi, S.; Chem, P.; Phys, C. As Featured in : Negative Electrodes for Na-Ion Batteries. *Phys.Chem.Chem.Phys* **2014**, *16*, 15007.

(72)   Wang, L. P.; Yu, L.; Wang, X.; Xu, Z. J. Recent Developments in Electrode Materials for Sodium-Ion Batteries. *J. Mater. Chem. A* **2015**, *3*, 9353–9378.

(73)   Jin, T.; Yamaguchi, T.; Tanabe, K. Mechanism of Acidity Generation on Sulfur-Promoted Metal Oxides. *J. Phys. Chem.* **1986**, *90* (20), 4794–4796.

(74)   Dharmadasa, I. M.; Haigh, J. Strengths and Advantages of Electrodeposition as a Semiconductor Growth Technique for Applications in Macroelectronic Devices. *J. Electrochem. Soc.* **2006**, *153* (1), G47.

(75)   Chen, Z.; Li, F.; Hao, L.; Chen, A.; Kong, Y. One-Step Electrodeposition Process to Fabricate Cathodic Superhydrophobic Surface. *Appl. Surf. Sci.* **2011**, *258* (4), 1395–1398.

(76)   Cohen-Hyams, T.; Kaplan, W. D.; Yahalom, J. Structure of Electrodeposited Cobalt. *Electrochem. Solid-State Lett.* **2002**, *5* (8), C75.

(77)   Sulcius, A.; Griskonis, E.; Kantminiene, K.; Zmuidzinaviciene, N. Influence of Different Electrolysis Parameters on Electrodeposition of γ- And α-Mn from Pure Electrolytes - A Review with Special Reference to Russian Language Literature. *Hydrometallurgy* **2013**, *137*, 33–37.

(78)   Mattos, O. R.; Barcia, O. E.; Miranda, F. J. F. ZnFe Anomalous Electrodeposition : Stationaries and Local pH Measurements. *Electrochim. Acta* **2002**, *47*, 4091–4100.

(79)   Alarfaj, E.; Subahi, A. The Effect of Solution pH and Applied Magnetic Field on the Electrodeposition of Thin Single-Crystal Films of Cobalt. *Br. J. Appl. Phys.* **1964**, *15* (7), 807.

(80)   Nakahara, S.; Mahajan, S. The Influence of Solution P H on Microstructure of Electrodeposited Cobalt. *J. Electrochem. Soc.* **1980**, *127* (2), 283–288.

(81)   Podlaha, E. J.; Bonhôte, C.; Landolt, D. A Mathematical Model and Experimental Study of the Electrodeposition of NiCu Alloys from Complexing Electrolytes. *Electrochim. Acta* **1994**, *39* (18), 2649–2657.

(82) Karwas, C.; Hepel, T. Morphology and Composition of Electrodeposited Cobalt-Zinc Alloys and the Influence of Boric Acid. *J Electrochem Soc* **1989**, *136* (6), 1672–1678.

(83) Orin, T. A.; Turon, A.; Kladekova, D.; Smith, R. M. Recent Developments in the Electrodeposition of Nickel and Some Nickel-Based Alloys. *J. Appl. Electrochem.* **2006**, *63*, 957–972.

(84) Luo, A. A.; Luo, A. A. Recent Magnesium Alloy Development for Elevated Temperature Applications. *Int. Mater. Rev.* **2013**, *49* (1), 13–30.

(85) Ye, H. An Overview of the Development of Al-Si-Alloy Based Material for Engine Applications. *J. Mater. Eng. Perform.* **2003**, *12* (3), 288–297.

(86) Srivastava, M.; Selvi, V. E.; Grips, V. K. W.; Rajam, K. S. Corrosion Resistance and Microstructure of Electrodeposited Nickel − Cobalt Alloy Coatings. *Surf. Coatings Technol.* **2006**, *201* (6), 3051–3060.

(87) Mez, Â.; Ramirez, J.; Valle, E. Electrodeposition of Co ± Ni Alloys. *J. Appl. Electrochem.* **1998**, *28*, 71–79.

(88) Lupi, C.; Pilone, D. Electrodeposition of Nickel-Cobalt Alloy : The Effect of Process Process Parameters on Energy Consumption. *Miner. Eng.* **2001**, *6875* (1), 1403–1410.

(89) Chen, Y.; Peng, D.-L.; Lin, D.; Luo, X. Preparation and Magnetic Properties of Nickel Nanoparticles via the Thermal Decomposition of Nickel Organometallic Precursor in Alkylamines. *Nanotechnology* **2007**, *18* (50), 505703.

(90) Bolokang, A. S.; Phasha, M. J. Novel Synthesis of Metastable HCP Nickel by Water Quenching. *Mater. Lett.* **2011**, *65* (1), 59–60.

(91) Zech, N.; Podlaha, E. J.; Landolt, D. Anomalous Codeposition of Iron Group Metals: II. Mathematical Model. *J. Electrochem. Soc.* **1999**, *146* (8), 2892.

(92) Ashcroft, N. W. Vegard's Law. *Phys. Rev. A* **1991**, *43* (6), 3161–3164.

(93) Huang, X. H.; Tu, J. P.; Xia, X. H.; Wang, X. L.; Xiang, J. Y.; Zhang, L.; Zhou, Y. Morphology Effect on the Electrochemical Performance of NiO Films as Anodes for Lithium Ion Batteries. *J. Power Sources* **2009**, *188* (2), 588–591.

(94) Li, W.; Currie, J. C. Morphology Effects on the Electrochemical Performance of LiNi 1-xCo xO 2. *J. Electrochem. Soc.* **1997**, *144* (8), 2773–2779.

(95) Song, M.-K.; Cairns, E. J.; Zhang, Y. Lithium/sulfur Batteries with High Specific Energy: Old Challenges and New Opportunities. *Nanoscale* **2013**, *5* (6), 2186.

(96) Bruce, P. G.; Freunberger, S. A.; Hardwick, L. J.; Tarascon, J.-M. Li–O2 and Li–S

Batteries with High Energy Storage. *Nat. Mater.* **2012**, *11* (1), 19–29.

(97) Manthiram, A.; Yu, X.; Wang, S. Lithium Battery Chemistries Enabled by Solid-State Electrolytes. *Nat. Rev. Mater.* **2017**, *2* (4), 1–16.

(98) Bachman, J. C.; Muy, S.; Grimaud, A.; Chang, H. H.; Pour, N.; Lux, S. F.; Paschos, O.; Maglia, F.; Lupart, S.; Lamp, P.; et al. Inorganic Solid-State Electrolytes for Lithium Batteries: Mechanisms and Properties Governing Ion Conduction. *Chem. Rev.* **2016**, *116* (1), 140–162.

(99) Xu, W.; Wang, J.; Ding, F.; Chen, X.; Nasybulin, E.; Zhang, Y.; Zhang, J.-G. Lithium Metal Anodes for Rechargeable Batteries. *Energy Environ. Sci.* **2012**, *7* (2), 513–537.

(100) Zhamu, A.; Chen, G.; Liu, C.; Neff, D.; Fang, Q.; Yu, Z.; Xiong, W.; Wang, Y.; Wang, X.; Jang, B. Z. Reviving Rechargeable Lithium Metal Batteries: Enabling next-Generation High-Energy and High-Power Cells. *Energy Environ. Sci.* **2012**, *5* (2), 5701–5707.

(101) Harry, K. J.; Hallinan, D. T.; Parkinson, D. Y.; MacDowell, A. A.; Balsara, N. P. Detection of Subsurface Structures underneath Dendrites Formed on Cycled Lithium Metal Electrodes. *Nat. Mater.* **2014**, *13* (1), 69–73.

(102) Lv, D.; Shao, Y.; Lozano, T.; Bennett, W. D.; Graff, G. L.; Polzin, B.; Zhang, J.; Engelhard, M. H.; Saenz, N. T.; Henderson, W. A.; et al. Failure Mechanism for Fast-Charged Lithium Metal Batteries with Liquid Electrolytes. *Adv. Energy Mater.* **2015**, *5* (3), 1–7.

(103) Sun, Y.; Liu, N.; Cui, Y. Promises and Challenges of Nanomaterials for Lithium-Based Rechargeable Batteries. *Nat. Energy* **2016**, *1* (7), 1–12.

(104) Peled, E. The Electrochemical Behavior of Alkali and Alkaline Earth Metals in Nonaqueous Battery Systems—The Solid Electrolyte Interphase Model. *J. Electrochem. Soc.* **1979**, *126* (12), 2047.

(105) Arakawa, M.; Tobishima, S. ichi; Nemoto, Y.; Ichimura, M.; Yamaki, J. ichi. Lithium Electrode Cycleability and Morphology Dependence on Current Density. *J. Power Sources* **1993**, *43* (1–3), 27–35.

(106) Brissot, C.; Rosso, M.; Chazalviel, J. N.; Lascaud, S. Dendritic Growth Mechanisms in Lithium/polymer Cells. *J. Power Sources* **1999**, *81*, 925–929.

(107) Rosso, M.; Gobron, T.; Brissot, C.; Chazalviel, J. N.; Lascaud, S. Onset of Dendritic Growth in Lithium/polymer Cells. *J. Power Sources* **2001**, *97–98*, 804–806.

(108) Kanamura, K. Electrochemical Deposition of Very Smooth Lithium Using Nonaqueous Electrolytes Containing HF. *J. Electrochem. Soc.* **1996**, *143* (7), 2187.

(109) Lu, Y.; Tu, Z.; Archer, L. A. Stable Lithium Electrodeposition in Liquid and Nanoporous Solid Electrolytes. *Nat. Mater.* **2014**, *13* (10), 961–969.

(110) Guo, J.; Wen, Z.; Wu, M.; Jin, J.; Liu, Y. Vinylene Carbonate-LiNO3: A Hybrid Additive in Carbonic Ester Electrolytes for SEI Modification on Li Metal Anode. *Electrochem. commun.* **2015**, *51*, 59–63.

(111) Li, W.; Yao, H.; Yan, K.; Zheng, G.; Liang, Z.; Chiang, Y. M.; Cui, Y. The Synergetic Effect of Lithium Polysulfide and Lithium Nitrate to Prevent Lithium Dendrite Growth. *Nat. Commun.* **2015**, *6*, 1–8.

(112) Ye, H.; Yin, Y. X.; Zhang, S. F.; Shi, Y.; Liu, L.; Zeng, X. X.; Wen, R.; Guo, Y. G.; Wan, L. J. Synergism of Al-Containing Solid Electrolyte Interphase Layer and Al-Based Colloidal Particles for Stable Lithium Anode. *Nano Energy* **2017**, *36*, 411–417.

(113) Yan, K.; Lee, H. W.; Gao, T.; Zheng, G.; Yao, H.; Wang, H.; Lu, Z.; Zhou, Y.; Liang, Z.; Liu, Z.; et al. Ultrathin Two-Dimensional Atomic Crystals as Stable Interfacial Layer for Improvement of Lithium Metal Anode. *Nano Lett.* **2014**, *14* (10), 6016–6022.

(114) Zheng, G.; Lee, S. W.; Liang, Z.; Lee, H. W.; Yan, K.; Yao, H.; Wang, H.; Li, W.; Chu, S.; Cui, Y. Interconnected Hollow Carbon Nanospheres for Stable Lithium Metal Anodes. *Nat. Nanotechnol.* **2014**, *9* (8), 618–623.

(115) Huang, C.; Xiao, J.; Shao, Y.; Zheng, J.; Bennett, W. D.; Lu, D.; Saraf, L. V.; Engelhard, M.; Ji, L.; Zhang, J.; et al. Manipulating Surface Reactions in Lithium-Sulphur Batteries Using Hybrid Anode Structures. *Nat. Commun.* **2014**, *5*, 1–7.

(116) Pang, Q.; Liang, X.; Shyamsunder, A.; Nazar, L. F. An In Vivo Formed Solid Electrolyte Surface Layer Enables Stable Plating of Li Metal. *Joule* **2017**, *1* (4), 871–886.

(117) Li, N. W.; Shi, Y.; Yin, Y. X.; Zeng, X. X.; Li, J. Y.; Li, C. J.; Wan, L. J.; Wen, R.; Guo, Y. G. A Flexible Solid Electrolyte Interphase Layer for Long-Life Lithium Metal Anodes. *Angew. Chemie - Int. Ed.* **2018**, *57* (6), 1505–1509.

(118) Duan, H.; Yin, Y. X.; Shi, Y.; Wang, P. F.; Zhang, X. D.; Yang, C. P.; Shi, J. L.; Wen, R.; Guo, Y. G.; Wan, L. J. Dendrite-Free Li-Metal Battery Enabled by a Thin Asymmetric Solid Electrolyte with Engineered Layers. *J. Am. Chem. Soc.* **2018**, *140* (1), 82–85.

(119) Cheng, X.; Yan, C.; Cheng, X.; Yan, C.; Chen, X.; Guan, C.; Huang, J.; Peng, H. Implantable Solid Electrolyte Interphase in Lithium-Metal Batteries Implantable Solid Electrolyte Interphase in Lithium-Metal Batteries. *Chempr* **2017**, *2* (2), 258–270.

(120) Wang, D.; Zhang, W.; Zheng, W.; Cui, X.; Rojo, T.; Zhang, Q. Towards High-Safe

Lithium Metal Anodes: Suppressing Lithium Dendrites via Tuning Surface Energy. *Adv. Sci.* **2017**, *4* (1).

(121) Choudhury, S.; Mangal, R.; Agrawal, A.; Archer, L. A. A Highly Reversible Room-Temperature Lithium Metal Battery Based on Crosslinked Hairy Nanoparticles. *Nat. Commun.* **2015**, *6*, 1–9.

(122) Han, X.; Gong, Y.; Fu, K.; He, X.; Hitz, G. T.; Dai, J.; Pearse, A.; Liu, B.; Wang, H.; Rubloff, G.; et al. Negating Interfacial Impedance in Garnet-Based Solid-State Li Metal Batteries. *Nat. Mater.* **2017**, *16* (5), 572–579.

(123) Zeng, X. X.; Yin, Y. X.; Li, N. W.; Du, W. C.; Guo, Y. G.; Wan, L. J. Reshaping Lithium Plating/Stripping Behavior via Bifunctional Polymer Electrolyte for Room-Temperature Solid Li Metal Batteries. *J. Am. Chem. Soc.* **2016**, *138* (49), 15825–15828.

(124) Yang, C. P.; Yin, Y. X.; Zhang, S. F.; Li, N. W.; Guo, Y. G. Accommodating Lithium into 3D Current Collectors with a Submicron Skeleton towards Long-Life Lithium Metal Anodes. *Nat. Commun.* **2015**, *6*, 1–9.

(125) Lu, L. L.; Ge, J.; Yang, J. N.; Chen, S. M.; Yao, H. Bin; Zhou, F.; Yu, S. H. Free-Standing Copper Nanowire Network Current Collector for Improving Lithium Anode Performance. *Nano Lett.* **2016**, *16* (7), 4431–4437.

(126) Liu, L.; Yin, Y. X.; Li, J. Y.; Li, N. W.; Zeng, X. X.; Ye, H.; Guo, Y. G.; Wan, L. J. Free-Standing Hollow Carbon Fibers as High-Capacity Containers for Stable Lithium Metal Anodes. *Joule* **2017**, *1* (3), 563–575.

(127) Zuo, T. T.; Wu, X. W.; Yang, C. P.; Yin, Y. X.; Ye, H.; Li, N. W.; Guo, Y. G. Graphitized Carbon Fibers as Multifunctional 3D Current Collectors for High Areal Capacity Li Anodes. *Adv. Mater.* **2017**, *29* (29), 1–6.

(128) Yun, Q.; He, Y. B.; Lv, W.; Zhao, Y.; Li, B.; Kang, F.; Yang, Q. H. Chemical Dealloying Derived 3D Porous Current Collector for Li Metal Anodes. *Adv. Mater.* **2016**, *28* (32), 6932–6939.

(129) Wang, S. H.; Yin, Y. X.; Zuo, T. T.; Dong, W.; Li, J. Y.; Shi, J. L.; Zhang, C. H.; Li, N. W.; Li, C. J.; Guo, Y. G. Stable Li Metal Anodes via Regulating Lithium Plating/Stripping in Vertically Aligned Microchannels. *Adv. Mater.* **2017**, *29* (40), 1–8.

(130) Liu, S.; Wang, A.; Li, Q.; Wu, J.; Chiou, K.; Huang, J.; Luo, J. Crumpled Graphene Balls Stabilized Dendrite-Free Lithium Metal Anodes. *Joule* **2017**, *2* (1), 184–193.

(131) Yan, K.; Sun, B.; Munroe, P.; Wang, G. Three-Dimensional Pie-like Current Collectors for Dendrite-Free Lithium Metal Anodes. *Energy Storage Mater.* **2018**, *11*, 127–133.

(132) Zhang, A.; Fang, X.; Shen, C.; Liu, Y.; Zhou, C. A Carbon Nanofiber Network for Stable Lithium Metal Anodes with High Coulombic Efficiency and Long Cycle Life. *Nano Res.* **2016**, *9* (11), 3428–3436.

(133) Zhang, R.; Chen, X. R.; Chen, X.; Cheng, X. B.; Zhang, X. Q.; Yan, C.; Zhang, Q. Lithiophilic Sites in Doped Graphene Guide Uniform Lithium Nucleation for Dendrite-Free Lithium Metal Anodes. *Angew. Chemie - Int. Ed.* **2017**, *56* (27), 7764–7768.

(134) Liu, L.; Yin, Y.-X.; Li, J.-Y.; Wang, S.-H.; Guo, Y.-G.; Wan, L.-J. Uniform Lithium Nucleation/Growth Induced by Lightweight Nitrogen-Doped Graphitic Carbon Foams for High-Performance Lithium Metal Anodes. *Adv. Mater.* **2018**, 1706216.

(135) Shen, F.; Zhang, F.; Zheng, Y.; Fan, Z.; Li, Z.; Sun, Z.; Niu, C. Direct Growth of 3D Host on Cu Foil for Stable Lithium Metal Anode. *Energy Storage Mater.* **2018**, *13*, 323–328.

(136) Zhao, H.; Lei, D.; He, Y.; Yuan, Y.; Yun, Q.; Ni, B.; Lv, W. Compact 3D Copper with Uniform Porous Structure Derived by Electrochemical Dealloying as Dendrite-Free Lithium Metal Anode Current Collector. *Adv. Energy Mater.* **2018**, *8*, 1800266.

(137) Ma, Y.; Yao, B.; Zhang, M. Inhibiting the Growth of Lithium Dendrites at High Current Densities with Oriented Graphene Foam. *J. Mater. Chem. A* **2018**, *6*, 15603–15609.

(138) Yan, K.; Lu, Z.; Lee, H.-W.; Xiong, F.; Hsu, P.-C.; Li, Y.; Zhao, J.; Chu, S.; Cui, Y. Selective Deposition and Stable Encapsulation of Lithium through Heterogeneous Seeded Growth. *Nat. Energy* **2016**, *1* (3), 16010.

(139) Liang, X.; Pang, Q.; Kochetkov, I. R.; Sempere, M. S.; Huang, H.; Sun, X.; Nazar, L. F. A Facile Surface Chemistry Route to a Stabilized Lithium Metal Anode. *Nat. Energy* **2017**, *2*, 17119.

(140) Cheng, X. B.; Hou, T. Z.; Zhang, R.; Peng, H. J.; Zhao, C. Z.; Huang, J. Q.; Zhang, Q. Dendrite-Free Lithium Deposition Induced by Uniformly Distributed Lithium Ions for Efficient Lithium Metal Batteries. *Adv. Mater.* **2016**, *28* (15), 2888–2895.

(141) Zhu, B.; Jin, Y.; Hu, X.; Zheng, Q.; Zhang, S.; Wang, Q.; Zhu, J. Poly(dimethylsiloxane) Thin Film as a Stable Interfacial Layer for High-Performance Lithium-Metal Battery Anodes. *Adv. Mater.* **2017**, *29* (2), 2–7.

(142) Nikolić, N. D.; Popov, K. I.; Pavlović, L. J.; Pavlović, M. G. Morphologies of Copper Deposits Obtained by the Electrodeposition at High Overpotentials. *Surf. Coatings Technol.* **2006**, *201* (3–4), 560–566.

(143) Arai, S.; Kitamura, T. Simple Method for Fabrication of Three-Dimensional (3D) Copper Nanostructured Architecture by Electrodeposition. *ECS Electrochem. Lett.* **2014**, *3* (5), D7–D9.

(144) Nitta, N.; Yushin, G. High-Capacity Anode Materials for Lithium-Ion Batteries: Choice of Elements and Structures for Active Particles. *Part. Part. Syst. Charact.* **2014**, *31* (3), 317–336.

(145) Ko, M.; Chae, S.; Ma, J.; Kim, N.; Lee, H. W.; Cui, Y.; Cho, J. Scalable Synthesis of Silicon-Nanolayer-Embedded Graphite for High-Energy Lithium-Ion Batteries. *Nat. Energy* **2016**, *1* (9), 1–8.

(146) Shin, B. R.; Nam, Y. J.; Oh, D. Y.; Kim, D. H.; Kim, J. W.; Jung, Y. S. Comparative Study of TiS2/Li-In All-Solid-State Lithium Batteries Using Glass-Ceramic Li3PS4and Li10GeP2S12 Solid Electrolytes. *Electrochim. Acta* **2014**, *146*, 395–402.